Modeling 3D Numerical Movable Bed based on LBM and its Application to the Analysis of Bed-Load Transport and Tsunami Drifts

（３次元ＬＢＭ数値移動床モデルの開発と掃流砂輸送および津波漂流物解析へのその適用）

Lulu HE

Dissertation Supervisor: Prof. Wataru KIOKA

Nagoya Institute of Technology
Nagoya, Japan
June, 2014

ABSTRACT

It is important to study the processes of sediment transport for the beach nourishment of sandy beaches, for the design of costal and fluvial structures, i.e., dam, groynes, breakwaters, etc., and for the dredging problems in channels and ports. Typically sediment can be transported both as suspended load and as bed load. Researchers are always interested in the particle motion of bed load layer, including rolling, sliding, saltation and the vertical sorting of graded sands. Numbers of hydraulic experiments and numerical studies have been performed to study the sediment transport on bedload layer. However, numerical studies on the particle motions of bedload layer, especially vertical sorting processes of mixed grain size sediments under oscillatory flows and progressive waves are still limited.

In order to analyze both the uniform grain size and mixed grain size sediment transport (regular sphere particles) and the behavior of tsunami drifts (particles with irregular shapes), a 3D numerical model of movable bed based on Lattice Boltzmann Method (LBM) will be established. The advantages of this model are listed as follows: (1) Free surface condition is included in the model for the simulation of open channel flows, oscillatory flows, progressive waves and tsunami currents. (2) Sub Grid Smagorinsky (SGS) turbulence term is considered. (3) Both the particle-particle interaction and particle-fluid interaction are effectively simulated by using a link-bounce-back scheme. (4) External forces can be easily added by modifying the DFs. Drag forces, gravity force, buoyance force, and also lubrication forces are considered in the model.

Cases of uniform grain size sediment under open channel flows in sheetflow regimes with different Shields parameters are performed by using this 3D movable bed model. In order to check the feasibility of the present model, the 3D behaviors of the uniform bed-load

sediments, including rolling, sliding and saltation are observed, and the typical characteristics of bed-load sediments, i.e. the horizontal velocity and the vertical existing probability density function (P.D.F) of sediments are analyzed. The present simulation predicts well the behavior of each particle in the bed-load layer both in saltation and sheetflow regimes. The simulation results for the height and length of saltation, the bed-load velocity and the existing probability density agree fairly well with the experimental data from Gotoh et al. (1993, 1994).

Cases of mixed-grain-size sediments under oscillatory flow (both symmetric sinusoidal flow and asymmetric flow based on the second cnoidal wave theory) in sheetflow regime are conducted by applying this 3D movable bed model. Knowledge of vertical sorting process of mixed grain size sediment, especially under progressive waves, is still limited. The present study focuses on the processes of vertical sorting of mixed sands, which is essential for further study on the sediment transport of mixed grain size sediment. The main influence factors, such as period, Shields parameters, bottom layer thickness, bottom slope, are discussed in the cases of mixed sands under symmetric oscillatory flows. The results show that (1) the phenomenon of vertical sorting is more significant with larger shields number; (2) sediment particles become more motive with the increase of the water particle semi-excursion, due to more momentum obtained from the fluid, and as a result, the armor may break; (3) Armoring takes effect earlier when the thickness of sediments increases to double. Besides, the processes of vertical sorting of mixed grain size sediment under a realistic progressive wave are performed. The result shows that vertical sorting proceeds until the wave crest passing by and fully develops in a complete period. The concentration centroid of particles for overall width is not uniform in wave progressing direction. The concentration centroid of large particles is higher landward within 2 periods.

The behavior of drifting automobiles due to tsunami inundation is studied by modifying this 3D movable bed model for particles with irregular shapes. As it is important to known the movement of large drift, i.e. automobiles, in tsunami and its collision behavior to tsunami evacuation tower, a facility used to protect the safety of life and property in the

tsunami-affected areas. For the verification of the modified numerical model, laboratory experiments with 80 automobiles colliding to the pillars of both Bridge type of tsunami evacuation tower (with a large distance between pillars) and Conventional tsunami evacuation tower (with beams between pillars) are carried out. The simulation results show that the behavior of drifting automobiles bypassing the pillars of tsunami evacuation tower is quite similar to the experimental results.

A 3D numerical movable bed model based on Ladd's LBM has been extended to free surface flow and with SGS turbulence term. This gas-fluid-solid model identifies fluid-gas interaction by applying a fluid fraction ε, and deals the fluid-solid interaction and solid-solid interaction by using a link-bounce-back scheme. The present model has been successfully used to simulate sediment transport with sphere shapes and drift automobiles with irregular shapes. Based on this, sediments with irregular shape can be simulated in the future. Besides, in the present LBM model, any semi-empirical coefficient is not needed as an input data, but only the cut-off of lubrication approximation, the additional offset in computing fluid fraction, together with the Smagorinsky Constant in turbulent model are required. And it can be extended relatively easily to 3D movable bed in large computation domain, as the LBM process involves an algorithm suitable for parallel computation.

Key Words: *LBM, SGS turbulence model, free surface, sediment transport, vertical sorting, bed-load, drift behavior, tsunami*

CONTENTS

CHAPTER 1 INTRODUCTION 1

1.1 Study Background 1
1.1.1 Importance of coastal and fluvial zones 1
1.1.2 Importance of study on sediment transport 2
1.1.3 Importance of study on tsunami drifts 4
1.1.4 Information of numerical movable bed 5

1.2 Literature Review 7
1.2.1 Numerical model for simulating the behaviors of particles in the fluid 7
1.2.2 Uniform grain size sediment transport under open channel flows 8
1.2.3 Mixed grain size sediment transport under oscillatory flows and progressive waves 10
1.2.4 The behavior of tsunami drifts 13

1.3 Study Objectives 14

1.4 Dissertation Layouts 15

CHAPTER 2 LATTICE BOLTZMANN METHOD USED FOR 3D MOVABLE BED 17

2.1 An Introduction to Lattice Boltzmann Method (LBM) 17

2.2 Basic Algorithm of LBM 18
2.2.1 Boltzmann equation 18
2.2.2 Discrete Boltzmann approximation 19
2.2.3 Basic steps for computation 22

2.3 Ladd's LBM for Particle-Fluid Suspension 23
2.3.1 Discrete Boltzmann approach 24
2.3.2 Link-Bounce-Back scheme 26

2.3.3 Lubrication forces....30
2.4 LBM with Free Surface Flow....31

2.5 LBM with SGS Turbulence Term....35

CHAPTER 3 THE BEHAVIOR OF UNIFORM GRAIN SIZE SEDIMENTS UNDER OPEN CHANNEL FLOWS....37

3.1 Introduction....37

3.2 Numerical Conditions....38

3.3 Simulation Results....41
3.3.1 Flow velocity field of the open channel flow....42
3.3.2 Movements of sediment particles....45
3.3.3 Horizontal velocity of sediment particles....55
3.3.4 Vertical P.D.F of sediment particles....56

3.4 Conclusions....57

CHAPTER 4 THE BEHAVIOR OF MIXED GRAIN SIZE SEDIMENTS UNDER BOTH OSCILLATORY FLOWS AND PROGRESSIVE WAVE....59

4.1 Introductions....59

4.2 Numerical Conditions....60

4.3 Simulation Results of Mixed Sands under Symmetric Oscillatory Flows....63
4.3.1 Vertical sorting process....63
4.3.2 Concentration centroids of mixed sands....70
4.3.3 Mean velocity of sediment particles....73
4.3.4 Dimensionless particle number density distribution....79

4.4 Simulation Results of Mixed Sands under Progressive Cnoidal Wave....85
4.4.1 Cnoidal wave....85

4.4.2 Vertical sorting of mixed sands under cnoidal wave 88

4.5 Conclusions 94

CHAPTER 5 THE DRIFT BEHAVIOR OF DEBRIS WITH IRREGULAR SHAPE IN TSUNAMI 97

5.1 Introduction 97

5.2 Hydrodynamic Experiments 98
5.2.1 Model set-up and experimental method 98
5.2.1 Collision number and collision speed 102
5.2.3 Trajectories of the center of automobiles 105

5.3 Simulation Results 107

5.4 Conclusions 113

CHAPTER 6 CONCLUSIONS 115

6.1 Uniform Sands under Open Channel Flow 116

6.2 Mixed Sands Transport under Oscillatory Flows and Progressive Wave 117

6.3 Submerged Drift Automobiles under Tsunami Flooding Currents 118

References 121

List of Tables 129

List of Figures 131

Acknowledgement 137

CHAPTER 1

INTRODUCTION

1.1 Study Background

1.1.1 Importance of coastal and fluvial zones

Most of the countries in the world have long shorelines. As recorded in "Shore Protection Manual" (USACE, 1984), the United States has a total shoreline of 135,550 km with 41% of exposed shoreline and 59% of sheltered shoreline. In the summary made by Hanson et al. (2002), most European countries have long coasts, i.e., Germany of 1,900km, Italy of 7,500km, France of 5,500km, etc. For the Asian countries, China has a total 18,000 km shoreline (Kuang et al., 2011) and Japan of 34,000 km (Uda, 2010).

Coastal and fluvial areas have been important for human beings throughout history. In the past, humans settled in the areas near river and coast, mainly for the benefit of getting water and food. While nowadays, coastal and fluvial zones are still attractive, primarily because of the economic interests with convenient transportation, the tourism activities with water environment and the convenience of living in large modern cities which are mostly developed along seacoast, lakes and rivers. The statistical results show that approximately 40% of the world's population lives in the relatively narrow coastal zones today (Small and Cohen, 2004).

The long shorelines and the dense population push us to have a full knowledge about costal and fluvial environment, i.e., sediment transport, tsunami drifts. One common problem of these two issues is studying the behavior of solid particles in fluids, namely, the particle-particle interaction and the particle-fluid interaction.

1.1.2 Importance of study on sediment transport

It is important to study the processes of sediment transport for the beach nourishment of sandy beaches (as illustrated by van der Salm and Unal in 2003 that 95% of the world beaches are eroding due to human activities and moving dynamics), for the design of costal and fluvial structures, i.e., dam, groynes, breakwaters, etc., and for the dredging problems in channels and ports.

Typically sediment can be transported both as suspended load and as bed load (with rolling, sliding, and saltation motions), depending on the size of the bed material particles and the flow conditions. Bed load is supported by inter-particle forces, while the suspended load is supported by upward fluid drag. The details about the motion of sediment particles can be found in the paper of van Rijn (1984).

Sediment transport occurring in the near-shore region is usually divided into a cross-shore and a longshore component. Cross-shore transport is dominated by the wave orbital motion and cross-shore net currents, whereas longshore transport is generally associated with tidal and wave-induced currents after breaking (Al-Salem, 1993). **Figure 1.1** shows an introductory overview of the cross-shore sediment transport modes on a beach. In deep water, the bed is unaffected by waves and consequently any sediment transport will happen due to tidal or other ocean currents. In somewhat shallower depths ($h<25m$) the wave motion will often dominate flow near the bed and the sediment transport. In the cross-shore direction, the sediment transport is quite complicated due to different conditions, i.e., water depths, bedforms, wave properties, wave induced currents, turbulences, etc. Cross-shore sediment transport has a complex three-dimensional and time-dependent character, as it is driven by the wave orbital motion and net currents (e.g., the oscillatory flows) near the seabed. The interaction between the oscillatory water velocity and the sediment at the sea-bed may lead to a resulting sediment transport in or opposite to the direction of the wave propagation, as the waves are commonly asymmetric in nature.

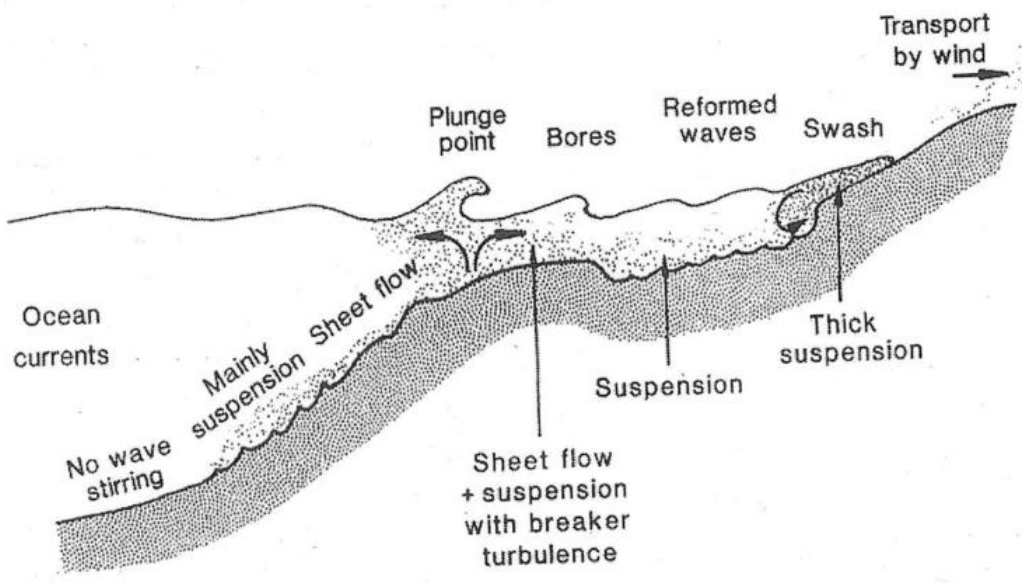

Figure 1.1 Sediment transport modes on a beach, a simplified 2D view. (Nielsen, 2009)

Field observations (Hassan and Ribberink, 2005) showed that the sea bed sediments are generally composed of a mixture of different grain sizes with coarse material in deeper water. Nowadays, people are interested in the processes of vertical sorting of mixed grain size sediments in the cross-shore zones, as the phenomenon of "dynamic armoring" (also called as "reciprocal armoring") with coarser sediment particles above the finer ones, is observed. It is in contrast to the conventional "static armoring", which usually happens among sediments in river field (uni-directional flows) with finer sands in the upper bed layers and coarser sands in the lower bed layer. Numerous hydrodynamic experiments (Dibajnia and Watanabe, 2000; Ahmed and Sato, 2003a, b; Hassan and Ribberink, 2005) and numerical simulations (Gotoh and Sakai, 1997; Dong and Zhang, 1999; Thaxton and Calantoni, 2006; Harada and Gotoh, 2008) have been conducted to study the mechanisms of vertical sorting processes and the transport rates of mixed grain size sediments. Most of the above studies are carried out in the sheetflow regime, as a large amount of sediment is transported under sheetflow regime. However, numerical studies on vertical sorting

processes of mixed grain size sediments under oscillatory flows and progressive waves are still limited. Hence, in the dissertation, the vertical sorting of mixed sands will be carried out under both oscillatory flows and progressive cnoidal wave in the sheetflow regime.

1.1.3 Importance of study on tsunami drifts

Tsunami has threatened Human beings by causing enormous disasters and huge losses since old times. Tsunamis can be generated by tectonic earthquakes, which may cause the deformation of sea floor abruptly and the vertical displacement of the overlying water and finally generate ocean earthquake tsunamis. Countries bordering ocean trenches like Japan have high possibility to be attacked by such tsunamis.

Japan may have the longest recorded history of tsunamis (Yeom, 2009). In 1896, the area around Sanriku coast was damaged with more than 20,000 deaths and the presumed financial damage of 10% of Japanese national budget at that time by tsunami due to Meiji-Sanriku earthquake. In 1933, 3,064 people lost their lives on Showa-Sanriku tsunami. And in 1993, a whole village of Okushiri island, Hokkaido was destroyed totally in the Hokkaido-Nanseioki earthquake tsunami, because of the quick coming of the first wave, 3-5 min after the occurrence of the earthquake. The most serious disaster recently is the Great East Japan Earthquake and its accompany tsunami (also known as 2011 Tohoku earthquake and tsunami), which cause 15,885 deaths, 6,148 injured, and 2,623 people missing across twenty prefectures, as well as 127,290 buildings totally collapsed, with a further 272,788 buildings 'half collapsed', and another 747,989 buildings partially damaged, reported by the Japanese National Police Agency on 10 February 2014. **Figure 1.2** shows the damage in the Sendai region after the Great East Japan Earthquake.

Figure 1.2 An aerial view of damage in the Sendai region with black smoke coming from the Nippon Oil Sendai oil refinery.
(http://en.wikipedia.org/wiki/2011_T%C5%8Dhoku_earthquake_and_tsunami)

In order to save lives and reduce damage caused by tsunami, tsunami refuge terraces are built at fishery ports. While in plazas or parks with large parking place in the coastal land area, tsunami evacuation towers are usually constructed to provide upland for people to evacuate in case of a tsunami inundation. However, these tsunami evacuation towers may always face the collisions from large tsunami drifting debris (such as automobiles) to theirs pillars, and the corresponding damage in a tsunami flooding. Hence, study on the movements of large drifts and their collisions to the tsunami evacuation tower will be performed in this paper.

1.1.4 Information of numerical movable bed

In order to analyze both the uniform grain size and mixed grain size sediment transport and the behavior of tsunami drifts, a 3D numerical model of movable bed based on Lattice

Boltzmann Method (LBM) will be established. The advantages of this model are listed as follows:

(1) Free surface condition is included in the model for the simulation of open channel flows, oscillatory flows, progressive waves and tsunami currents. The intrinsic characteristic of LBM, of which all the macroscopic variables (density, momentum, momentum flux of the fluid) can be simulated with a serious of microscopic Distribution Functions (DFs) of virtual particles in each lattice, makes the expansion of free surface condition more conveniently without any huge computational cost. In the dissertation, free-surface interface is simulated based on the method proposed by Thürey and Rüde (2009), in which a fluid fraction parameter ε is used to distinguish fluid (ε=1), gas (ε=0) and interface lattices ($0<\varepsilon<1$).

(2) Sub Grid Smagorinsky (SGS) turbulence model is considered. Unlike other methods, SGS model is easily applied by adding the modified total kinematic viscosity to the collision term of the general Lattice Boltzmann Equation (LBE) with BGK approximation (He et al., 2013). The total kinematic viscosity is composed by the eddy viscosity coefficient of SGS turbulence term and the normal kinematic viscosity coefficient.

(3) Both the particle-particle interaction and particle-fluid interaction are effective. The surface of an individual particle is constructed with a serious a boundary nodes which located in the center of fluid nodes and solid nodes inside the rigid particle. It is assumed that there are no DFs in the solid nodes, and the momentum transfers between fluid and particle are through the link-bounce-back scheme. More details about link-bounce-back scheme are illustrated in Chapter 2.

(4) External forces can be easily added by modifying the DFs. Drag forces, gravity force, buoyance force, and also lubrication forces are considered in the model. The present model has also been successfully used to simulate the sediment transport of very fine coherent sediments by including the van der Waals forces and Ionic forces (Sumori, 2014).

More detailed descriptions of basic LBM model, the characteristics of Ladd's LBM model for chemical particle-fluid suspension, and the theories of free surface flows and SGS turbulent model can be found in Chapter 2.

1.2 Literature Review

1.2.1 Numerical model for simulating the behaviors of particles in the fluid

In the numerical simulation, both sub-mechanisms of fluid-particle interaction and particle-particle interaction should be considered. However, research for bed-load sediment transports focusing on the fluid-particle interaction and particle-particle interaction is still limited. Most of the experiments focus on the sediment transport rate (e.g. Ribberink, 1998; Dibajnia and Watanabe, 2000; Ahmed and Sato, 2003 a, b) except Harada and Gotoh (2008), who use relatively larger but lighter artificial pearl to study particles behaviors in the fluid.

For the numerical simulation, there are typically two kinds of models for particle motions in bed-load transport. One is two-phase flow model (Dong and Zhang, 1999), an Euler-Euler coupling mode, which is good at dealing with fluid-particle interaction but weak at particle-particle interaction, as both flow model and particle model are Eulerian, while the motion of particles is essentially Langrangian. This deficiency has been improved in the granular model, a Langrangian model with coupled one-way (van Rijn, 1984) or two-way (Gotoh and Sakai, 1997) flow models. However, in most of the granular

models, the behaviors of particles are emphasized while the flow characteristics are mostly simplified. For instance, Xu and Yu (1997) developed a numerical model to solve particle-fluid interaction by combining Discrete Particle Method (DPM) and Computational Fluid Dynamics (CFD) with local averaged Navier-Stokes Equation together. Fukuda et al. (2013) proposed a numerical method to study the 3D motion of gravel particles of various shape and size combined with a group of small spheres, and the fluid motion by using governing equations of multiphase flows.

Few studies emphasize both particle-particle interaction and particle-fluid interaction. Feng and Michaelides (2003) applied LBM, originally from Ladd's particle-fluid suspension model, to study the behavior of particle motions in 2D space. However, for a 2D model, the freedom of movement is very low and the resistance against particle movement increases because all the particles are in the same plane. While for a 3D model, the resistance transfer of an individual particle can be considered because the interaction between particles outside the same plane can be evaluated. More recently, a granular model with a combination of Discrete Element Method (DEM) for the motion of particles and discrete Boltzmann equation for the solution of fluid is proposed by Feng et al. (2010). Studies on 3D particle-fluid and particle-particle interactions are extremely few, and most of which are done by Gotoh et al. (2002) and Harada and Gotoh (2008), whose 3D granular material model is based on the Distinct Element Method.

1.2.2 Uniform grain size sediment transport under open channel flows

Although field observations show that sea bed sediments are generally composed of a mixture of different grain sizes, researchers are interested in the sediment transport of uniform grain size sands, as it is easy to study the mobility of sediments in fluid (including rolling, sliding, and saltation for bed-load sediments), external forces exerting on particles, and the sediment transport rates. However, the prediction of sediment transport is very difficult even with uniform grain size sediments, because the flow in open channel is usually turbulent, the geometry is irregular and can vary with time, and sediment transport

phenomena are very complex.

Researches on bed-load transport in open channels were performed early in 1940s. Based on numerous hydrodynamic experiments, Meyer-Peter and Müller (1948) established an empirical equation for bed-load sediment transport rate in open channel. Einstein (1950) proposed a semi-empirical equation for bed-load sediment transport rate by considering the experimental results of uniform sands in an alluvial channel together with probability theory and hydraulic mechanisms. Based on the bed-shear concept of Meyer-Peter and Müller, Ribberink (1998) developed a general bed-load transport concept for a wide range of flow and sediment conditions through more than 150 laboratory experiments under steady unidirectional flows, oscillatory flows and oscillatory flows with superimposed net currents. Ahmed and Sato (2003a) established net sediment transport rate for uniform grain size bed-load sediments under asymmetric oscillatory flows by PIV technology. Experiments of bed-load effects on turbulent structure under open channel flows was investigated by Campbell et al. (2005)

Because of the complexity of mechanisms sediment transport in open channel flows, most of the numerical models were of 1D and 2D simulations, which usually neglect the influence of secondary flows. Van_Rijn (1987) established a combined model in which the sediment transport is calculated with a 3D approach and the flow with a depth-averaged approach in combination with the assumption of vertical logarithmic velocity profile, which is valid only for gradually varying open channel flow. Wu et al. (2000) presented a 3D numerical model for calculating flow and sediment transport in open channels by considering Reynolds-averaged Navier-Stokes equations together with k-e turbulence model for the flow simulation, a non-equilibrium method for the bed-load transport and an overall mass-balance equation for the bed deformation.

For the fluid-particle interaction problems concerned, the hydrodynamic interactions between solid particles are either ignored or modeled in a simple manner. For the bed-load

sediment transport, especially in sheetflow regime, the concentration is so high that the existence of the sediment particles influences the flow properties. Hence in the numerical simulation, both submechanisms of fluid-particle interaction and particle-particle interaction should be considered. However, studies on the interactions between particles in the fluid are still less (Feng and Michaelides, 2003), because of the complexity and huge computations. Studies on 3D particle-fluid and particle-particle interactions are extremely few, and most of which are done by Gotoh et al. (2002) and Harada and Gotoh (2006), whose 3D granular material model is based on the distinct element method.

1.2.3 Mixed grain size sediment transport under oscillatory flows and progressive waves

The vertical sorting processes of graded sediment is one of the most important part in the cross-shore sediment transport, as field observation show that sea bed sediments are generally composed of a mixture of different grain sizes (Hassan and Ribberink, 2005). In the cross-shore sediment transport, sheetflow is dominant process of shoreline change because a large amount of sediment is transported in sheetflow regime (Gotoh and Sakai, 1997). For this reason, most of the hydrodynamic experiments and numerical simulations are conducted in sheetflow regime.

Diameters of graded sediments used in Hydrodynamic experiments are usually less than 1mm and the specific weight of quartz grains is 2.65. Table 1 listed examples of experimental conditions, including both sediment conditions and oscillatory flow conditions, from some references recently. The experimental condition of Harada and Gotoh (2008) is quite different from the others, because artificial pearls with specific weight of 1.318 and relatively large diameters are used to study the mechanisms of vertical sorting processes of graded sands and as a base for the verification of their numerical model.

Table 1.1 Examples of experimental conditions from some references.

Reference	sediments		Oscillatory flow		
	components of graded sands	Specific weight	Period T (s)	maximum flow velocity (m/s)	theory
Dibajnia and Watanabe, 2000	0.2mm+0.8mm	2.65	3	1.6	first-order cnoidal wave
Ahmed and Sato, 2003b	0.21mm+0.49 mm+0.74mm	2.65	3	1.8	first-order cnoidal wave
Hassan and Ribberink, 2005	0.13mm+0.34 mm+0.97mm	2.65	6.5	1.63	2nd-order Stokes wave
Harada and Gotoh, 2008	5.15mm+9.88 mm+15.6mm	1.318	5	0.85	Sinusoidal wave

For the numerical simulation models, there are typically two kinds of models for the mixed grain size sediments. One is the Euler-Euler coupling model, i.e., two-phase flow model (Dong and Zhang, 1999; Hsu, Jenkins and Liu, 2004), which is good at dealing with fluid-particle interaction but weak at particle-particle interaction. Because both flow model and particle model is Euler, while the motion of particles is Langrangian in the nature. The other is the Langrangian-Euler coupling model (i.e., Wiberg and Smith, 1989; Gotoh and Sakai, 1997; Thaxton and Calantoni, 2006), namely a granular model coupled with one-way or two-way flow models. Although the deficiency of the Eulerian model is improved by the granular model, the behaviors of particles in the granular models are emphasized while the characteristics are mostly simplified. Hence in the dissertation, a 3D movable bed model based on LBM is applied, which includes both fluid-particle interaction and fluid-fluid interaction without much assumption limit.

A series numerical studies of vertical sorting processes of graded sediments has been done by the group of Sakai, Gotoh, Harada et al. **Table 1.2** lists some numerical conditions of their work, as a reference for the numerical condition of the dissertation.

Table 1.2 Numerical conditions applied by the group of Sakai, Gotoh, Harada, et al. in the years from 1996 to 2011.

Reference	period T (s)	Maximum flow velocity Um (cm/s)	Shields Parameter	Specific Weight s	Diameters of graded sediments (mm)				dt
					d1	d2	d3	d4	
Gotoh, Sakai, Toyota, 1996	4.5	106.6	0.619	1.32	5.15	9.88	/	/	
Sakai et al., 1999	6.0	104	0.538	1.318	5.15	9.88	15.6	/	
Gotoh, Yeganeh, Sakai, 2000				2.6	5.0	/	/	/	
Harada,Yeganeh,Gotoh, Sakai, 2000	4.0	80	0.53	2.65	5.0	10.0	/	/	0.00002s
Sakai et al., 2000	3.0 4.0	56 72	0.3 0.34	1.318	5.15	9.88	/	/	
Gotoh, Harada, Sakai, 2001a					0.5	/	/	/	2e-5s
Gotoh, Harada, Sakai, 2001b	5.0	85	0.27	1.318	5.15	9.88	15.6		
Gotoh, Harada, Sakai, 2002	2.0		0.44	2.65	10.0	9.0	7.0	5.0	1e-4s
Harada and Gotoh, 2006/2008	5.0	85	0.27	1.318	5.15	9.88	15.6		
Harada and Gotoh, 2007	5.0		0.3	1.318	4.0	8.5	10.0		
Harada, Gotoh, Turada, 2010	1.0	60	0.4		5.0	10.0	15.0		
Harada, Gotoh, Tsuruda, 2011	5.0	85	0.27	1.318	5.15	9.88	15.6		

1.2.4 The behavior of tsunami drifts

Numbers of both physical experiments and numerical simulations have been done to study the drift behavior in tsunami run-up.

Kumagai et al. (2006) established a simple numerical model coupling with a 2D horizontal tsunami and drift bodies with DEM to study the drift behavior of containers and estimate the collision force.

Tomita and Honda (2010) developed a numerical model with the fluid force simply calculated from fluid models of STOC-IC and STOC-ML without drift bodies, to deal with multiply tsunami-drifted vessels colliding with both floating and fixed bodies.

Kawasaki et al. (2010) proposed a numerical solid-gas-liquid phase flow model, based on CIP method and an extended SMAC method, with a series improvements of resolving mass conservation problem, adding LES, developing from 2D to 3D and extending from single rigid body to multiple rigid bodies.

Nakamura et al. (2012) applied the 3D coupled fluid-structure-sediment interaction model with a main solver based on an extended N-S equation for computing the incompressible viscous air-water multi-phase flow and three modules including VOF module for air-water interface tracking, IB module for movable structure motion and sediment transport module, to analyze the drift behavior of the container more precisely.

1.3 Study Objectives

The present model studies the behavior of particles emerged or sub-emerged in the fluid with a free surface in three-dimensional space, which is more realistic and accurate compared with the 2D models. Numerical models of sediment transport including both particle-particle interaction and particle-fluid interaction are still limited. The present model deals with both particle-fluid interaction and particle-particle interaction by using a link-bounce-back scheme, which will be illustrated in Section 2.3.2. In addition to this, few models consider all three phases of gas-fluid-solid. The present model can simulate the free surface by applying a simple fluid fraction factor, which will be descripted in details in Section 2.4. The turbulence terms can be easily added by modifying the eigenvalues related to shear viscosity in the collision term of distribution functions, which is the base of LBM (Section 2.5). The external forces exerting on particles are added by the modification of DFs (more details can be found in Chapter 2).

Based on the above theory, a simple case of uniform grain size sediment under open channel flows in sheetflow regimes is performed by using this 3D movable bed model. In order to check the feasibility of the present model, the 3D behaviors of the uniform bed-load sediments, including rolling, sliding and saltation are observed, and the typical characteristics of bed-load sediments, i.e. the horizontal velocity and the vertical existing probability density function (P.D.F) of sediments are analyzed.

The knowledge of vertical sorting process of mixed grain size sediment, especially under progressive waves, is still limited. The present study will focus on the processes of vertical sorting of mixed sands, which is essential for further study on the sediment transport of mixed grain size sediment. The main influence factors, such as period, Shields parameters, bottom layer thickness, bottom slope, will be discussed in the cases of mixed sands under oscillatory flows. Besides, the processes of vertical sorting of mixed grain size sediment under a realistic progressive wave will be analyzed.

Another usage of the 3D movable bed model is the simulation of tsunami drifts. To do this, sediment particles with spherical shapes are further modified to tsunami drift automobiles with irregular shape. Successful on doing this, it is possible to simulate sediments with irregular shape by the present model.

1.4 Dissertation Layouts

The present study establishes a 3D numerical movable bed model for the analysis of sediment transport under flows with free surface and the behavior of tsunami drifts. The layout of the dissertation is shown as follows (with a brief flow chart shown in **Fig. 1.3**).

In Chapter 2, detailed descriptions of the theory of basic Lattice Boltzmann Method, Ladd's original LBM model for particle-fluid suspension, Thürey's theory for free surface flows, together with Sub-Grid Smagorinsky (SGS) turbulence model, are given.

In Chapter 3, the present model is used to investigate the sediment transport of bed load with uniform grain size sediment under open channel flows in sheet flow regime. The present model is verified with experimental data of Gotoh et al. (1993, 1994).

In Chapter 4, a series of cases of mixed grain size sediments under oscillatory flows with different flow periods, Shields parameters, bottom layer thicknesses, bottom slope is performed. One case of mixed sands under a progressive cnoidal wave is conducted.

In Chapter 5, unlike the above chapters, in which only sphere particles are used, particles with irregular shapes (represent tsunami drifted automobiles) are simulated in tsunami flooding currents. Based on this, tsunami drifts colliding with the pillars of tsunami evacuation towers are simulated and the behavior of tsunami drifts will be discussed.

In Chapter 6, conclusions including the advantages of the present model are given at first. Physical mechanisms of sediment transport of both uniform grain size sediments and mixed grain size sediments bed-load are illustrated. The behaviors of tsunami drift automobiles are discussed.

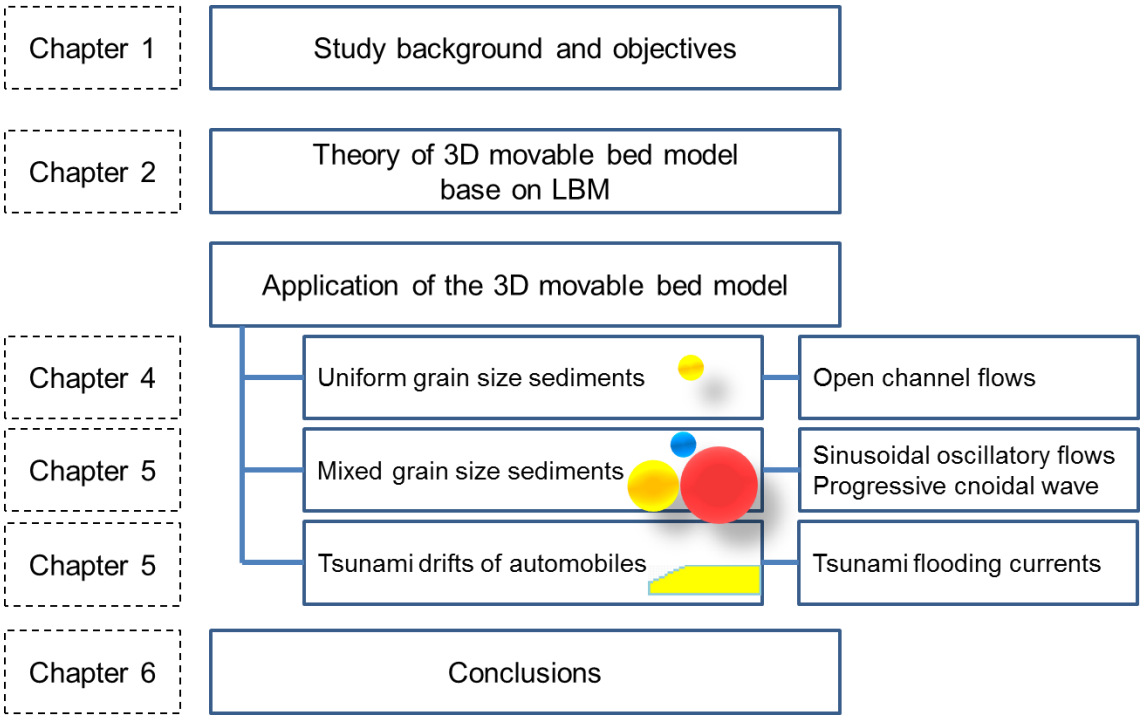

Figure 1.3 Flow Chart of the present dissertation.

CHAPTER 2

LATTICE BOLTZMANN METHOD USED FOR 3D MOVABLE BED

2.1 An Introduction to Lattice Boltzmann Method (LBM)

The Boltzmann equation (BE) has been proposed by the Austrian scientist Ludwig Boltzmann in 1872, and is part of the classical statistical physics that describe the behavior of a gas on the microscopic scale. Originated from the Lattice Gas Automata (LGA), which can be considered as a simplified fictitious molecular dynamics model in which space, time and particle velocities are all discrete, Lattice gas models (Frisch et al., 1987) with an appropriate choice of the lattice symmetry in fact represent numerical solutions of the Navier-Stokes equations and are therefore able to describe macroscopic hydrodynamic problems. Since the first algorithm proposed to model the lattice gas with a BE (McNamara and Zanetti, 1988), LBM has been widely used for the technique to the LGA for the study of hydrodynamic properties. Then the Bhatnagar Gross Krook (BGK) approximation (Bhatnagar, Gross and Krook, 1954) was used to simplify the collision operator with a single time relaxation parameter, which was derived by Chen et al. (1992) and Qian et al. (1992) independently.

Recently, LBM is widely used in fluid dynamics. Thürey and Rüde (2009) conducted free surface flow simulations with LBM on multiple grids. Yu et al., (2005) performed DNS and LES of the classical decaying HIT problems with and without reference frame rotation by using LBM, to conclude that LBM can accurately capture important features of decaying HIT and is potentially a reliable computational tool for turbulence simulations. LBM is also a useful tool to study the mechanism of two-phase or multiphase flows (Shan and Chen, 1993; Swift et al., 1996; Inamuro et al., 2004; Zheng et al., 2006). Lockard et al. (2000) developed commercial fluid solvers based on LBM, which can be used in aerospace,

car companies and so on. LBM can also be applied to solve problems where N-S equations are no longer applicable, e.g., hypersonic or rarefied gas flows (Zheng and Struchtrup, 2004), as it can handle problems with a wide range of Knudsen numbers.

Körner et al. (2006) summarized some typical characteristics of LBM. The main advantages of LBM are the stability, ease of implementation (for free surface, complex geometries and boundary conditions, etc.), ease of extensibility (for turbulent flows, multiphase flows, sediments, etc.) and intrinsic parallel structure allowing high performance computing. However, LBM suffer from some disadvantages: statistical noise, non-Galilean invariance, a velocity dependent pressure and spurious invariants. Particularly, the statistical noise requires time and/or space averaging procedures to extract macroscopic quantities like the density or the velocity.

2.2 Basic Algorithm of LBM

2.2.1 Boltzmann equation

The Boltzmann equation is a partial differential equation (PDE) describing the evolution of the single particle distribution function (DF) f in phase space. The DF f ($\mathbf{x}$, $\boldsymbol{\xi}$, t) is the probability for particles to be located within a phase space control element d$\mathbf{x}$ d$\boldsymbol{\xi}$ about $\mathbf{x}$ and $\boldsymbol{\xi}$ at time t where $\mathbf{x}$ and $\boldsymbol{\xi}$ are the spatial position vector and the particle velocity vector, respectively.

The Boltzmann equation can be expressed as a function of DF,

$$\frac{\partial f}{\partial t} + \boldsymbol{\xi} \frac{\partial f}{\partial \mathbf{x}} = \left(\frac{df}{dt} \right)_{coll} \tag{2.1}$$

The collision operator $(df/dt)_{coll}$ is quadratic in f, consisting of a complex integro-differential expression. A simple form for the collision operator is the Bhatnagar-Gross-Krook (BGK) scheme,

$$\left(\frac{df}{dt}\right)_{coll} = -\frac{f - f^{eq}}{\tau} \tag{2.2}$$

where the relaxation time τ is an empirical parameter, and f^{eq} is the equilibrium Maxwell-Boltzmann distribution. f^{eq} can be shown as

$$f^{eq} = \frac{\rho}{m}\left(\frac{m}{2\pi k_B T}\right)^{3/2} \exp\left(\frac{-m(\xi - \mathbf{u})\cdot(\xi - \mathbf{u})}{2k_B T}\right) \tag{2.3}$$

where m is the molecular mass, k_B is the Boltzmann constant, ρ is the density, $\mathbf{u}$ is the fluid velocity and T is the fluid temperature. The BGK scheme is suitable for the near equilibrium state of low Mach number hydrodynamics and fulfills Boltzmann's H-theorem and locally conserves mass and momentum.

2.2.2 Discrete Boltzmann approximation

To solve for DF f numerically, Eq. (2.1) is discretized in the velocity space using a finite set of velocity vectors $\mathbf{e}_i$ (i=0, …, N) leading to the velocity discrete Boltzmann Equation

$$\frac{\partial f_i}{\partial t} + \mathbf{e}_i \frac{\partial f_i}{\partial \mathbf{x}} = -\frac{f_i - f_i^{eq}}{\tau} \tag{2.4}$$

where $f_i(\mathbf{x}, t)$ is equivalent to $f(\mathbf{x}, \mathbf{e}_i, t)$.

Based on the discrete distribution functions, the LBM can be classified by different methods of lattice, the DnQm scheme. Here "Dn" stands for "n dimensions" while "Qm" stands for "m speeds". **Figure 2.1** shows some popular examples of DnQm LBM models. For instance, D3Q15 model is a three dimensional lattice Boltzmann model on a cubic grid with the discretized distribution functions fi directed for 15 directions: 14 DFs associated with the particles moving to the neighboring cells and 1 DF corresponding to the resting particles.

Generally for DnQm models, a suitable form for equilibrium distribution function (EDF) f_i^{eq} is given as

$$f_i^{eq} = \rho w_i \left(1 + \frac{\mathbf{u} \cdot \mathbf{e}_i}{c_s^2} + \frac{(\mathbf{u} \cdot \mathbf{e}_i)^2}{2c_s^4} - \frac{\mathbf{u} \cdot \mathbf{u}}{2c_s^2} \right) \tag{2.5}$$

where $c_s = \sqrt{k_B T / m} = c/\sqrt{3}$ is the sound speed with $c = \Delta x / \Delta t$, w_i is the weighting factors, which depend only on the lattice model Qian et al. (1992).

Then the macroscopic values of mass density ρ, momentum density **j** and momentum flux **Π** can be obtained through the following equations

$$\rho = \int_{-\infty}^{\infty} f d\xi = \sum_{i=0}^{N} f_i = \sum_{i=0}^{N} f_i^{eq} \tag{2.6}$$

$$\mathbf{j} = \rho \mathbf{u} = \int_{-\infty}^{\infty} \xi f d\xi = \sum_{i=0}^{N} \mathbf{e}_i f_i = \sum_{i=0}^{N} \mathbf{e}_i f_i^{eq} \tag{2.7}$$

$$\mathbf{\Pi} = \rho \mathbf{u}\mathbf{u} = \int_{-\infty}^{\infty} \xi_\alpha \xi_\beta f d\xi = \sum_{i=0}^{N} \mathbf{e}_{i\alpha} \mathbf{e}_{i\beta} f_i = \sum_{i=0}^{N} \mathbf{e}_{i\alpha} \mathbf{e}_{i\beta} f_i^{eq} \tag{2.8}$$

And the pressure can be given by the equation of state of an ideal gas

$$p = \rho c_s^2 \tag{2.9}$$

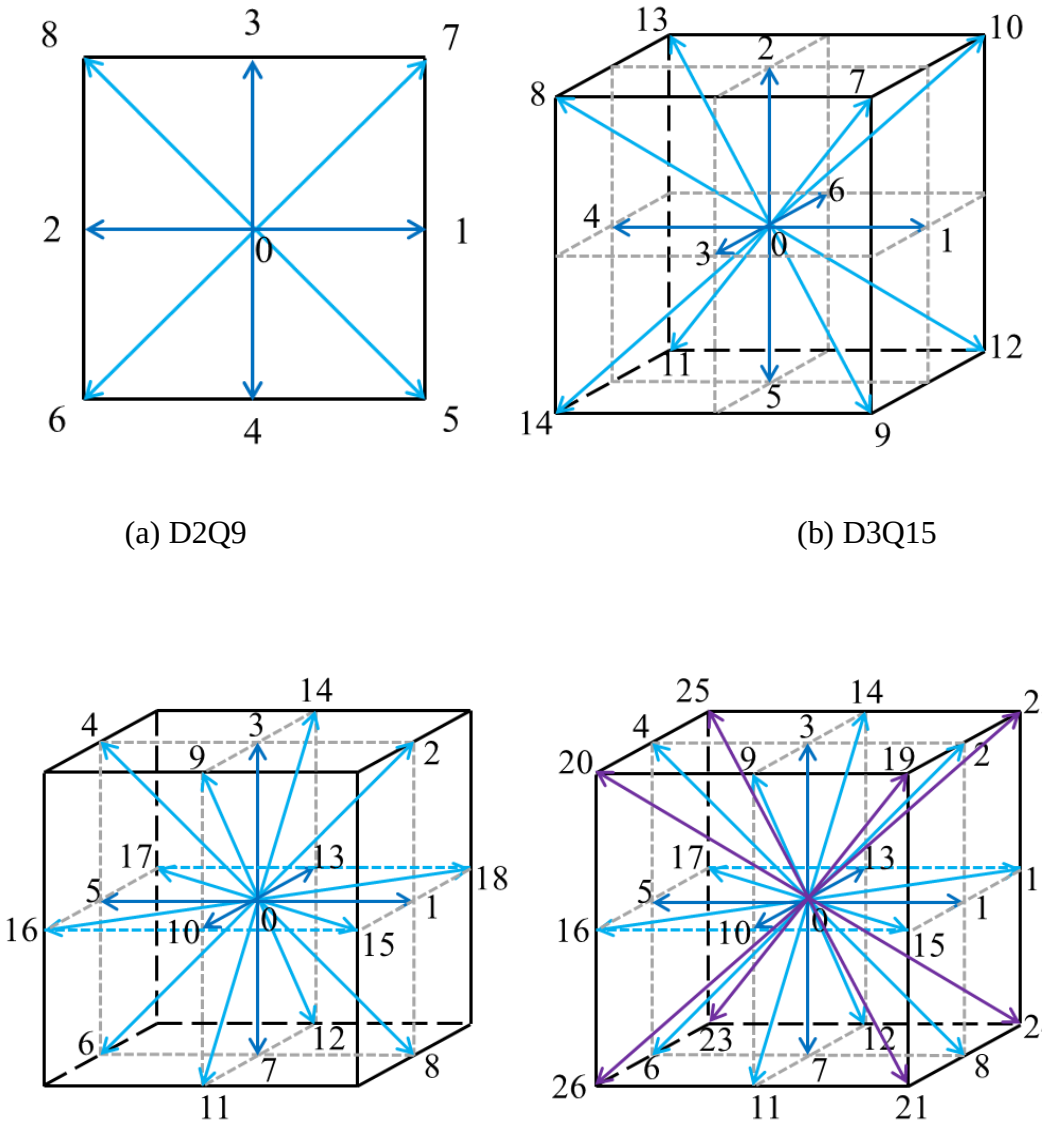

(a) D2Q9 (b) D3Q15

(c) D3Q19 (d) D3Q27

Figure 2.1 Discretized distribution functions fi for the DnQm models.

2.2.3 Basic steps for computation

The basic LBM algorithm consists of two steps; the streaming step and the collision step. For clarity, take D2Q9 model for an example. **Figure 2.2** shows the streaming and collision processes for an individual fluid lattice in a single loop. At the initial of a typical loop, namely before streaming, the fraction of particles moving with a certain velocity of an independent lattice is represented by the DF f_i. During the streaming step, all DFs are advected to their adjacent fluid lattices with the corresponding velocity direction. After the streaming step, the post-streaming DFs can be expressed as

$$f_i^*(\mathbf{x}, t+\Delta t) = f_i(\mathbf{x}+\mathbf{e}_{\tilde{i}}\Delta t, t) \tag{2.10}$$

where the subscript $\tilde{i}$ denotes the anti-parallel lattice vector, namely $\mathbf{e}_{\tilde{i}} = -\mathbf{e}_i$.

With all DFs of the current lattice streamed from the neighbor lattices, collision occurs in the local lattice. And the DFs after collision step can be obtained by

$$f_i(\mathbf{x}, t+\Delta t) = (1-\frac{1}{\tau}) f_i^*(\mathbf{x}, t+\Delta t) + \frac{1}{\tau} f_i^{eq} \tag{2.11}$$

The relaxation time parameter τ controls the viscosity of the fluid and has a range of [0.5, ∞), when τ near 0.5 results in very turbulent flow and τ close to ∞ results in very viscous fluids.

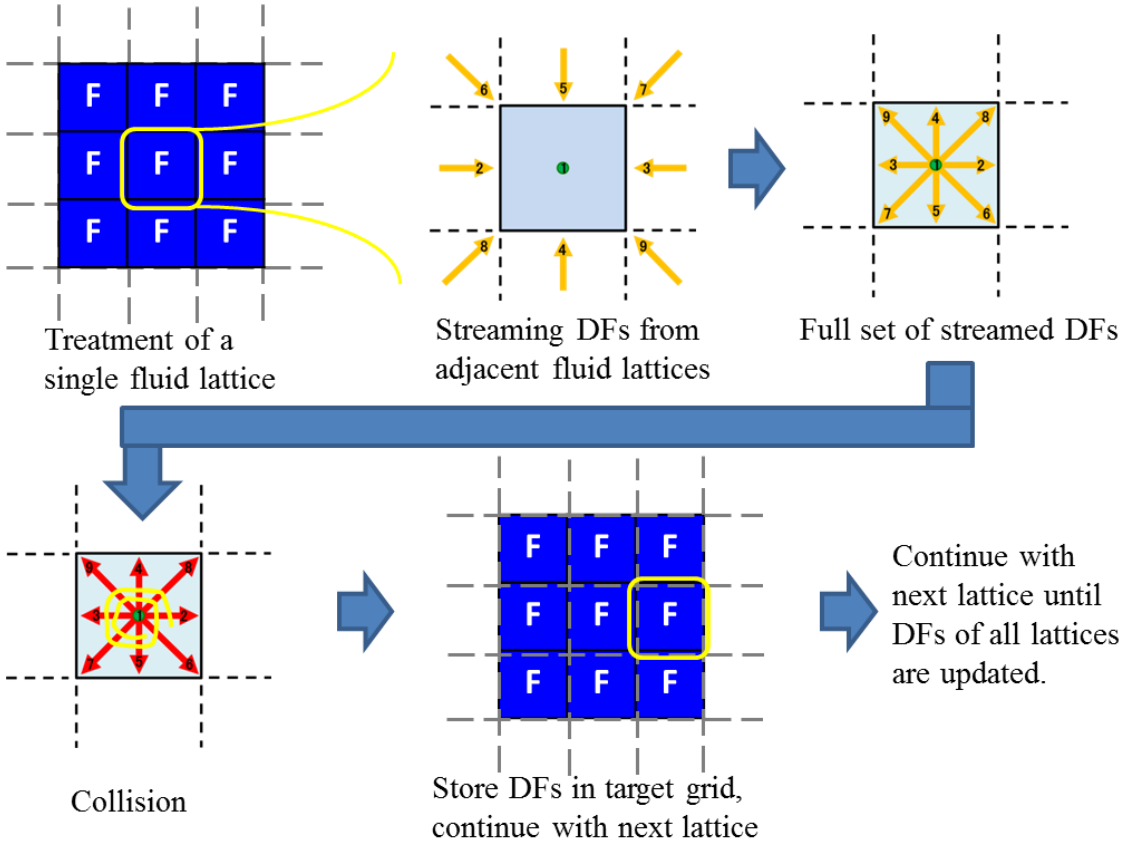

Figure 2.2 Streaming and collision steps for a fluid lattice.

2.3 Ladd's LBM for Particle-Fluid Suspension

In Lattice Boltzmann Method (LBM), the macroscopic fluid can be represented by an aggregation of microscopic virtual particles moving on lattices, and the flow of fluid can be obtained through the calculation of time evolution of streaming and collision processes of these virtual particles. According to Ladd's (1994a, b) LBM model, the interaction force between fluid and movable solid particles can be calculated from the exchange of momentum, applying the link-bounce-back scheme for the movable solid particles in the fluid.

D3Q19 lattice model (**Fig. 2.3**) is used, as it is necessary to determine the macroscopic

variables, momentum flux in addition to density and velocity from the velocity Distribution Function. The velocity vectors $\mathbf{e}_i$ (i=0, 1, ..., 18) of each single lattice are given as follows 0 (i=0), e (i=1, 2, 3, 4, 5, 6), $\sqrt{2}e$ (i=7, 8, …, 18), where $e=\Delta x/\Delta t$ (Δx and Δt are lattice interval in space and time, respectively).

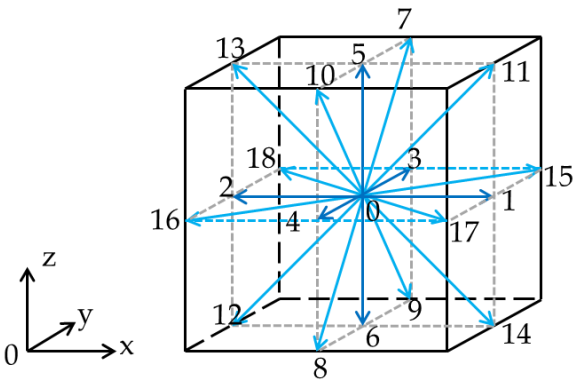

Figure 2.3 Schematic diagram of D3Q19 LBM model.

2.3.1 Discrete Boltzmann approach

The discrete Boltzmann equation describing the time evolution of the distribution function $f_i(\mathbf{x},t)$, which is analogous to Eq. (2.11), is shown as

$$f_i(\mathbf{x}+e_i\Delta t, t+\Delta t) = f_i(\mathbf{x},t)+\Delta_i(\mathbf{x},t) \tag{2.12}$$

where $\Delta_i(\mathbf{x},t)$ is the change in f_i due to molecular collisions. The basic Boltzmann algorithm consists two steps: one is the streaming step and the other is the collision step. During the stream step, virtual particles move along the velocity direction from the adjacent lattices to the current lattice. During the collision step, the virtual particles are redistributed with a percentage of Δ_i to a local equilibrium state.

$$\Delta_i(f) = \Delta_i\left(f^{eq}\right)+\sum_j \ell_{ij} n_j^{neq} \tag{2.13}$$

where ℓ_{ij} are the matrix elements of the linearized collision operator, n_j^{neq} is the

non-equilibrium distribution function from the equation of $n_j = n_j^{eq} + n_j^{neq}$, and $\Delta_i\left(f^{eq}\right) = 0$.

Analogous to Eq. (2.5), the EDF can be expressed as a series expansion in powers of the flow velocity **u**,

$$f_i^{eq} = \rho\left\lfloor a_0^{e_i} + a_1^{e_i}\mathbf{u}\cdot\mathbf{e}_i + a_2^{e_i}\overline{\mathbf{uu}}:\overline{\mathbf{e}_i\mathbf{e}_i} + a_3^{e_i}u^2\right\rfloor \tag{2.14}$$

where $\overline{\mathbf{uu}} = \mathbf{uu} - (1/3)u^2\mathbf{1}$ is the traceless part of **uu**. And the coefficients of weights $a_i^{e_i}$ can be derived from a series of equation of moments with EDF

$$\rho = \sum_i f_i^{eq}, \qquad \rho\mathbf{u} = \mathbf{j} = \sum_i f_i^{eq}\mathbf{e}_i, \qquad \prod^{eq} = \sum_i f_i^{eq}\mathbf{e}_i\mathbf{e}_i = p\mathbf{1} + \rho\mathbf{uu} \tag{2.15}$$

For a D3Q19 model, the coefficients are

$$a^0 = \frac{1}{3}, \qquad a^1 = \frac{1}{18}, \qquad a^{\sqrt{2}} = \frac{1}{36} \tag{2.16}$$

and the EDF for a stationary particle is then revised as

$$f_i^{eq} = a^{e_i}\left[\rho + \frac{\mathbf{j}\cdot\mathbf{e}_i}{c_s^2} + \frac{\rho\mathbf{uu}:\left(\mathbf{e}_i\mathbf{e}_i - c_s^2\mathbf{1}\right)}{2c_s^4}\right] \tag{2.17}$$

The particle distribution function of the next step, namely the post-collision DF, ($f_i^* = f_i + \Delta_i$), can be calculated as

$$f_i^* = a^{e_i}\left(\rho + \frac{\mathbf{j}\cdot\mathbf{e}_i}{c_s^2} + \frac{\left(\rho\mathbf{uu} + \prod^{neq,*}\right):\left(\mathbf{e}_i\mathbf{e}_i - c_s^2\mathbf{1}\right)}{2c_s^4}\right) \tag{2.18}$$

where **1** is the unit tensor, and and c_s is the speed of sound, expressed with a function of virtual particle velocity e, $c_s = \sqrt{e^2/3}$. The pressure is determined by the ideal gas equation of state, $p = \rho c_s^2$.

The post-collision non-equilibrium momentum flux in the above equation is calculated as

$$\Pi^{neq,*} = (1+\lambda)\overline{\Pi}^{neq} + \frac{1}{3}(1+\lambda_v)(\Pi^{neq} : \mathbf{1}) \tag{2.19}$$

Here the eigenvalues λ and λ_v are related to shear and bulk viscosities, respectively, and λ lies in the range of $-2 < \lambda < 0$. The overbar indicates the traceless projection. The non-equilibrium momentum flux $\mathbf{\Pi}^{neq}$ can be obtained directly by subtracting the equilibrium momentum flux $\mathbf{\Pi}^{eq}$ from the total momentum flux $\mathbf{\Pi}$.

$$\Pi^{neq} = \Pi - \Pi^{eq} \tag{2.20}$$

$$\Pi^{eq} = \sum_i f_i^{eq} \mathbf{e}_i \mathbf{e}_i = p\mathbf{1} + \rho \mathbf{u}\mathbf{u} \tag{2.21}$$

The shear and bulk viscosities are respectively

$$\eta = -\rho c_s^2 \Delta t (\frac{1}{\lambda} + \frac{1}{2}) \qquad \text{and} \qquad \eta_v = -\rho c_s^2 \Delta t (\frac{2}{3\lambda_v} + \frac{1}{3}) . \tag{2.22}$$

Based on the above equations, the continuous equation and Navier-Stokes equations recovered in the low velocity limit can be shown as

$$\partial_t \rho + \nabla \cdot (\rho \mathbf{u}) = 0 \tag{2.23}$$

$$\partial_t (\rho \mathbf{u}) + \nabla \cdot (\rho \mathbf{u}\mathbf{u}) + \nabla \rho c_s^2 = \eta \nabla^2 \mathbf{u} + (\eta + \eta_v) \nabla (\nabla \cdot \mathbf{u}) \tag{2.24}$$

2.3.2 Link-Bounce-Back scheme

The link-bounce-back collision rule is applied for the moving boundary condition of a solid particle. It is assumed that the surface of an individual particle is constructed by a series of boundary nodes which locate in the center of fluid nodes and solid nodes (**Fig. 2.4**). The velocities along links cutting the boundary surface are represented by arrows. Set the location of fluid node just outside the particle surface as $\mathbf{x}$ and the position of solid node adjacent to the particle surface as $\mathbf{x}+\mathbf{e}_b \Delta t$ (the subscript $_b$ represents the solid

boundary node), then each of the corresponding population densities is updated according to a simple rule which takes into account the motion of the particle surface. **Figure 2.5** shows the momentum transfers between DFs of fluid nodes and boundary nodes. It should be emphasized that the velocity components transfer parallel to the 18 DF directions. Hence, the DFs of moving boundary node can be updated from

$$f_{\tilde{b}}(\mathbf{x}, t+\Delta t) = f_b^*(\mathbf{x}, t) - \frac{2a^{e_b}\rho_0 \mathbf{u}_b \cdot \mathbf{e}_b}{c_s^2} \tag{2.25}$$

where $f_b^*(\mathbf{x},t)$ is the post-collision DF at ($\mathbf{x}$, t) in the direction $\mathbf{e}_b$, a^{e_b} is the coefficient of weights, ρ_0 is the mean density used to simplify the update procedure, and the subscript $\tilde{b}$, the same to $\tilde{i}$ in Eq. (2.10), denotes the anti-parallel lattice vector, namely, $\mathbf{e}_{\tilde{b}} = -\mathbf{e}_b$. The local velocity of the particle surface $\mathbf{u}_b$ is determined by the particle velocity **U**, angular velocity **Ω** and the center of the mass **R**, shown as

$$\mathbf{u}_b = \mathbf{U} + \mathbf{\Omega} \times (\mathbf{x}_b - \mathbf{R}) \tag{2.26}$$

where $\mathbf{x}_b$ is the location of surface boundary node, $\mathbf{x}_b$ =**x**+1/2 $\mathbf{e}_b \Delta t$. Originally, the bounce-back method (Ladd, 1994a) is assumed with fluid filled inside of the particle. However, it is impossible to treat a solid particle as a rigid body, as time lag of momentum exchange exists due to the inertia of fluid inside the particle. As a result, the method proposed by Aidun (1998), in which no fluid is included inside particles and momentum exchange only occurs at the boundary nodes of particle surfaces, is applied.

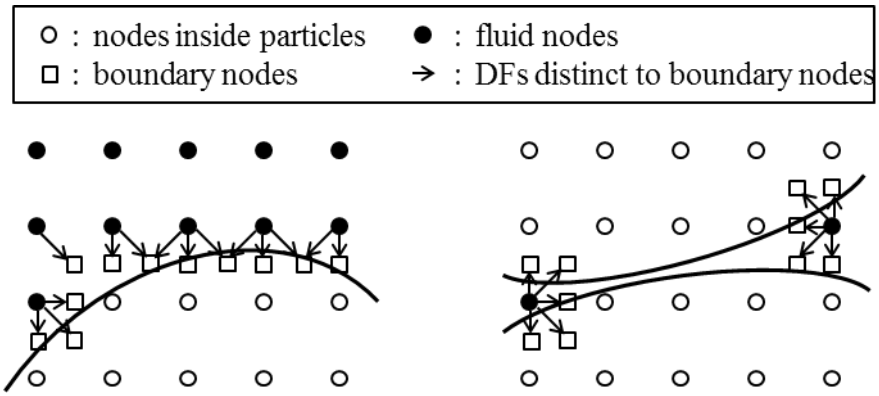

(a) Boundary nodes for sphere particles

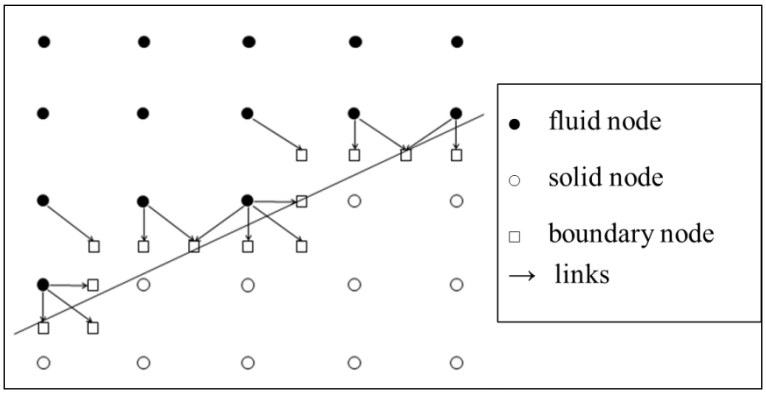

(b) Boundary nodes for automobiles with irregular particles

Figure 2.4 The surface boundary nodes of curved particles.

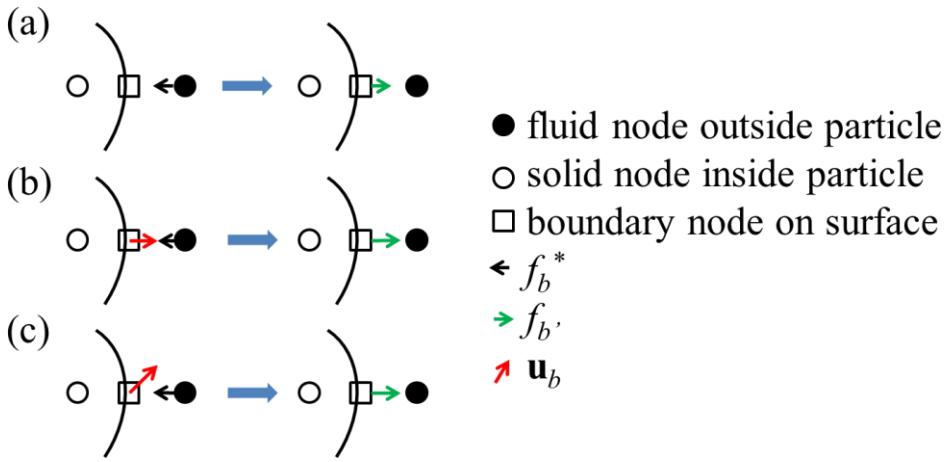

Figure 2.5 DFs before and after collision with stationary (a) and moving (b, c) boundary nodes.

The external force **F** and torque **T** exerted on particles are composed of external forces (i.e., gravity force), forces depending on the incoming DFs, and forces related to the particle velocity **U** and angular velocity **Ω**.

$$\mathbf{F} = \mathbf{F}_0 + \mathbf{F}_{ext} - \zeta^{\mathrm{FU}} \cdot \mathbf{U} - \zeta^{\mathrm{F\Omega}} \cdot \mathbf{\Omega} \tag{2.27}$$

$$\mathbf{T} = \mathbf{T}_0 - \zeta^{\mathrm{TU}} \cdot \mathbf{U} - \zeta^{\mathrm{T\Omega}} \cdot \mathbf{\Omega} \tag{2.28}$$

where ζ^{FU}, $\zeta^{\mathrm{F\Omega}}$, ζ^{TU} and $\zeta^{\mathrm{T\Omega}}$ are high-frequency friction coefficients (Nguyen and Ladd, 2002). The velocity independent forces $\mathbf{F}_0$ and torques $\mathbf{T}_0$, are calculated at the half-time step, as

$$\mathbf{F}_0\left(t+\frac{1}{2}\Delta t\right) = \frac{\Delta x^3}{\Delta t}\sum_b 2 f_b^*(\mathbf{x},t)\mathbf{e}_b \tag{2.29}$$

$$\mathbf{T}_0\left(t+\frac{1}{2}\Delta t\right) = \frac{\Delta x^3}{\Delta t}\sum_b 2 f_b^*(\mathbf{x},t)(\mathbf{x}_b \times \mathbf{e}_b) \tag{2.30}$$

Then the particle velocity **U** and angular velocity **Ω** of the next time step are updated implicitly

$$\begin{bmatrix}\mathbf{U}(t+\Delta t)\\ \mathbf{\Omega}(\mathrm{t}+\Delta\mathrm{t})\end{bmatrix} = \begin{bmatrix}\mathbf{U}(t)\\ \mathbf{\Omega}(t)\end{bmatrix} + \begin{bmatrix}\frac{m}{\Delta t}\mathbf{1}+\zeta^{\mathrm{FU}} & \zeta^{\mathrm{F\Omega}}\\ \zeta^{\mathrm{TU}} & \frac{I}{\Delta t}\mathbf{1}+\zeta^{\mathrm{T\Omega}}\end{bmatrix}^{-1} \times \begin{bmatrix}\mathbf{F}\\ \mathbf{\Omega}\end{bmatrix} \tag{2.31}$$

where m is the mass, and I is the inertia momentum.

With the updated velocity and angular velocity, the new position of an individual particle is finally updated with the following simple equations:

$$\mathbf{x}_b(t+\Delta t) = \mathbf{x}_b(t) + \mathbf{U}(t+\Delta t)\Delta t \tag{2.32}$$

$$\mathbf{\theta}(t+\Delta t) = \mathbf{\theta}(t) + \mathbf{\Omega}(t+\Delta t)\Delta t \tag{2.33}$$

2.3.3 Lubrication forces

When two particles get close to each other or particles imping on a wall, a strong repulsive forces occurs, which is caused by fluid between the particles being squeezed out. These lubrication flows generate very high pressures in the gap and are difficult to be solved. However, Nguyen and Ladd (2002) proposed a method to incorporate into a lattice Boltzmann simulation as

$$\mathbf{F}_{ij}^{\mathrm{lub}} = -\frac{6\pi\eta(a_1 a_2)^2}{(a_1+a_2)^2}\mathbf{R}_{ij}\mathbf{R}_{ij}\cdot(\mathbf{u}_i-\mathbf{u}_j)\left(\frac{1}{R_{ij}-a_1-a_2}-\frac{1}{\Delta_c}\right) \tag{2.34}$$

where a_1 and a_2 are the radii of the particles, Δ_c is the cut off for the added lubrication force, including the normal Δ_{cN} , tangential Δ_{cT} and rotational Δ_{cR} components. R_{ij}-a_1-a_2 is the gap between two particles. When gaps are smaller than Δ_c, the lubrication forces work, otherwise $\mathbf{F}_{ij}^{\mathrm{lub}} = 0$.

Some empirical cut off distance of lubrication forces are listed in Table 2.1 (Nguyen and Ladd, 2002). $\nu^* = \nu\Delta t/\Delta x^2$ is the dimensionless kinematic viscosity.

Table 2.1 Lubrication ranges for various kinematic viscosities, determined for a sphere of radius a = 8.2Δx, the ranges are determined separately for the normal Δ_{cN}, tangential Δ_{cT} and rotational Δ_{cR} motions.

	Δ_{cN}/Δx	Δ_{cT}/Δx	Δ_{cR}/Δx
ν^*=1/6	0.67	0.50	0.43
ν^*=1/100	0.24	0.50	0.15
ν^*=1/1200	0.10	0.50	0.00

2.4 LBM with Free Surface Flow

For the simulation of free-surface interface, the method proposed by Thürey (2007), in which a fluid fraction parameter ε is used to distinguish fluid (ε=1), gas (ε=0) and interface lattices ($0<\varepsilon<1$), shown in **Fig. 2.6**, is applied. With this marking method, tracking of the free surface is feasible in the simulation. This can be done by the following steps (**Fig. 2.7**): calculation of mass exchange, computation of the gas lattice next to an interface lattice, the ordinary streaming and collision processes, re-initialization lattice types and redistribution extra mass to the surrounding lattices.

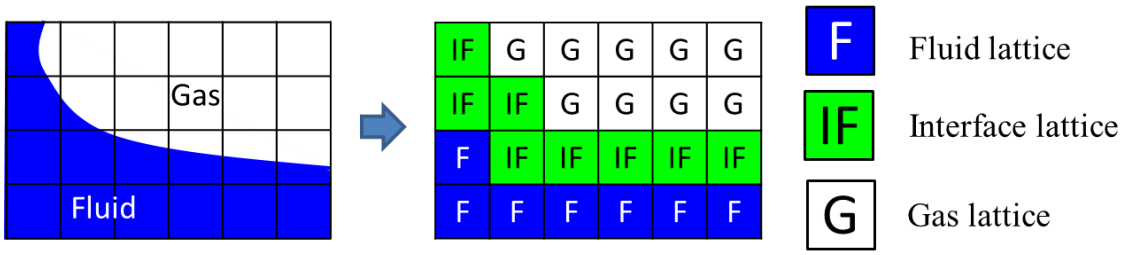

Figure 2.6 Schematic graph of three lattice types.

From the fluid fraction computed with the lattice mass m and density ρ, $\varepsilon=m/\rho$, the movement of the fluid interface is traced by the calculation of the mass that is contained in each lattice. It is assumed that the mas exchange only happens between a fluid lattice and an interface lattice or between interface lattices. For an interface lattice and a fluid lattice at $\mathbf{x}_{nb} = (\mathbf{x}+\mathbf{e}_{nb}\Delta t)$, the exchanged mass is

$$\Delta m_i(\mathbf{x},t+\Delta t) = f_{\tilde{i}}(\mathbf{x}+\mathbf{e}_i\Delta t,t) - f_i(\mathbf{x},t) \tag{2.35}$$

When the mass exchange occurs for two interface lattices, the area of the fluid interface between these two lattices is considered. This is approximated by averaging the fluid fraction values of the two lattices, and the exchanged mass between them becomes

$$\Delta m_i(\mathbf{x},t+\Delta t) = Se\frac{\varepsilon(\mathbf{x}+\mathbf{e}_i\Delta t,t)+\varepsilon(\mathbf{x},t)}{2} \tag{2.36}$$

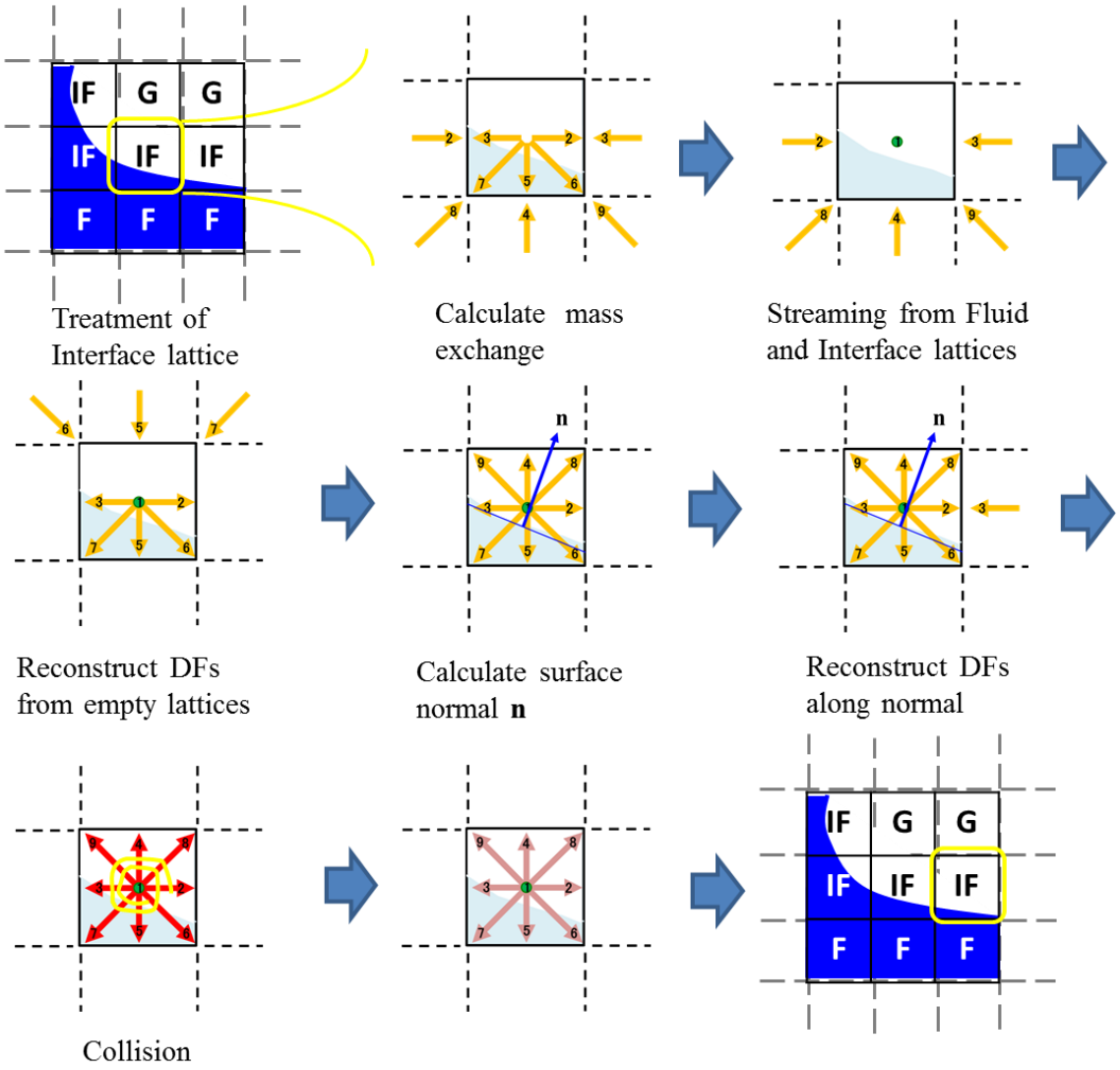

Figure 2.7 Streaming and collision of an interface lattice.

where *Se* is determined by the type of interface lattices surrounded by three different types of lattices, namely Type A, Type B and Type C shown in **Fig. 2.8**. The corresponding *Se* is listed in Table 2.2. With the results from Eq. (2.31) and Eq. (2.32), the total mass for the next time step is computed as

$$m(\mathbf{x},t+\Delta t)=m(\mathbf{x},t)+\sum\Delta m_i(\mathbf{x},t+\Delta t) \tag{2.37}$$

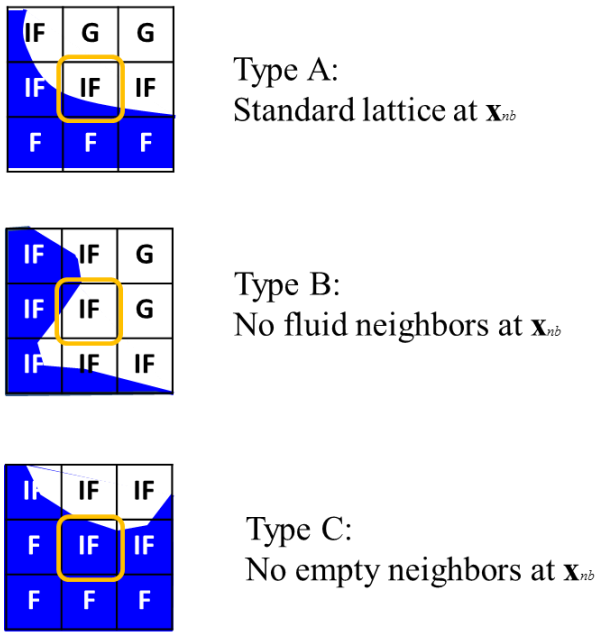

Figure 2.8 Three typical lattice types of interface lattice.

Table 2.2 Different value of *Se* in Eq. (2.32).

	Type A	Type B	Type C
Type A	$f_{\tilde{i}}(\mathbf{x}+\mathbf{e}_i\Delta t,t)-f_i(\mathbf{x},t)$	$f_{\tilde{i}}(\mathbf{x}+\mathbf{e}_i\Delta t,t)$	$-f_i(\mathbf{x},t)$
Type B	$-f_i(\mathbf{x},t)$	$f_{\tilde{i}}(\mathbf{x}+\mathbf{e}_i\Delta t,t)-f_i(\mathbf{x},t)$	$-f_i(\mathbf{x},t)$
Type C	$f_{\tilde{i}}(\mathbf{x}+\mathbf{e}_i\Delta t,t)$	$f_{\tilde{i}}(\mathbf{x}+\mathbf{e}_i\Delta t,t)$	$f_{\tilde{i}}(\mathbf{x}+\mathbf{e}_i\Delta t,t)-f_i(\mathbf{x},t)$

When a gas lattice is next to an interface lattice, it is assumed that the atmosphere has a pressure of $\rho_G=\rho$ and the fluid has a much lower kinematic viscosity. Hence, the gas at the interface simply flows along the direction which is pushed by the fluid. Then the DFs from the gas lattice is modified with the following equation:

$$f_i(\mathbf{x},t+\Delta t)=f_{\tilde{i}}^{eq}(\rho_G,\mathbf{u})+f_i^{eq}(\rho_G,\mathbf{u})-f_{\tilde{i}}(\mathbf{x},t) \tag{2.38}$$

With all DFs for the interface lattice, the density is calculated during the collision step and then the updated density is used to check whether the interface lattice filled or emptied by the following equations:

$$\begin{cases} m(\mathbf{x}, t+\Delta t) > (1+\kappa)\rho(\mathbf{x}, t+\Delta t) & \text{lattice filled} \\ m(\mathbf{x}, t+\Delta t) < (0-\kappa)\rho(\mathbf{x}, t+\Delta t) & \text{lattice emptied} \end{cases} \tag{2.39}$$

where κ is an additional offset with a value of 10^{-3}. The extra mass caused by lattice type change is then redistributed to its neighbour lattices to ensure the mass conservation.

$$m(\mathbf{x}+\mathbf{e}_i\Delta t) = m(\mathbf{x}+\mathbf{e}_i\Delta t) + m^{ex}(\eta_i / \eta_{total}) \tag{2.40}$$

where η_i is the weights determined by a function of the normal **n** and $\mathbf{e}_i$, and η_{total} is the sum of all weights η_i.

$$\begin{aligned} \eta_i &= \begin{cases} \mathbf{n}\cdot\mathbf{e}_i & \text{if } \mathbf{n}\cdot\mathbf{e}_i > 0 \\ 0 & \text{otherwise} \end{cases} && \text{for filled lattice} \\ \eta_i &= \begin{cases} -\mathbf{n}\cdot\mathbf{e}_i & \text{if } \mathbf{n}\cdot\mathbf{e}_i < 0 \\ 0 & \text{otherwise} \end{cases} && \text{for emptied lattice} \end{aligned} \tag{2.41}$$

$$\mathbf{n} = \frac{1}{2}\begin{pmatrix} \varepsilon_{i-1,j,k} - \varepsilon_{i+1,j,k} \\ \varepsilon_{i,j-1,k} - \varepsilon_{i,j+1,k} \\ \varepsilon_{i,j,k-1} - \varepsilon_{i,j,k+1} \end{pmatrix} \tag{2.42}$$

The extra mass can be calculated from

$$\begin{cases} m^{ex} = m(\mathbf{x}, t+\Delta t) - \rho(\mathbf{x}, t+\Delta t) & \text{lattice filled} \\ m^{ex} = m(\mathbf{x}, t+\Delta t) & \text{lattice emptied} \end{cases} \tag{2.43}$$

2.5 LBM with SGS Turbulence Term

The SGS turbulence term based on Smagorinsky model (Smagorinsky 1958, 1963) is added to the collision term of the general Lattice Boltzmann Equation (LBE) with BGK approximation. Specifically, the eddy viscosity coefficient ν_t of SGS turbulence term is added to the normal kinematic viscosity coefficient ν, resulting with a total kinematic viscosity $\nu_{total} = \nu + \nu_t$. The relaxation time ($\tau$ = -1 / λ) related to kinematic viscosity is then revised with

$$\frac{1}{\lambda} = -\left(\frac{v_{total}}{c_s^2 \Delta t} + \frac{1}{2} \right) \tag{2.44}$$

The Equation of Smagorinsky eddy viscosity is given in the form

$$v_t = (C\Delta x)^2 |S| \tag{2.45}$$

where $|S|$ is the magnitude of the local stress tensor, C is Smagorinsky constant and Δx is the lattice length. Since the filter length is assumed here less than $2\Delta x$, a Smagorinsky constant of C=0.1 is applied. The local stress tensor in LBM model is determined as follows:

$$|S| = \frac{\sqrt{v^2 + 18(C\Delta x)^2 (Q_{ij} Q_{ij})^{1/2}} - v}{6(C\Delta x)^2} \tag{2.46}$$

where

$$Q_{ij} = \sum_{\alpha} e_{\alpha i} e_{\alpha j} (f_\alpha - f_\alpha^{eq}) \tag{2.47}$$

CHAPTER 3

THE BEHAVIOR OF UNIFORM GRAIN SIZE SEDIMENTS UNDER OPEN CHANNEL FLOWS

3.1 Introduction

For the fluid-particle interaction problems concerned, the hydrodynamic interactions between solid particles are either ignored or modeled in a simple manner. For the bed-load sediment transport, especially in sheetflow regime, the concentration is so high that the existence of the sediment particles influences the flow properties. Hence in the numerical simulation, both sub-mechanisms of fluid-particle interaction and particle-particle interaction should be considered. However, research on the fluid-particle interaction and particle-particle interaction is still limited. Most of the experiments focus on the sediment transport rate (e.g. Ribberink, 1998; Dibajnia and Watanabe, 2000; Ahmed and Sato, 2003) except Harada and Gotoh (2008), who use relatively larger but lighter artificial pearl to study particles behaviors in the fluid.

For the numerical simulation, there are typically two kinds of models for particle motions in bed-load transport: the two-phase flow model and the granular model. Few studies emphasize both particle-particle interaction and particle-fluid interaction. Feng and Michaelides (2003) applied LBM, originally from Ladd's particle-fluid suspension model, to study the behavior of particle motions in 2D space. More recently, a granular model with a combination of Discrete Element Method (DEM) for the motion of particles and discrete Boltzmann equation for the solution of fluid is proposed by Feng et al. (2010). Studies on 3D particle-fluid and particle-particle interactions are extremely few, and most of which are done by Gotoh et al. (2002) and Harada and Gotoh (2008), whose 3D granular material model is based on the Distinct Element Method.

In this chapter, the present model is applied to study the particle motion of uniform grain size sediments under open channel shear flows. Cases with different Shields parameters ranged between 0.01 and 0.42 under the same still water depth of 8.3cm are performed. The direct description of movement of sediment particles are detected through the computational snapshots and the trajectories of individual sediment particles selected from bottom to top. Besides, statistical results, including the horizontal velocity distribution of sediment particles and vertical existing particle density function, are also given. For the verification of the present model, the simulated statistical results are compared to the experimental data of Gotoh et al. (1993, 1994).

3.2 Numerical Conditions

3000 sphere particles with the same diameter of 0.5cm and specific weight of 2.6 were set almost uniformly at the bottom of an open channel with a length of 32.0cm, width of 4.0cm, water depth of 8.3cm (**Fig. 3.1**). Logarithmic flow velocity distribution is assumed at the upstream side and transmission condition is imposed at the downstream side of the computation domain. No-slip boundary condition is used for the bottom and slip boundary conditions are applied for the front and back walls. Based on these conditions, the behavior of bed-load layer is simulated.

The pressure gradient in the open channel flow is approximately equal to a constant increase of momentum flux $\Delta\mathbf{j}$ along x-direction, and Δj_x is calculated from the following equation:

$$\Delta j_x = \frac{U_{0max} \cdot 8\eta}{B^2} \tag{3.1}$$

where U_{0max} is maximum flow velocity of the upstream, and B is the flume width.

The kinematic viscosity is expressed in the form

$$\eta = -\frac{\rho\left(\frac{2}{\lambda}+1\right)}{6} \tag{3.2}$$

A serious of numerical simulations is performed with different Shields parameter τ^*, which is determined by

$$\tau^* = \frac{u^*}{(s-1)gd} \tag{3.3}$$

where g is the gravity acceleration, s is the specific weight and d is the grain diameter. The friction velocity of the particle u^* is calculated from

$$u^* = \sqrt{\frac{gn^2U_m^2}{R^{1/3}}} \tag{3.4}$$

Here n is the manning coefficient and n=0.02m$^{-1/3}$·s is used in the present study. U_m is the mean flow velocity in the cross-section, which is calculated at the center of the computation domain after the flow field becomes stable. R is the hydraulic radius, and for simplicity, equal to the still water depth, h.

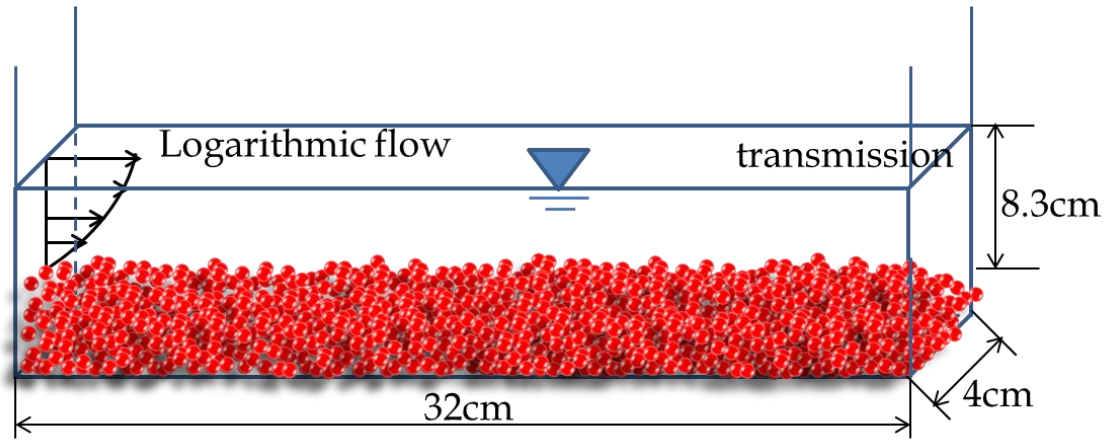

Figure 3.1 Initial set up of uniform size particles in an open channel.

Periodic boundary condition is used for sediment particles, namely particles moving out of

the downstream side in the computation domain are fed back to the upstream side. Lubrication force effects when the distance between particles is less than the cut-off distance Δ_c, to avoid overlap between particles. Since the surface of one single particle is constructed with a series of discrete lattice boundary nodes, the unsmooth boundary surface is not exactly for the spherical particle with the diameter d. A hydrodynamic diameter of 1.05d is obtained by considering the Stokes drag force in low Reynolds number regime. A constant diameter of 1.0d is, however, used throughout the numerical simulations.

Table 3.1 lists a series of cases with different Shields parameter from the simulation result of the mean flow velocity in the cross-section, U_m. Case 8 with Shields parameter of 0.23 is used to verify the model with Gotoh's (1993) experimental data.

Table 3.1 Simulation conditions in cases with different Shields parameter (Okajima, 2013).

case	h(cm)	U_m(cm/s)	u*(cm/s)	τ*
1	8.30	29.5	2.80	0.01
2		46.7	4.43	0.025
3		71.5	6.78	0.06
4		90.1	8.53	0.09
5		93.4	8.85	0.10
6		117.2	11.09	0.16
7		125.3	11.88	0.18
8		141.6	13.43	0.23
9		156.0	14.78	0.28
10		190.2	18.02	0.42

3.3 Simulation Results

The movement of particles is investigated for a series cases with Shields parameter ranged between 0.01 and 0.42 (**Table 3.1**), under a constant water depth of 8.3 cm. **Figure 3.2** shows a snapshot of part of the computation domain of Case 6 at t'=3.0 ($t'=td/\sqrt{(s-1)gd}$) after the flow field is stable.

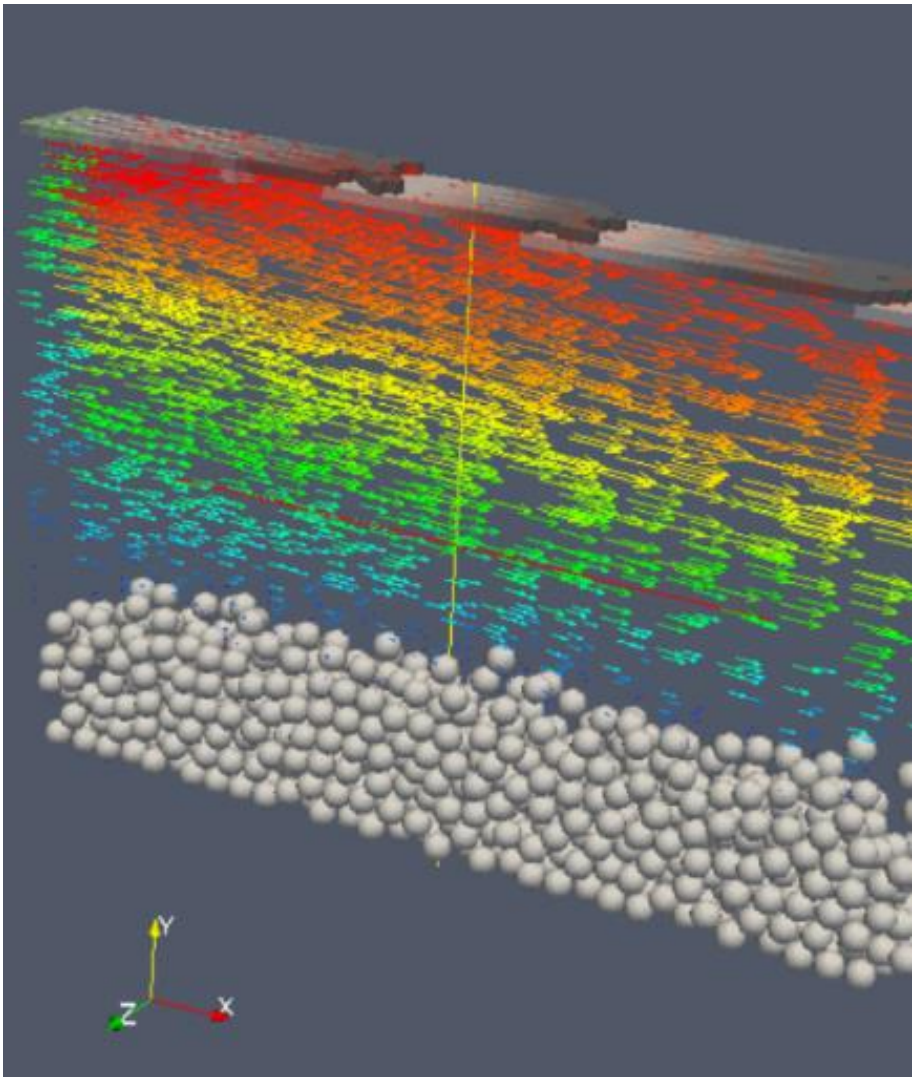

Figure 3.2 Snapshot of uniform grain size sediment in open channel flow (τ^*=0.16).

3.3.1 Flow velocity field of the open channel flow

Figure 3.3 shows the flow velocity fields of Case 6 in different time steps with a same time interval of t'=0.5. The scale bar shows the dimensionless flow velocity, which can be transformed to the dimension value by $\Delta x/\Delta t$ of 0.2cm/1.0×10^{-5}s.

The simulation results in **Fig. 3.3** shows that a tangential flow velocity occurs at the beginning of the simulation, when the dimensionless time is less than 1.5, due to the pressure gradient. However, after t'=2.0, the simulation become stable and the flow velocity fields in the longitudinal section are almost the same, by comparing the results of t'=2.0 and t'=9.0. Similar results can be found in the other cases.

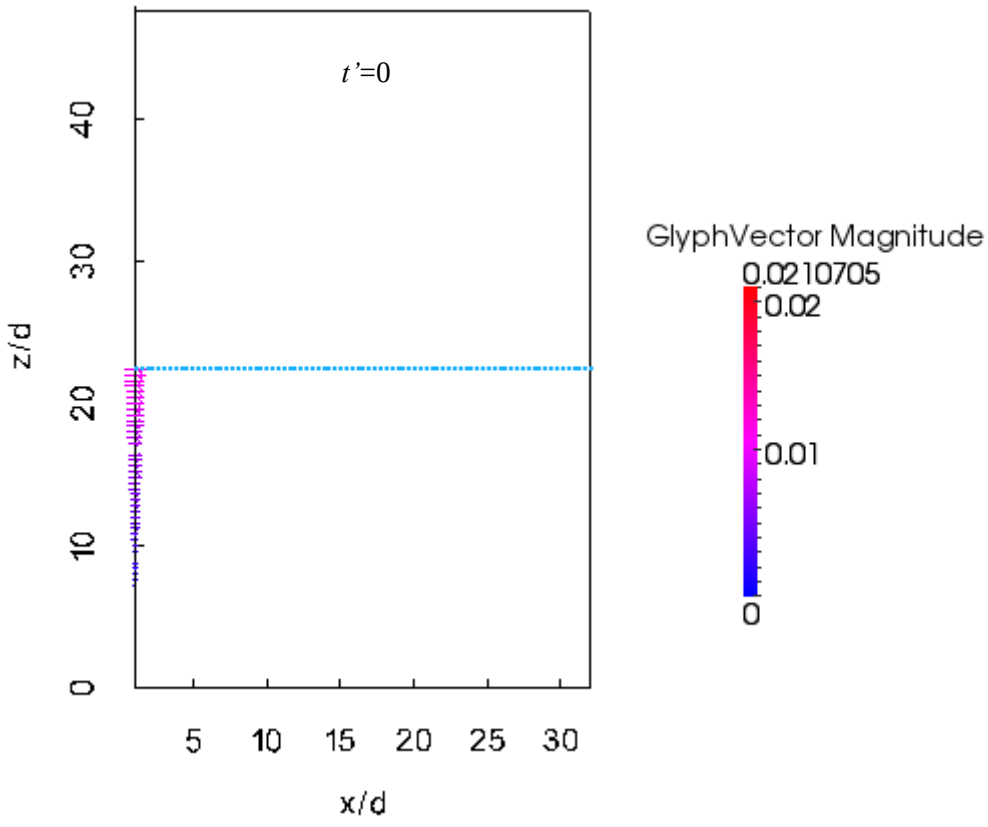

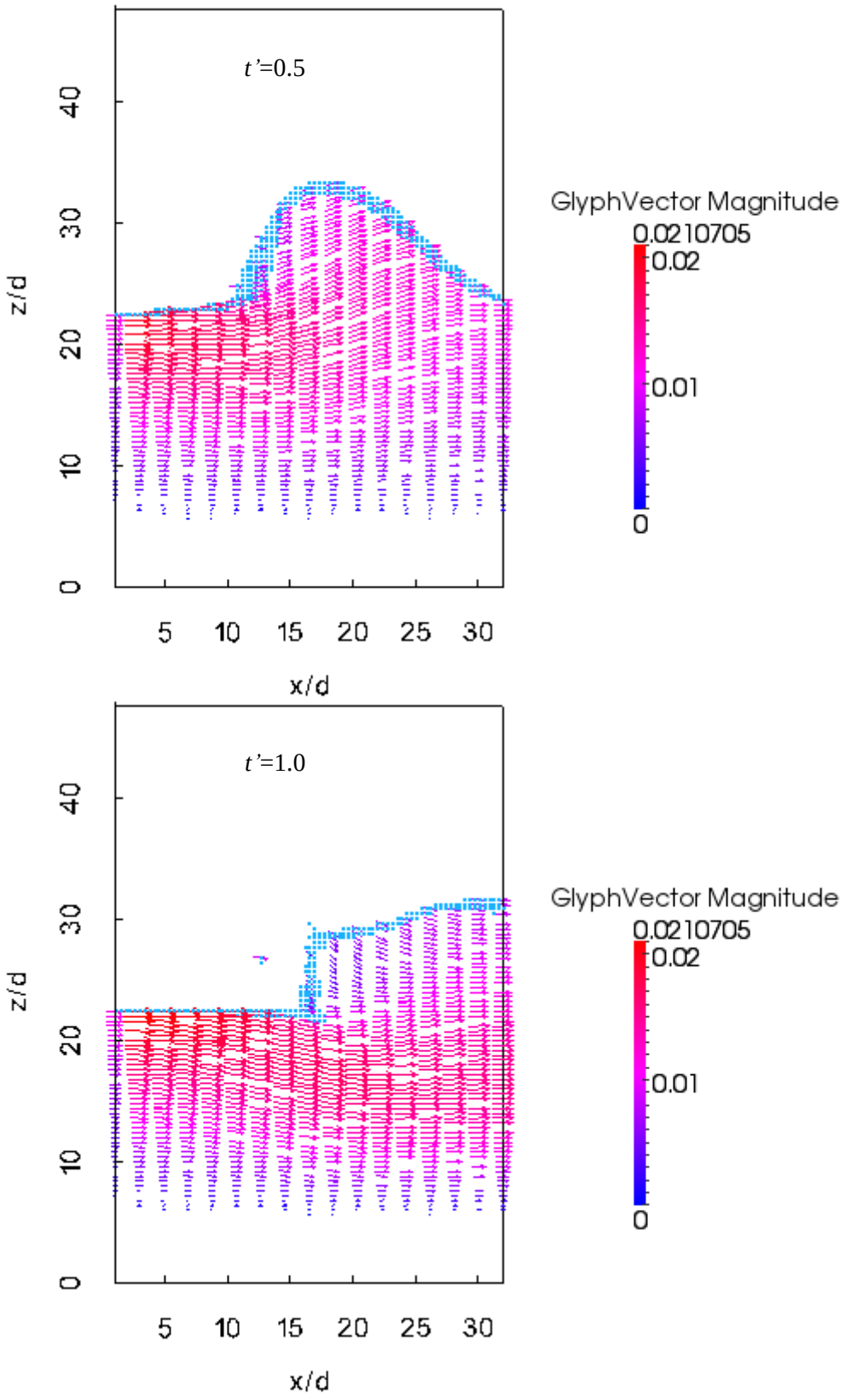
t'=0.5
z/d
0
10
20
30
40
5
10
15
20
25
30
x/d
GlyphVector Magnitude
0.0210705
0.02
0.01
0
t'=1.0
z/d
0
10
20
30
40
5
10
15
20
25
30
x/d
GlyphVector Magnitude
0.0210705
0.02
0.01
0

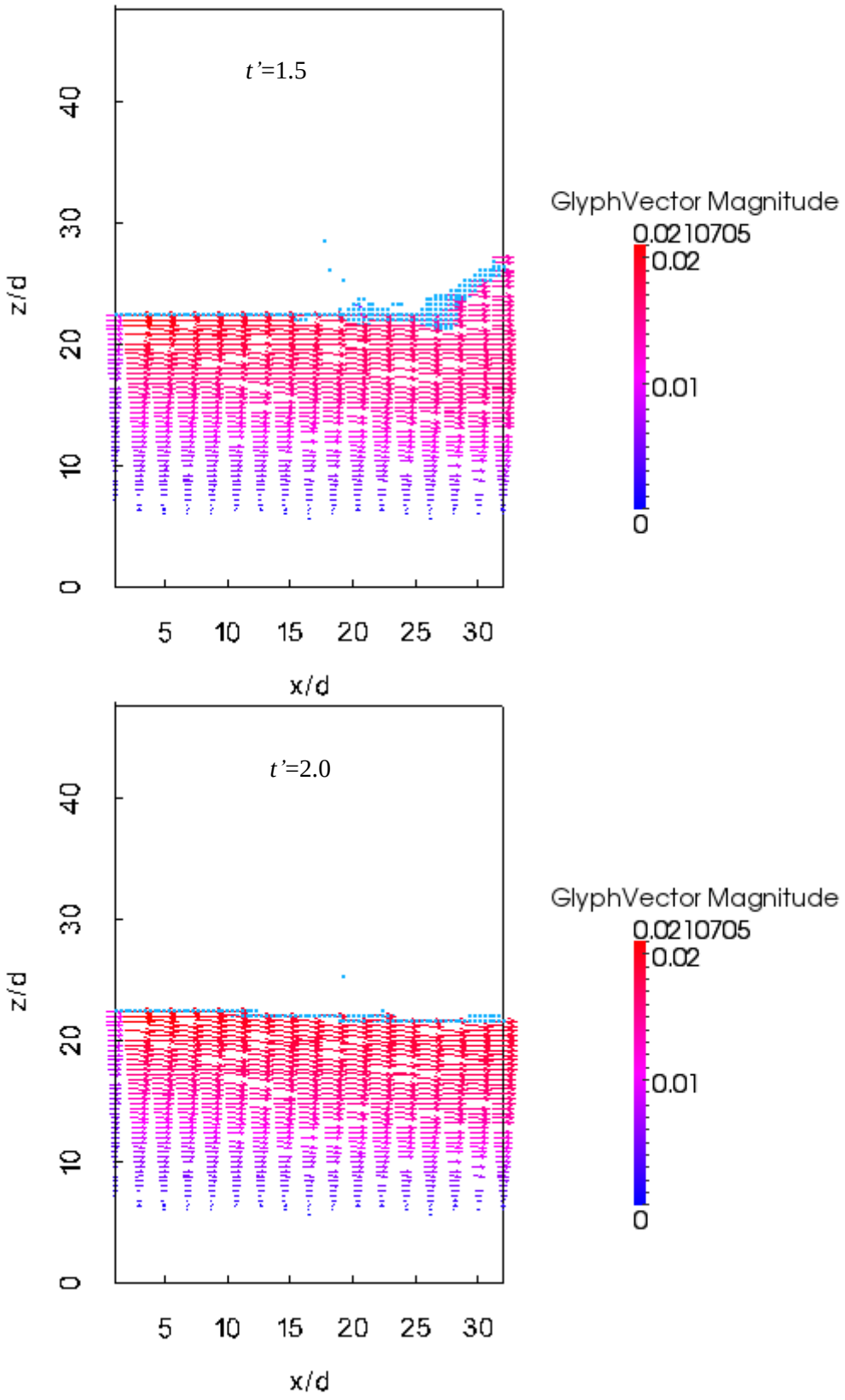
t'=1.5
z/d
0
10
20
30
40
5
10
15
20
25
30
x/d
GlyphVector Magnitude
0.0210705
0.02
0.01
0
t'=2.0
z/d
0
10
20
30
40
5
10
15
20
25
30
x/d
GlyphVector Magnitude
0.0210705
0.02
0.01
0

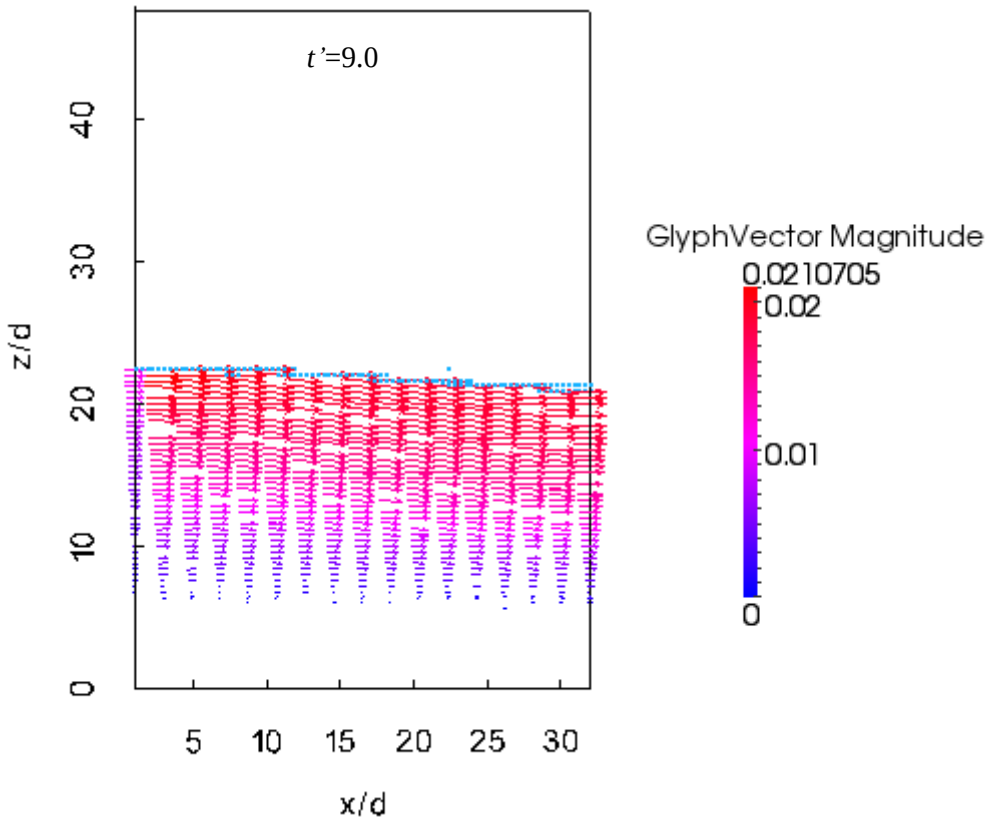

Figure 3.3 Flow velocity fields in longitudinal section (τ^*=0.16).

3.3.2 Movements of sediment particles

Figure 3.4 – **Figure 3.6** show 2D longitudinal profile of the movements of sediment particles at t'=5.5 and t'=12.5. When Shields parameter is small (τ*=0.025), particles move very slowly with sliding and rolling (**Fig. 3.4**). Small saltation happens in the surface layer at t'=12.5 (**Fig. 3.4**). Saltation is detected after t'=9.5 when τ*=0.10 (**Fig. 3.5**) and after t'=6.0 when τ*=0.18 (**Fig. 3.6**) with individual particles departing with significant distances from the bed-load layer. With the increase of Shields parameter, sediment particles move faster as the number of fed back particles increases, and jump higher as the layer thickness z/d increases from 6 (at t'=12.5 in **Fig. 3.4**) to 8 (at t'=12.5 in **Fig. 3.6**). Sheetflow occurs (after t'=9.5 **Fig. 3.5**) when Shields parameter increases to 0.1, and becomes earlier (after t'=8.0 **Fig. 3.6**) and more significant when τ*=0.18.

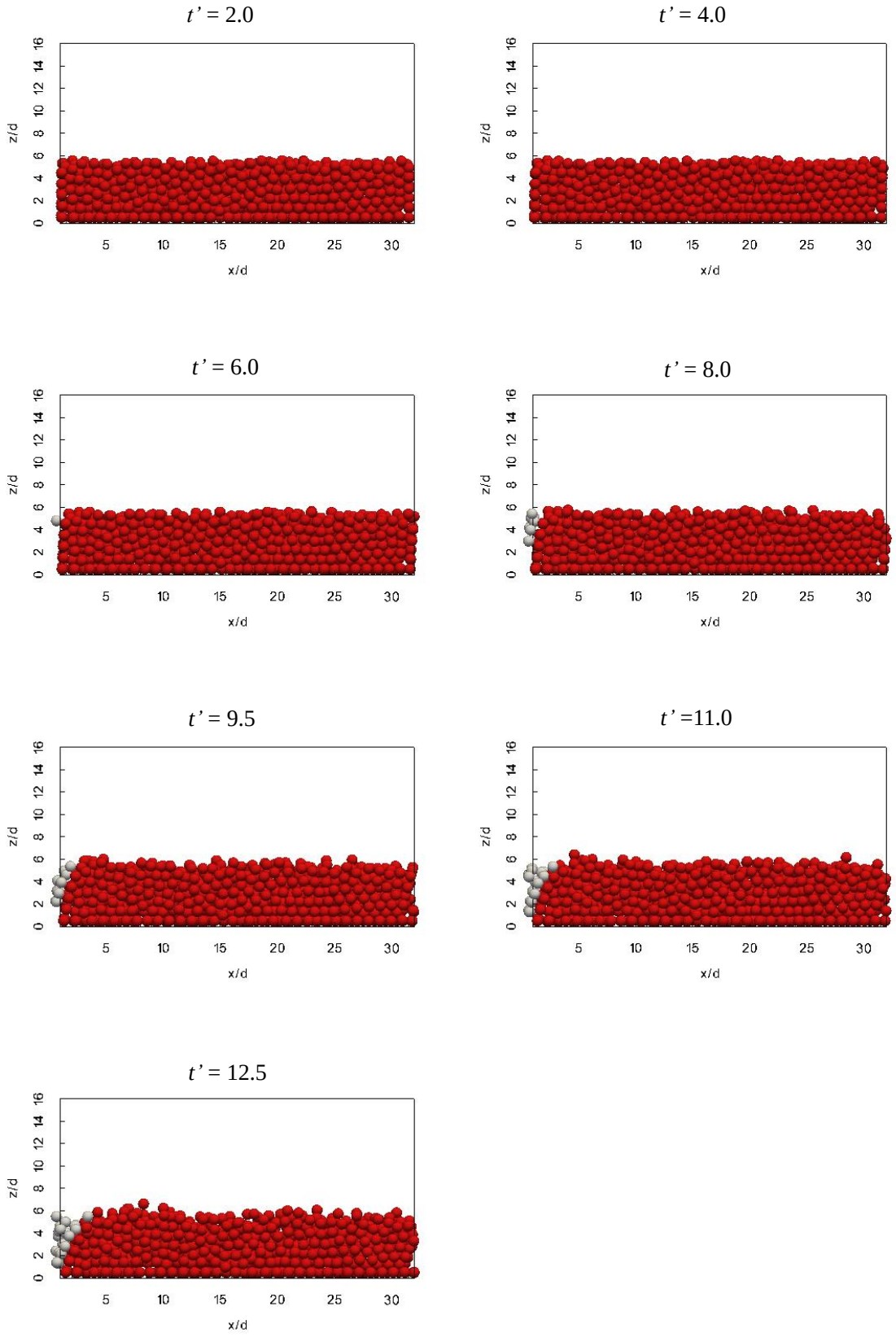

Figure 3.4 2D longitudinal profile of the movements of sediment particles (τ^*=0.025).

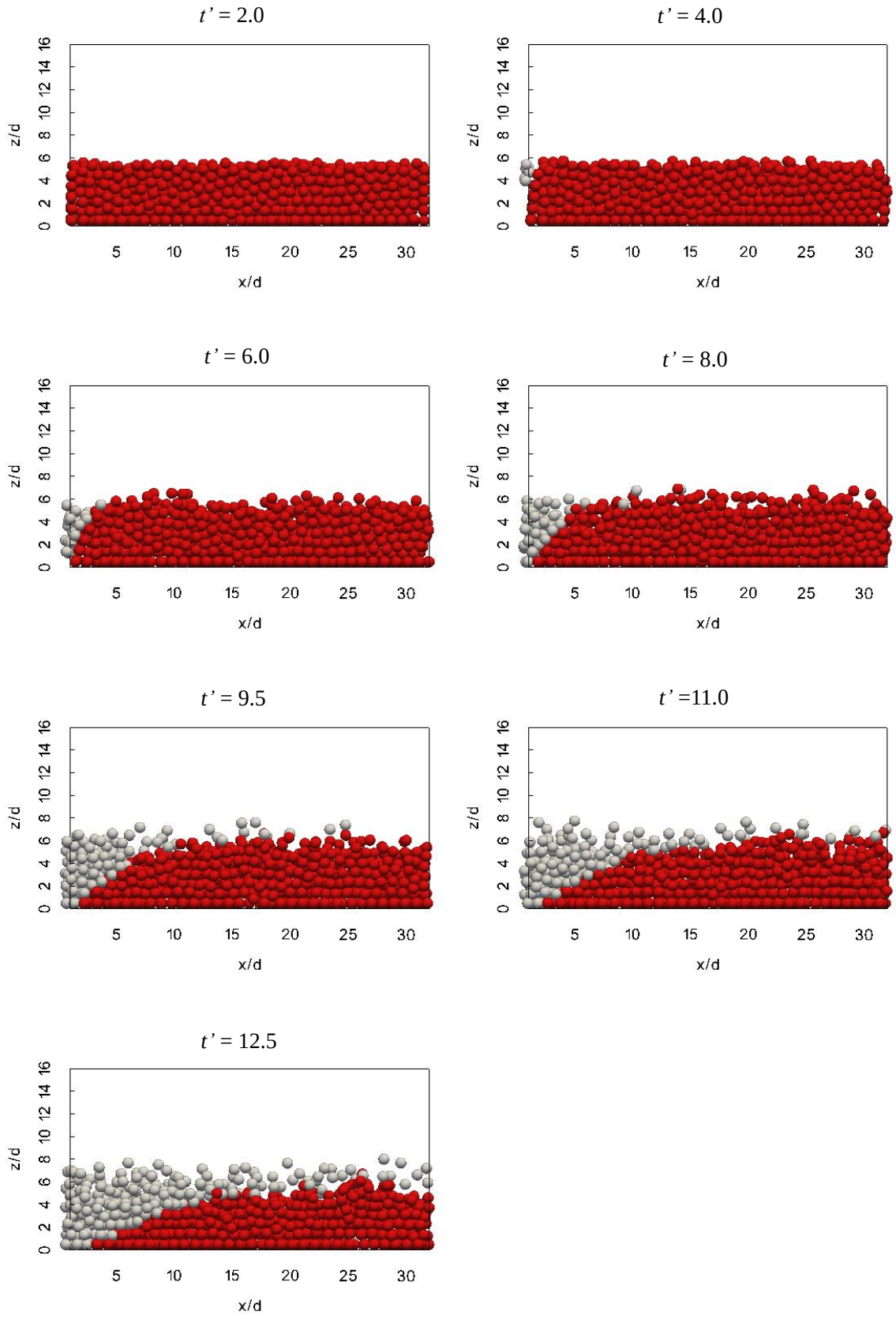

Figure 3.5 2D longitudinal profile of the movements of sediment particles (τ^*=0.10).

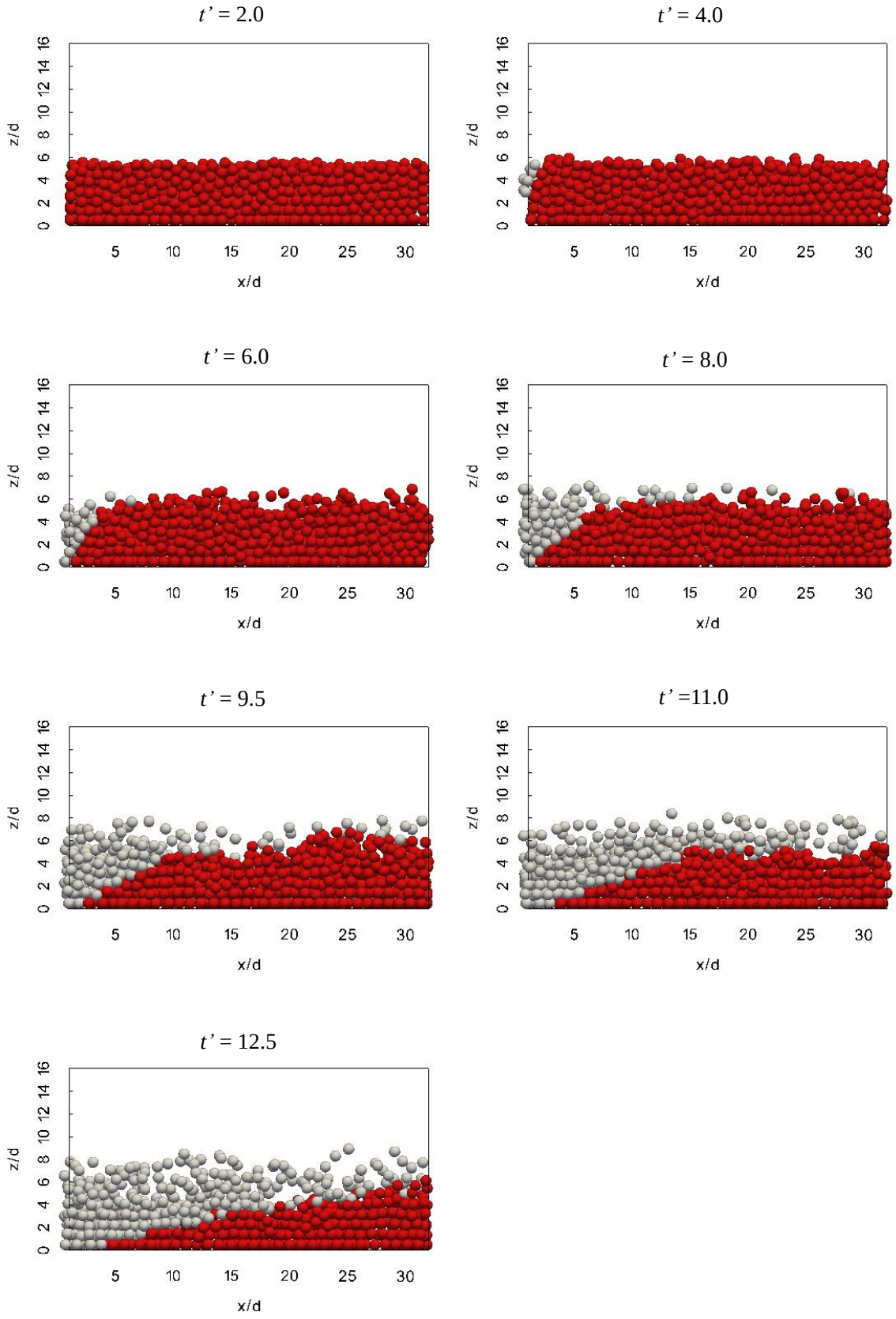

Figure 3.6 2D longitudinal profile of the movements of sediment particles (τ^*=0.18).

Figure 3.7 – **Figure 3.9** show the paths of 5 individual particles (Particle 1 - Particle 5) extracted from bottom to top with the same interval time of t'=0.5.

In the case of Shields parameter τ^*=0.025 (**Fig. 3.7**), particles at the bottom layer (Particle 1) hardly move, and particles in the intermediate layer (Particle 2 and Particle 3) move with sliding and rolling. These particles move with a 3D spiral trajectory, i.e., Particle 3 has a significant displacement in the transverse direction (**Fig. 3.7c**), due to the effect of repeated collisions. Particles in the surface layer (Particle 4 and Particle 5) move with a small saltation besides sliding and rolling (**Fig. 3.7b**).

With the increase of Shield parameter, the movement of particles in the intermediate layer becomes significant in the vertical direction (**Fig. 3.8b**). In the case of Shields parameter τ^*=0.1, particles (Particle 2 and Particle 3) show a trajectory of zigzag (**Fig. 3.8a, c**)due to the repeated collisions between particles in the surface layer and bottom layer, and the momentum is transferred between these two layers.

As shown in **Fig. 3.9**, when τ^*=0.18, sheetflow occurs in the bed-load layer, and saltation particles are observed in the surface layer. With the increase of Shields parameter, the movement of particles in the bed-load layer becomes 2D sheetflow, and the particle trajectories can be drawn in the 2D plane as the saltation distance becomes longer (**Fig. 3.9 a, b**).

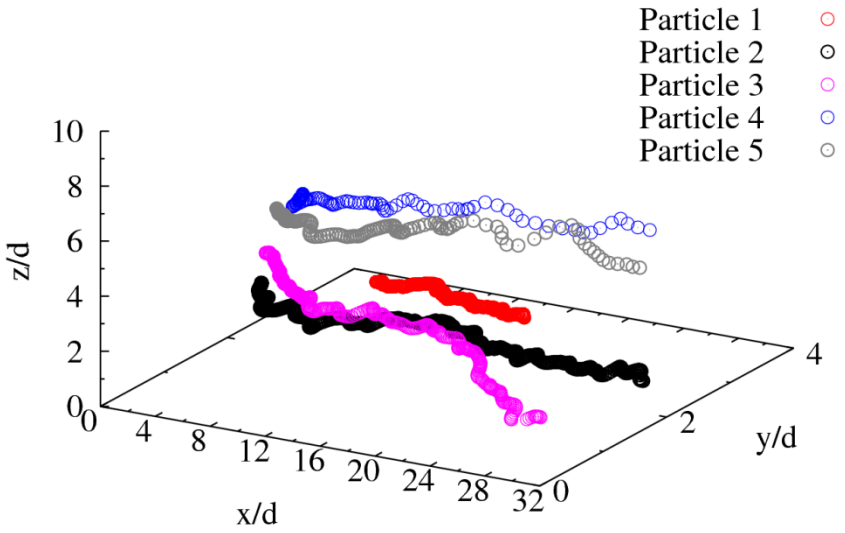

(a) 3D view

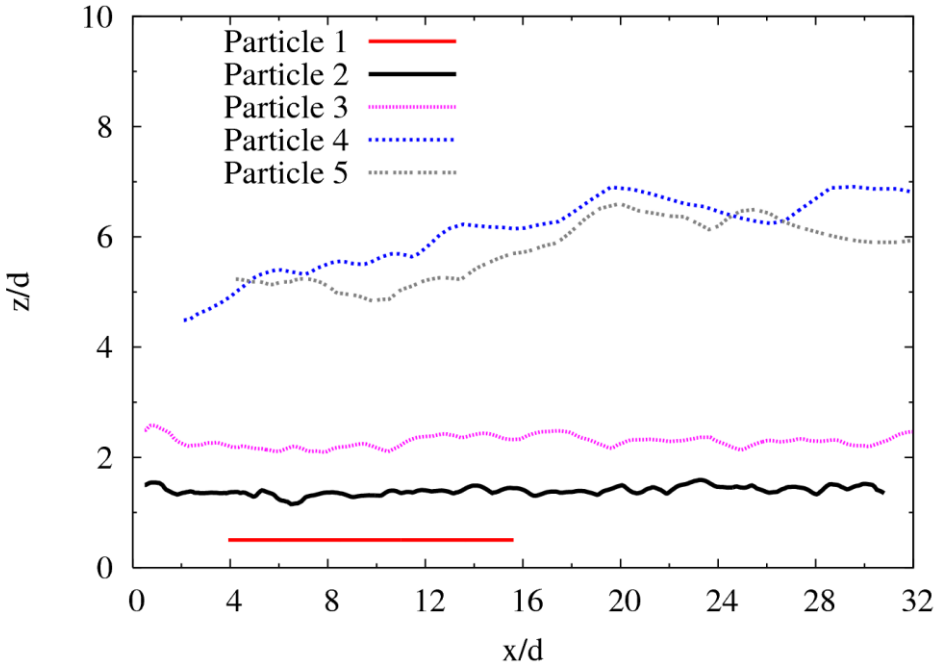

(b) 2D view in x-z plane

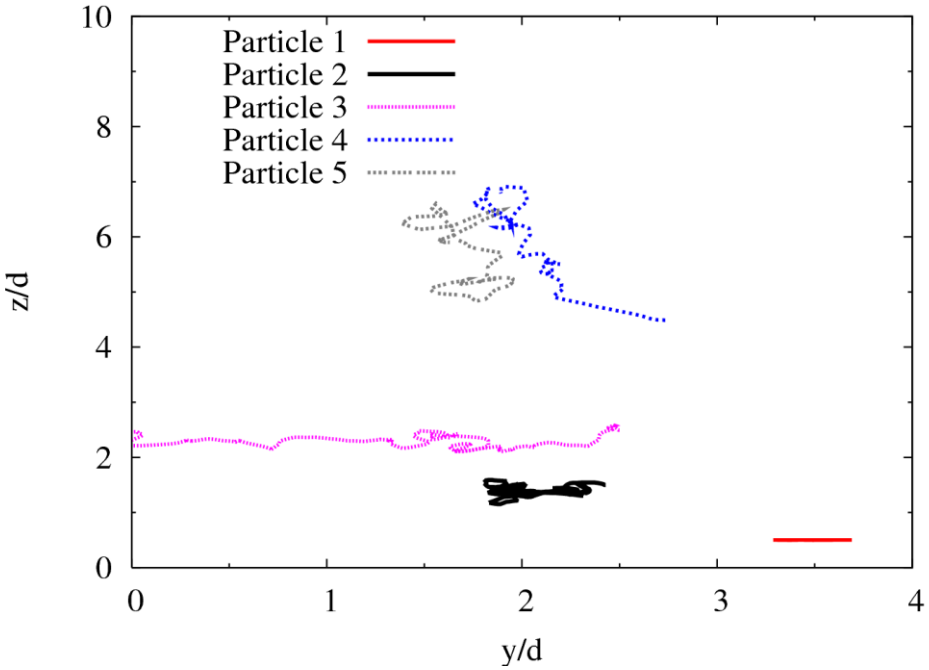

(c) 2D view in y-z plane

Figure 3.7 Trajectories of individual sediment particles (τ^*=0.025).

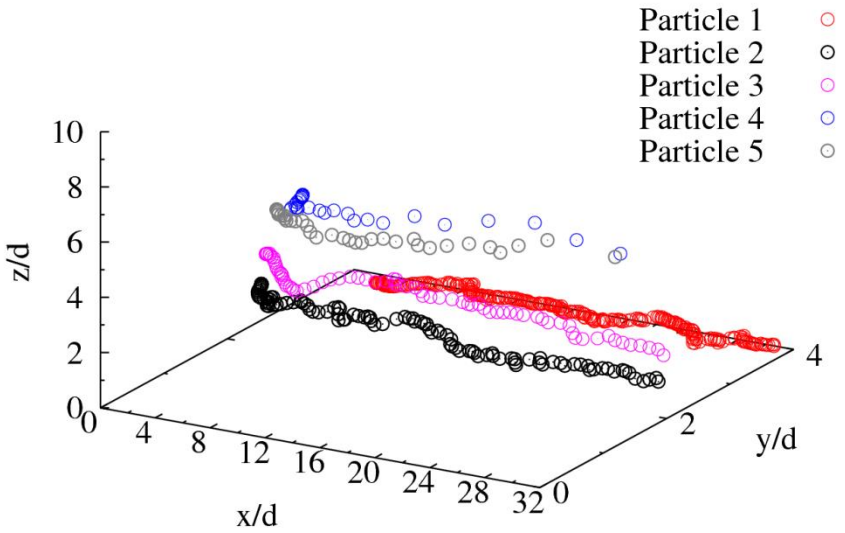

(a) 3D view

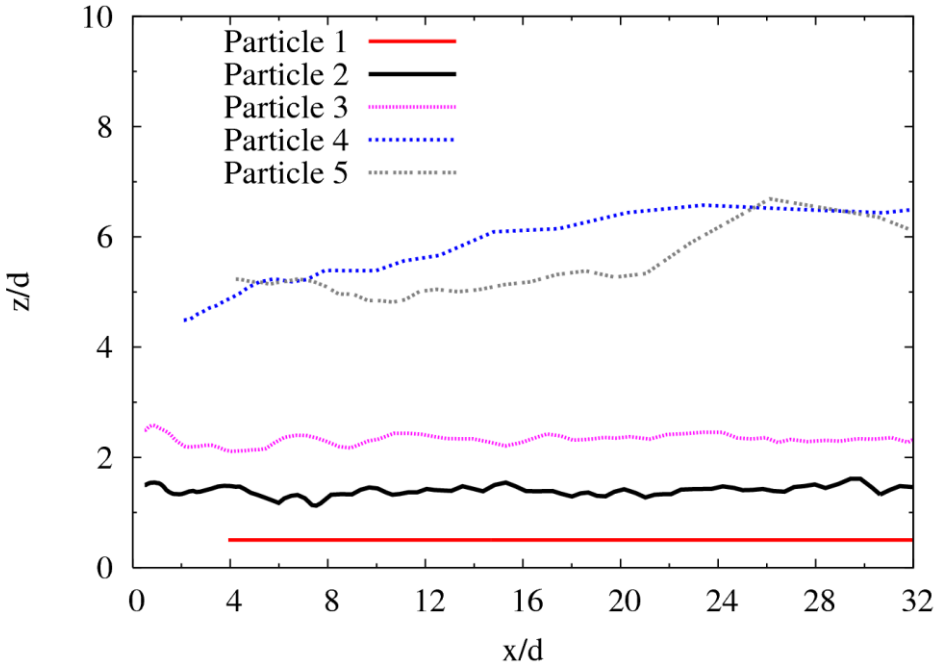

(b) 2D view in x-z plane

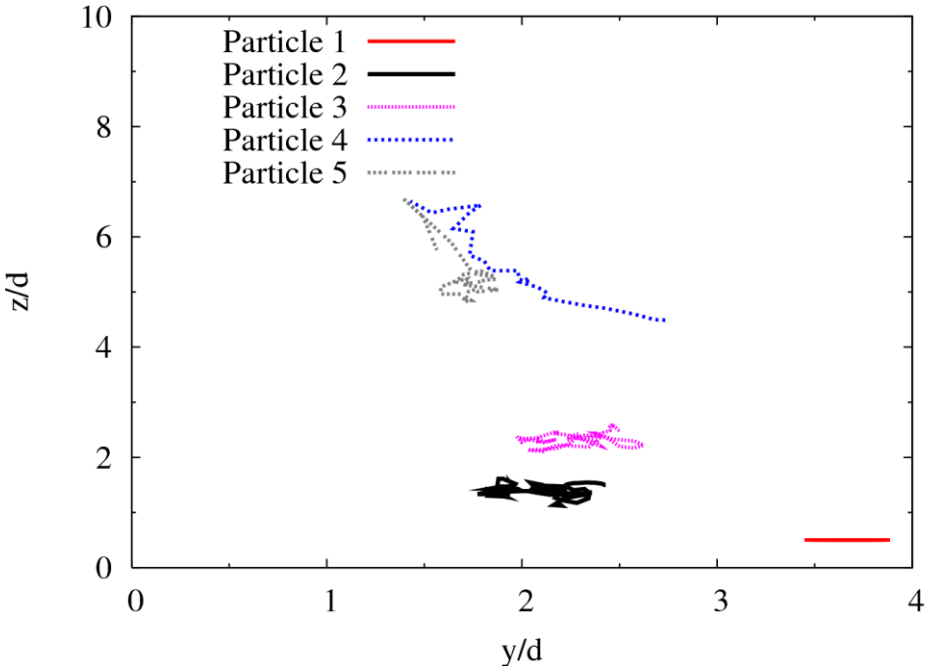

(c) 2D view in y-z plane

Figure 3.8 Trajectories of individual sediment particles (τ^*=0.10).

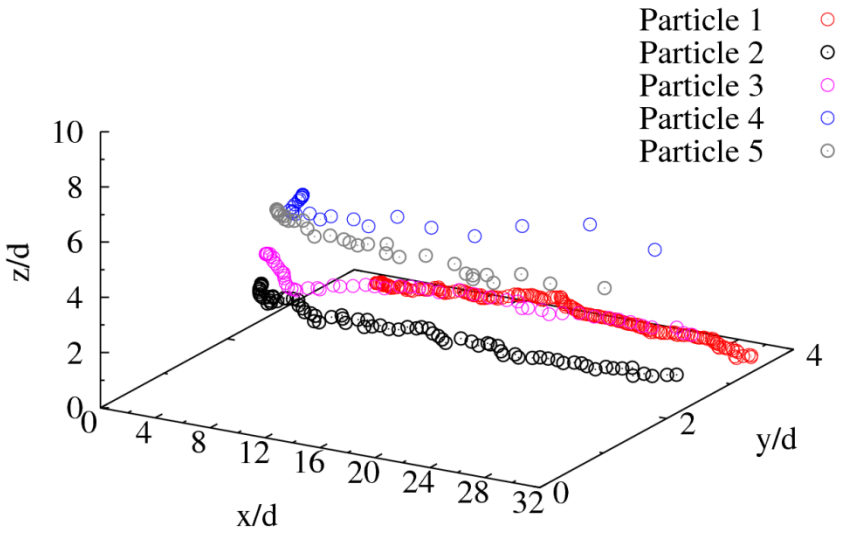

(a) 3D view

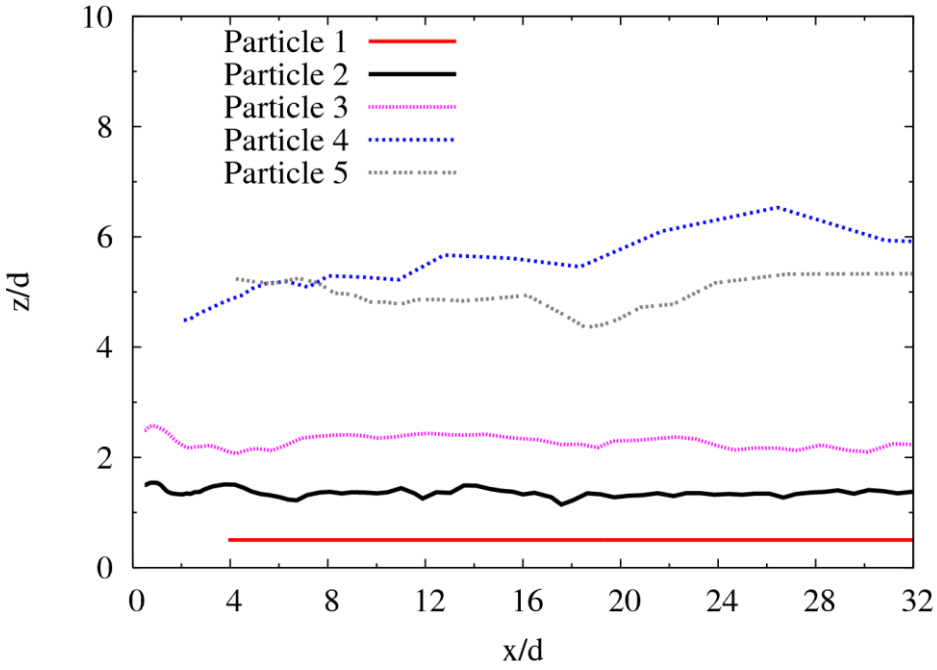

(b) 2D view in x-z plane

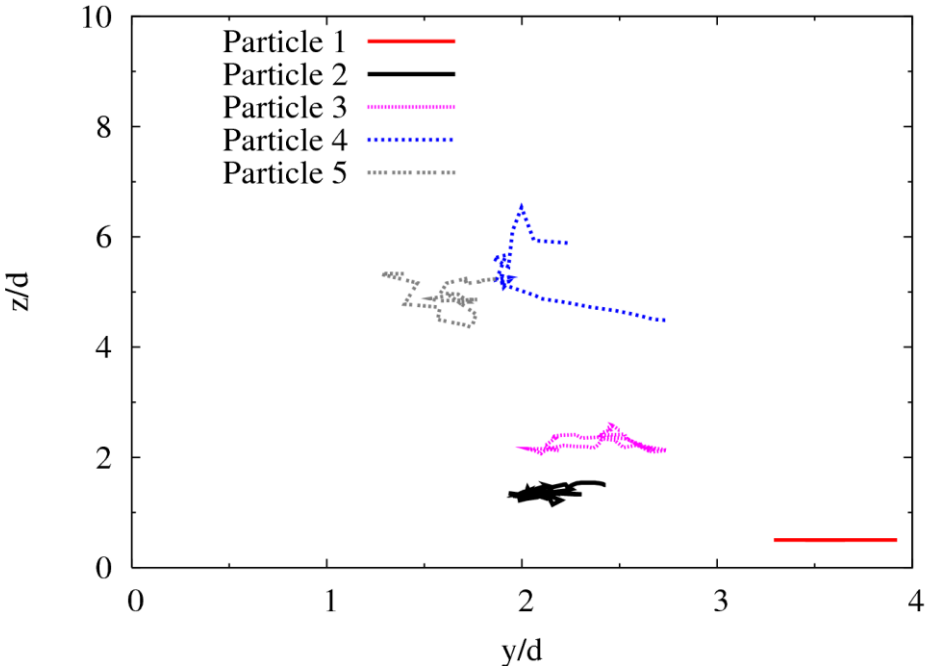

(c) 2D view in y-z plane

Figure 3.9 Trajectories of individual sediment particles (τ^*=0.18).

3.3.3 Horizontal velocity of sediment particles

Figure 3.10 shows the horizontal velocity distribution of particles corresponding to the change of τ^*, and the experimental results of Gotoh et al. (1994). Except the case of τ^*=0.06, the horizontal velocity of particles in the bed-load layer does not increase monotonously. There exist several inflection points in the surface layer. This phenomenon is quite similar to the results of Gotoh et al. (1994), where larger arc-shaped saltation occurs due to the repeated collisions between particles in the intermediate layer. The simulation result of the velocity distribution agrees fairly well the result of Gotoh's experiment for τ^*=0.23.

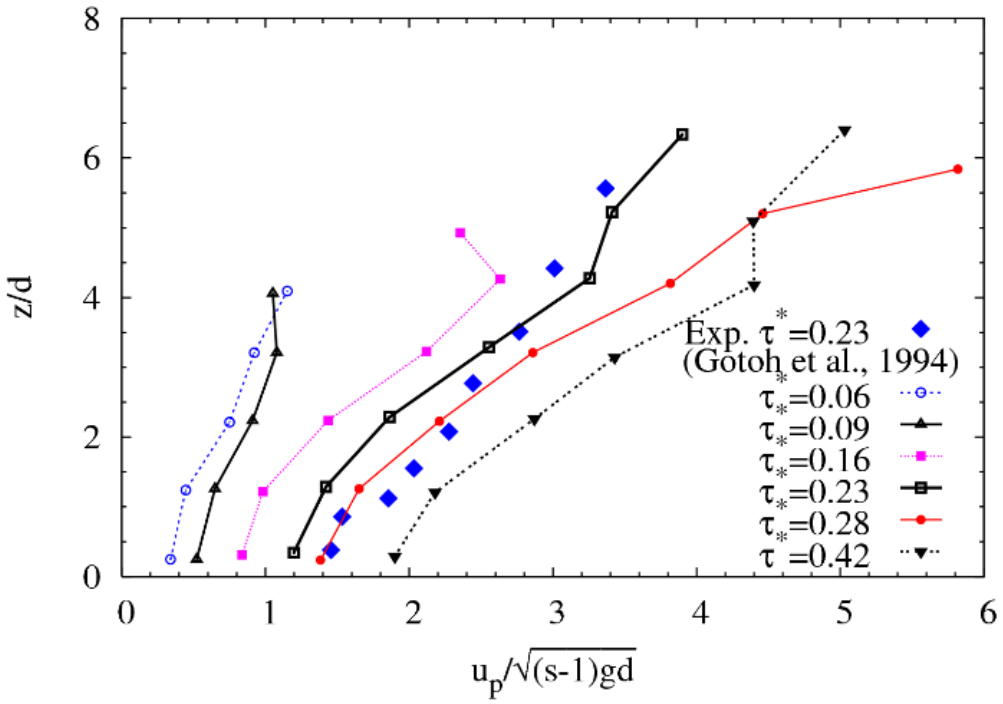

Figure 3.10 The horizontal movement velocity of sediment particles.

3.3.4 Vertical P.D.F of sediment particles

The vertical existing probability density function (P.D.F) is evaluated by counting the moving particle number of each layer with uniform thickness, d and then divided by the total moving particle number of overall layers. **Figure 3.11** shows the vertical existing P.D.F of bed-load layer with variable Shields parameter. The width of the peak is slightly wider with the increase of Shields parameter. The distribution of vertical existing P.D.F of moving sediment particles is asymmetry with a steep rise from bottom to peak and a gentle decrease toward the surface. The position of the peak of vertical existing P.D.F tends to decrease with the increase of τ^*, however, it is fixed when $\tau^*>0.2$. In comparison with the experimental value of Gotoh et al. (1993), the simulated peak value is slightly larger and the position of peak is also a little higher, however, the centroid center of vertical existing P.D.F agrees quite well with the experimental results when $\tau^*=0.23$.

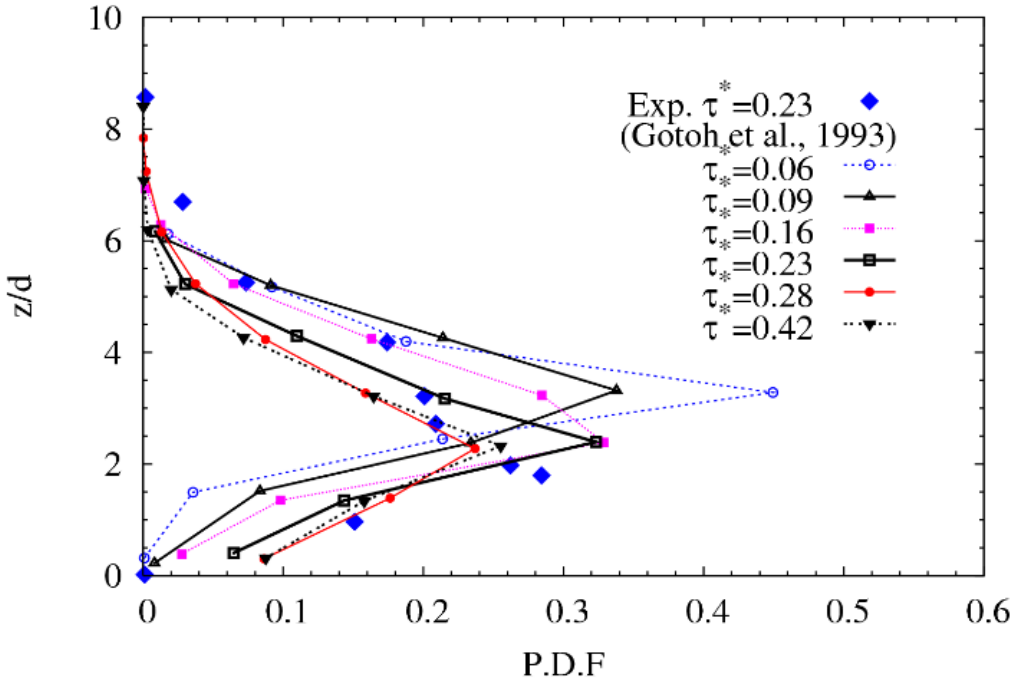

Figure 3.11 The vertical existing probability density distribution of sediment particles.

3.4 Conclusions

The 3D movable bed model based on LBM is developed to study the particle movements of uniform grain size sediments of bed-load layer under open channel flow in sheetflow regime. In the present LBM model, any semi-empirical coefficient is not needed as an input data, but only the cut-off of lubrication approximation, the additional offset in computing fluid fraction, together with the Smagorinsky Constant in turbulent model are required. This model can be extended relatively easily to 3D movable bed in large scale, because the LBM process involves an algorithm suitable for parallel computation.

For the model's validation, the horizontal velocity distribution of sediment particles and the vertical exists probability distribution function (P.D.F) of sediment particles of the Case 8 with τ^*=0.23 are compared with the experimental data of Gotoh et al. (1994) and Gotoh et al. (1993), respectively. The results show that the tendency of horizontal velocity distribution agrees well with the experimental data. In comparison with the experimental value of Gotoh et al. (1993), the simulated peak value is slightly larger and the position of peak is higher, however, the centroid of vertical existing P.D.F agrees quite well with the experimental results.

In order to know more about the behavior of uniform bed-load sediments, a series of cases are carried out with different Shields parameter ranged between 0.01 and 0.42, under a constant water depth of 8.3 cm. The time series of flow velocity field in the longitudinal section show that at the beginning, the flow velocity is unstable with a tangential flow velocity due to pressure gradient and after the dimensionless time step of t' = 2.0, the flow velocity field becomes stable.

2D longitudinal profiles of the movements of sediment particles are analyzed. The results show that when Shields parameter is small, particles move very slowly with sliding and rolling, and small saltation occurs in the surface layer. With the increase of Shields parameter, sediment particles move faster and jump higher, and saltation becomes

significant. Sheetflow occurs when Shields parameter increases to 0.1, and becomes more significantly pronounced when τ*=0.18.

The trajectories of 5 individual particles show that sediment particles at the top of bed-load layer move with a small saltation besides sliding and rolling, sediment particles in the middle layer move with sliding and rolling, and sediment particles move with a 3D spiral trajectory due to the collisions among particles when the Shields parameter is small (τ^*=0.025). With the increasing of τ^*, particles in the intermediate layer becomes more motive in the vertical direction. When τ^*=0.18, sheetflow occurs in the bed-load layer, and saltation particles are observed in the surface layer. With the increasing of τ^*, the movement of particles in the bed-load layer becomes 2D sheetflow, and the trajectories of particles can be drawn in a 2D plane as the saltation distance becomes longer.

The horizontal velocity distribution of sediment particles show that the horizontal velocity of the top bed-load layer does not increase monotonously, but increase in a complicated distribution with several inflection points in all cases except the case of τ*=0.06, where sediment particles hardly move. This phenomenon is quite similar to the results of Gotoh (1993), where larger arc-shaped saltation occurs due to the repeated collisions between particles in the intermediate layer.

The vertical existing probability density function (P.D.F) is evaluated by counting the moving particle number of each layer with uniform thickness, d and then divided by the total moving particle number of overall layers. The results show that the distribution of vertical existing P.D.F of sediment particles is asymmetry and the width of the peak of particles' P.D.F increase with the increase of Shield parameter. The position of the peak of particles' P.D.F becomes lower with the increase of Shield parameter but it is almost fixed when τ^*>0.2.

CHAPTER 4

THE BEHAVIOR OF MIXED GRAIN SIZE SEDIMENTS UNDER BOTH OSCILLATORY FLOWS AND PROGRESSIVE WAVE

4.1 Introductions

The vertical sorting process of graded sediment is for the further study of sediment transport rate of mixed grain size sediments. Studies on graded sediments under unidirectional flows were carried out originally, and these studies showed that the armoring parameter is a vital parameter for specifying the armoring effect. Later, studies on graded sediments under symmetric oscillatory flows are investigated. Then, studies on graded sediments under asymmetric oscillatory flows, i.e., oscillatory flows based on first approximation of cnoidal wave (Dibajnia and Watanabe, 2000; Ahmed and Sato, 2003b), oscillatory flows based on second-order Stokes wave (Hassan and Ribberink, 2005) are performed.

In this chapter, the present model is applied to simulate the sediment particle behaviors of mixed grain size sediments under both symmetric sinusoidal oscillatory flows and asymmetric oscillatory flows generated by the cnoidal wave with second approximation. In order to compare with both the experimental results and numerical simulation results of Harada and Gotoh (2008), particles with relatively large diameters of the order of 1cm are applied. For studying the influence factor to the vertical grading of mixed grain size sediments, cases with different Shields parameters, oscillatory flow periods, bottom layer thicknesses and slope of bottom are conducted under symmetric sinusoidal oscillatory flows.

For the analysis of the simulation results, computational snapshots are detected to get a

direct view of the vertical grading of mixed grain size sediments. The centroids of concentration of large, middle and small particles in the whole computation domain are drawn respectively, to confirm the vertical sorting of mixed grain size sediments. The mean velocity of sediment particles with different sizes are used to study the sediment particle motion in fluid. Dimensionless particle number density is calculated as a base of predicting sediment transport rate of mixed grain size sediments.

A single case of mixed grain size sediment under progressive cnoidal wave is performed. The time series of water elevation together with flow velocity fields generated by the initial cnoidal wave are described. Vertical sorting of mixed grain size sediments are analyzed, including the detection on computation snapshots and concentration centroids of seaward, center and landward areas.

4.2 Numerical Conditions

Three types of grains with diameters of 0.5cm, 1.0cm and 1.5cm, respectively, are performed under oscillatory flows and cnoidal wave. Periodic boundary conditions are used for the left and right side of the computation domain and no-slip boundary conditions for the others.

Table 4.1 lists six cases under symmetric sinusoidal oscillatory flows and asymmetric oscillatory flow based on cnoidal wave theory with second order. The Shield parameter Ψ is calculated with the maximum flow velocity of the oscillatory flow. **Table 4.2** shows the component of sediment mixture in **Table 4.1**.

Table 4.1 Characteristics of cases under oscillatory flow (Case 1 – Case 5) and progressive conidal wave (Case 6)

	Number of particles	Specific gravity, s	Flow / wave period, T	Shields prameter, Ψ	Bottom Layer thickness, δ	Slop bottom
Case 1	A	2.65	1.0s	0.58	4cm	0
Case 2	A	2.65	1.0s	**0.36**	4cm	0
Case 3	A	2.65	**2.0s**	0.58	4cm	0
Case 4	A	2.65	1.0s	0.58	4cm	**1/10**
Case 5	B	2.65	1.0s	0.58	**8cm**	0
Case 6	C	1.10	1.4s	0.31	4cm	0

Table 4.2 Composition of mixed grain size sediment.

Sediment mixture	Sediment particle numbers			
	Total	d_1	d_2	d_3
A	3,740	88	399	3,253
B	7,400	225	895	6,280
C	48,620	1,244	5,188	42,188

Case 1 is set as a basic case for the comparison. In order to get a clear idea of the vertical sorting process of mixed sand, particles with large diameters, which is 10 times larger than usually used in experiments but the same to Harada and Gotoh's (2008), are used in the simulation. Oscillatory flows with relatively large maximum velocities and short periods T of 1s and 2s, which also have been applied by Harada et al (2010) and Gotoh et al. (2002) ,

respectively, are applied in the present simulation to save computation time. With a frictional coefficient of 0.018, Shield parameter of 0.36 and 0.58 can be obtained by the corresponding flow-velocity amplitude of 220cm/s and 280cm/s. The initial positions of particles shown in **Fig. 4.1** are obtained from the settling down of particles, which are suspended randomly without contact to the adjacent particles in the cubic computation domain at the beginning.

The second approximation of cnoidal wave theory is applied to generate a cnoidal wave with a still water depth of 20cm, wave height of 14cm and period of 1.4s. Sand mixture C (**Table 4.2**) with the same thickness δ=4cm, but s=1.32 are set in the numerical flume to get a view of the behavior of mixed sands.

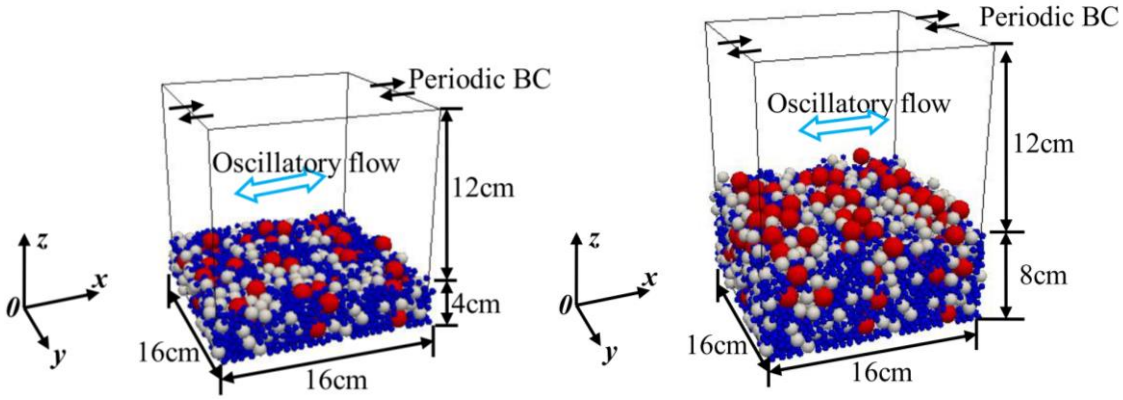

(a) (b)

Figure 4.1 Initial snapshots of (a) Case1, Case 2, Case 3, Case 4 and (b) Case 5.

4.3 Simulation Results of Mixed Sands under Symmetric Oscillatory Flows

Figure 4.2 to **Figure 4.6** show the computational snapshots of Case 1 to Case 5 on different phases in both developing stage of grading and developed stage of grading. Centroids of concentration of particles in Case 1 to Case 5 are shown in **Fig. 4.7** and **Fig.4.8**. **Figure 4.9** to **Figure 4.13** show the mean velocity profiles of individual small, middle and large sediment particles of Case 1 to Case 5, respectively. **Figure 4.14** to **Figure 4.18** show the dimensionless particle number density distributions of Case 1 to Case 5 respectively.

4.3.1 Vertical sorting process

The simulation results of Case 2 (**Fig. 4.3b**) and Case 1 (**Fig. 4.2b**) indicate that the phenomenon of vertical sorting is more significant with larger Shield number.

In Case 3, where the period of oscillatory flow increases to double of Case 1, vertical sorting starts earlier. However, after 1.5T, armor effect is not sufficiently working and middle particles become near suspension (**Fig. 4.4d**). The flow velocity U_m and Shields parameter for Case 3 and Case 1 are the same, while T increases to double, the angular velocity ω becomes half. Hence the water particle semi-excursion A (in the function $U_m=A\omega$) increases, which induces that the Keulegan-Carpenter number increase with the increase of drag force (Nielsen, 2009). Namely, more momentum can be transferred from the fluid, sediment particles become more motive and as a result, the armoring effect breaks.

When a sloping bottom of 1/10 is used for the simulation, the movement of small particles and middle particle are quite similar, however, large particles move much faster in the down-hill flow (**Fig. 4.5a**).

Armoring takes effect earlier in Case 5, where the thickness δ of sediments increases to double (**Fig. 4.6b**) of Case 1. Large particles move to the top layer with middle particles below it and a mixture of small, middle and large particles (**Fig. 4.6d**). However, as simulation goes on, large particles get more momentum from the fluid, and some of them become suspended (**Fig. 4.6f**).

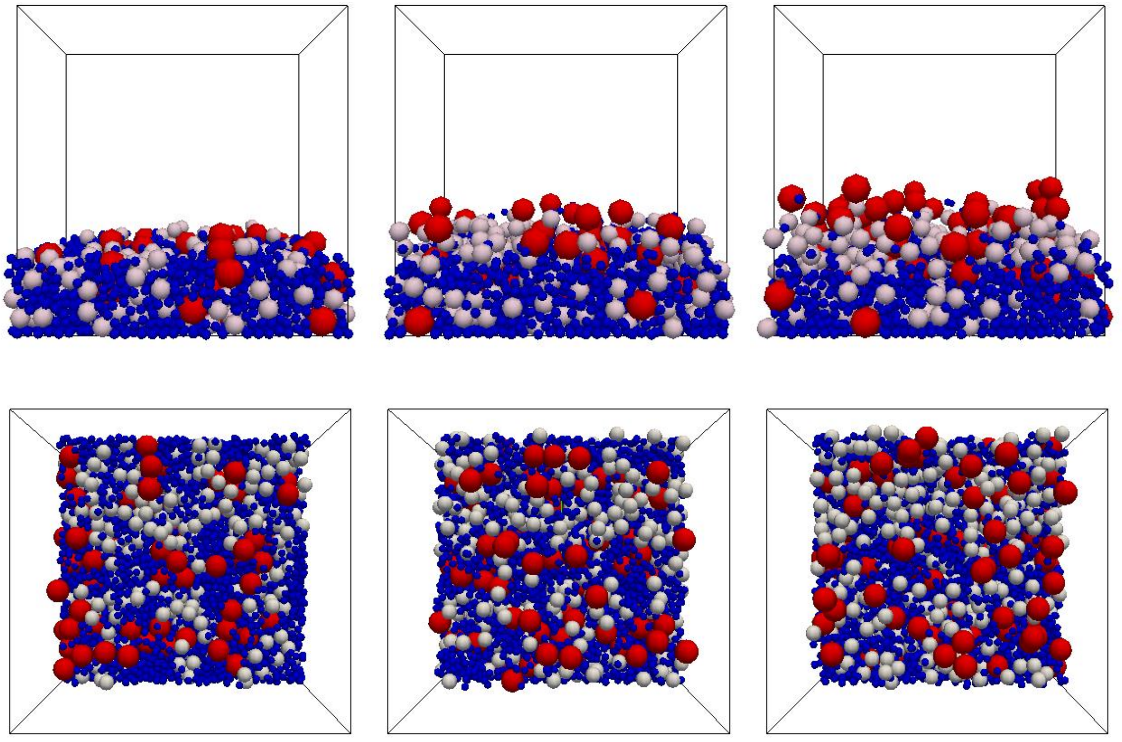

(a) Φ=(1/4)π (b) Φ=(1/2)π (c) Φ=(3/4)π

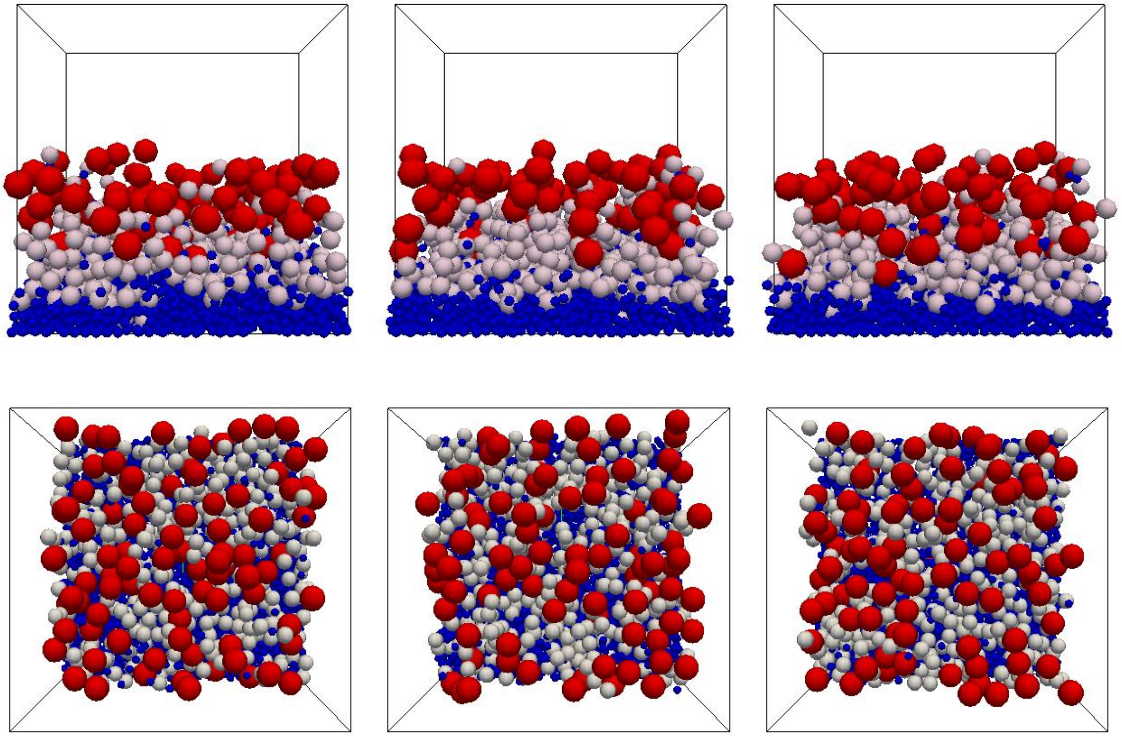

(d) Φ=(1/4)π (e) Φ=(1/2)π (f) Φ=(3/4)π

Figure 4.2 Snapshots of side/top view of Case1 in the developing stage of grading (a, b, c) and developed stage of grading (d, e, f).

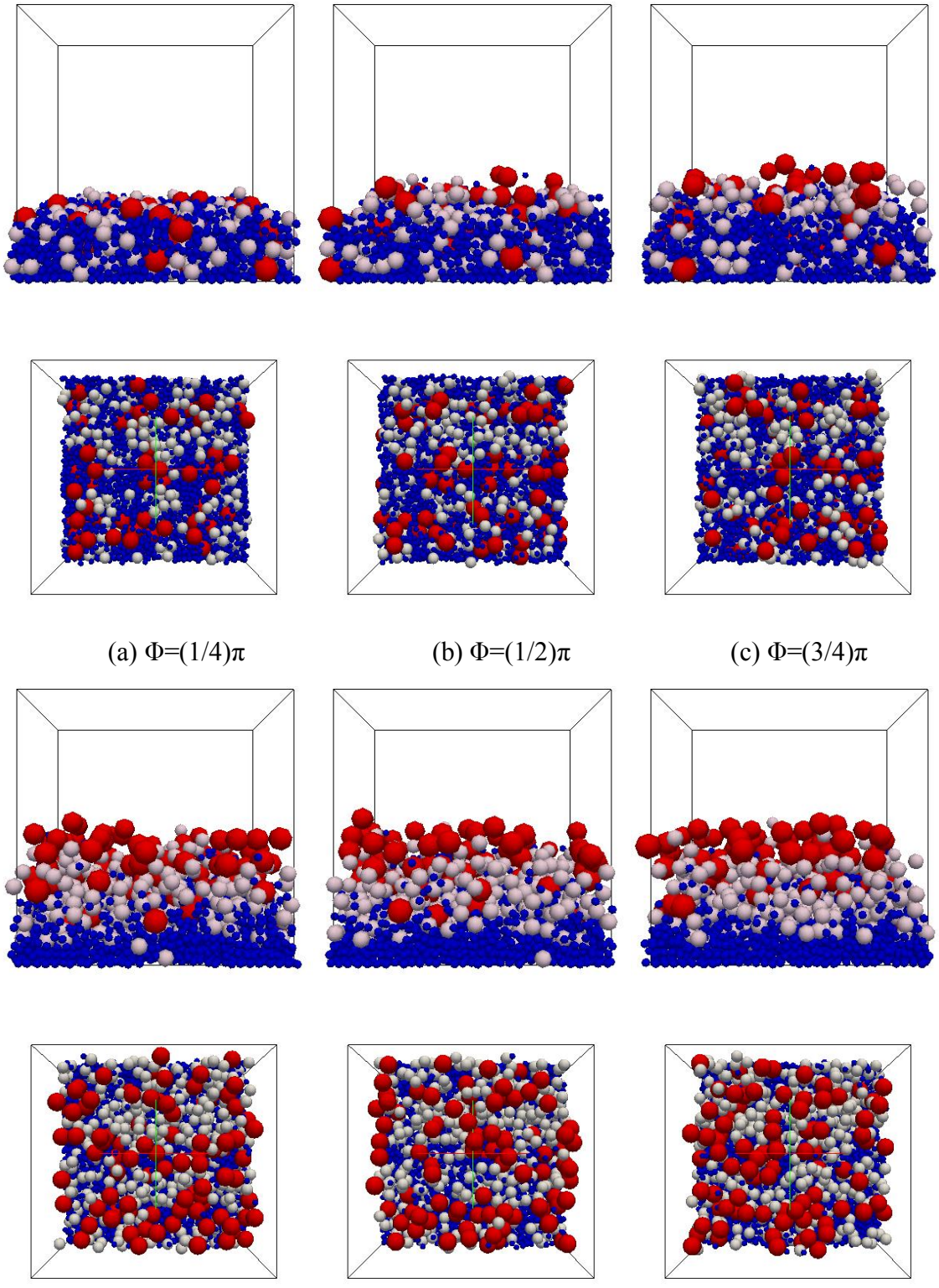

(a) Φ=(1/4)π (b) Φ=(1/2)π (c) Φ=(3/4)π

(d) Φ=(1/4)π (e) Φ=(1/2)π (f) Φ=(3/4)π

Figure 4.3 Snapshots of side/top view of Case 2 in the developing stage of grading (a, b, c) and developed stage of grading (d, e, f).

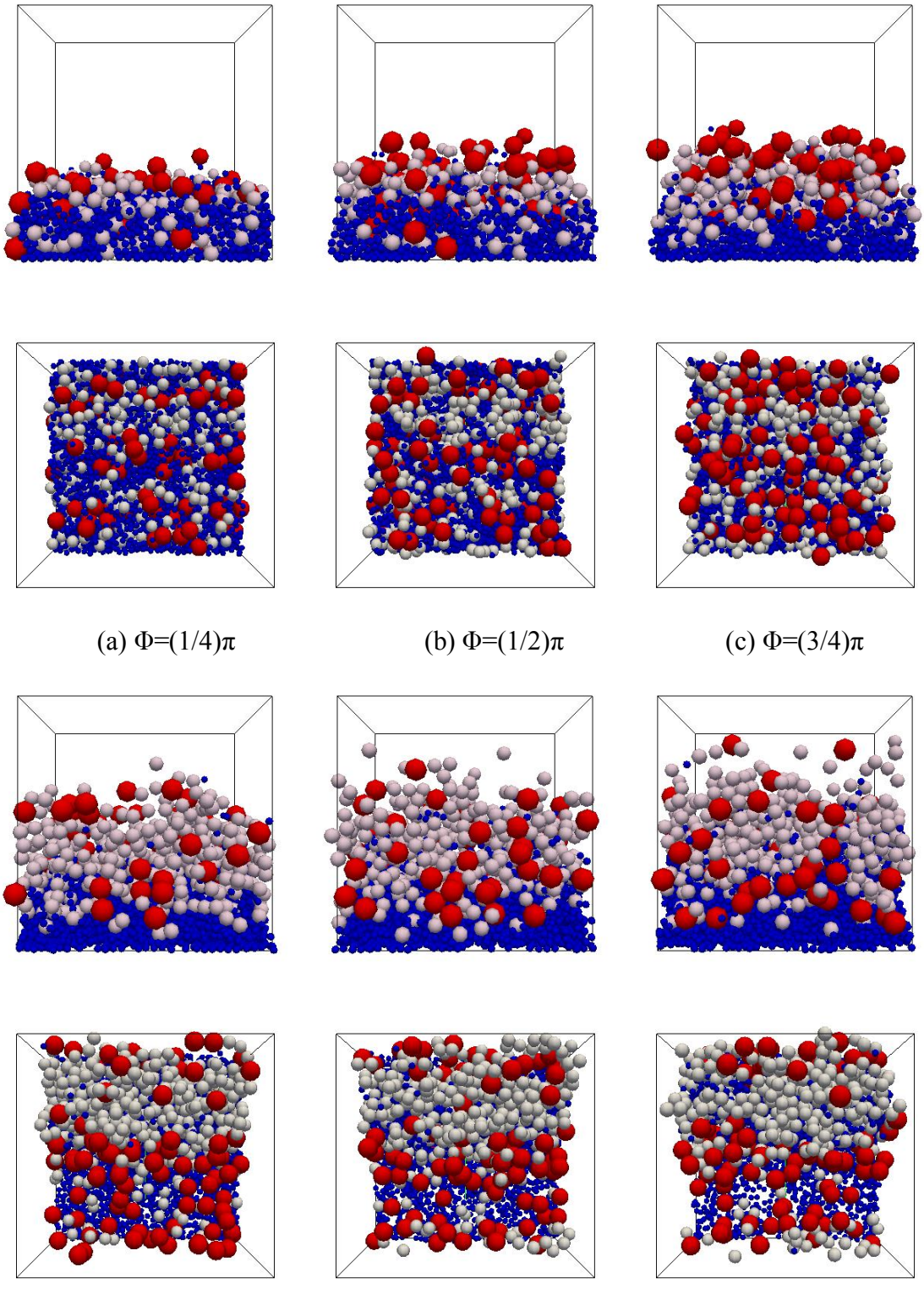

(a) Φ=(1/4)π (b) Φ=(1/2)π (c) Φ=(3/4)π

(d) Φ=(1/4)π (e) Φ=(1/2)π (f) Φ=(3/4)π

Figure 4.4 Snapshots of side/top view of Case 3 in the developing stage of grading (a, b, c) and developed stage of grading (d, e, f).

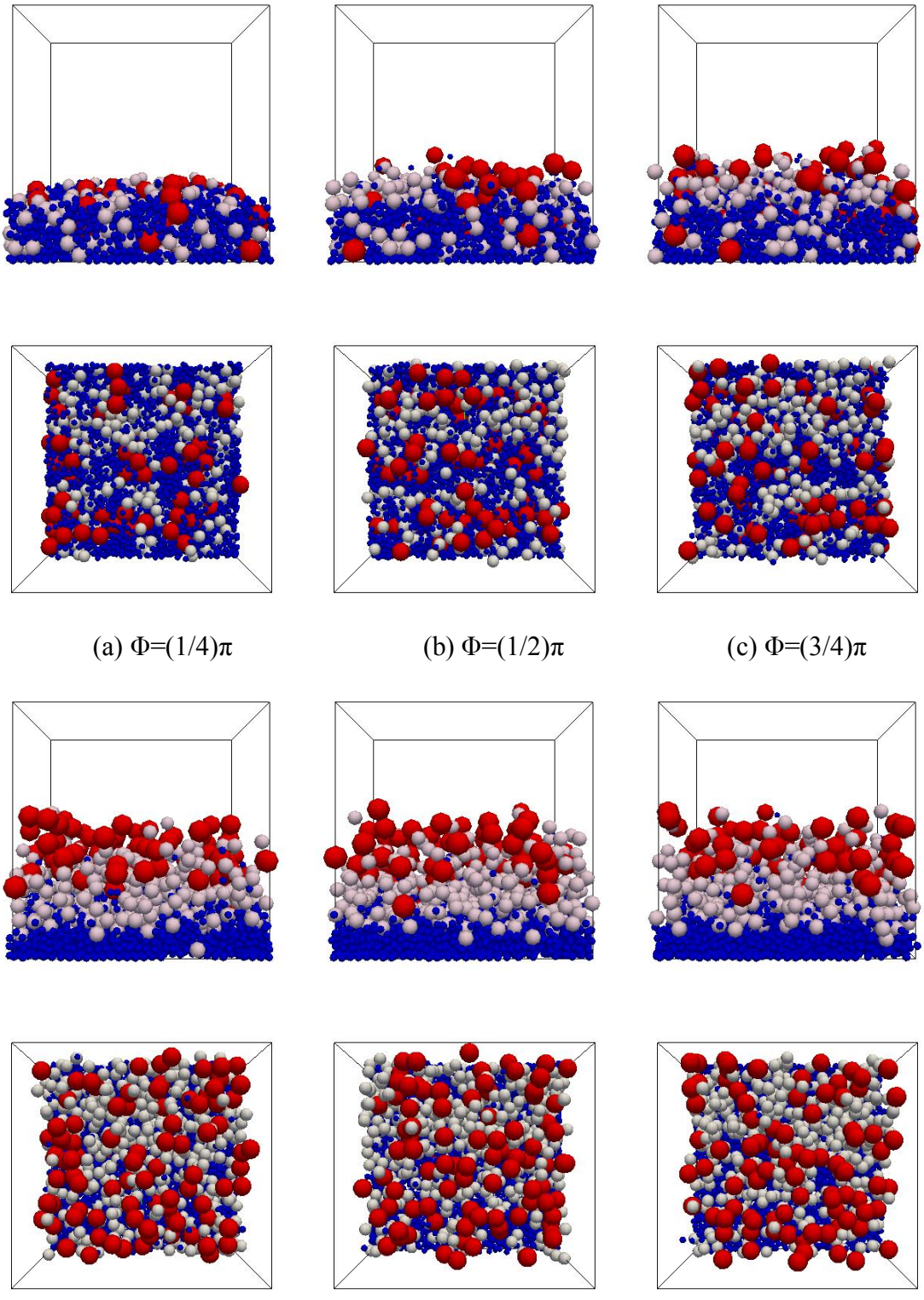

(a) Φ=(1/4)π (b) Φ=(1/2)π (c) Φ=(3/4)π

(d) Φ=(1/4)π (e) Φ=(1/2)π (f) Φ=(3/4)π

Figure 4.5 snapshots of side/top view of Case 4 in the developing stage of grading (a, b, c) and developed stage of grading (d, e, f)

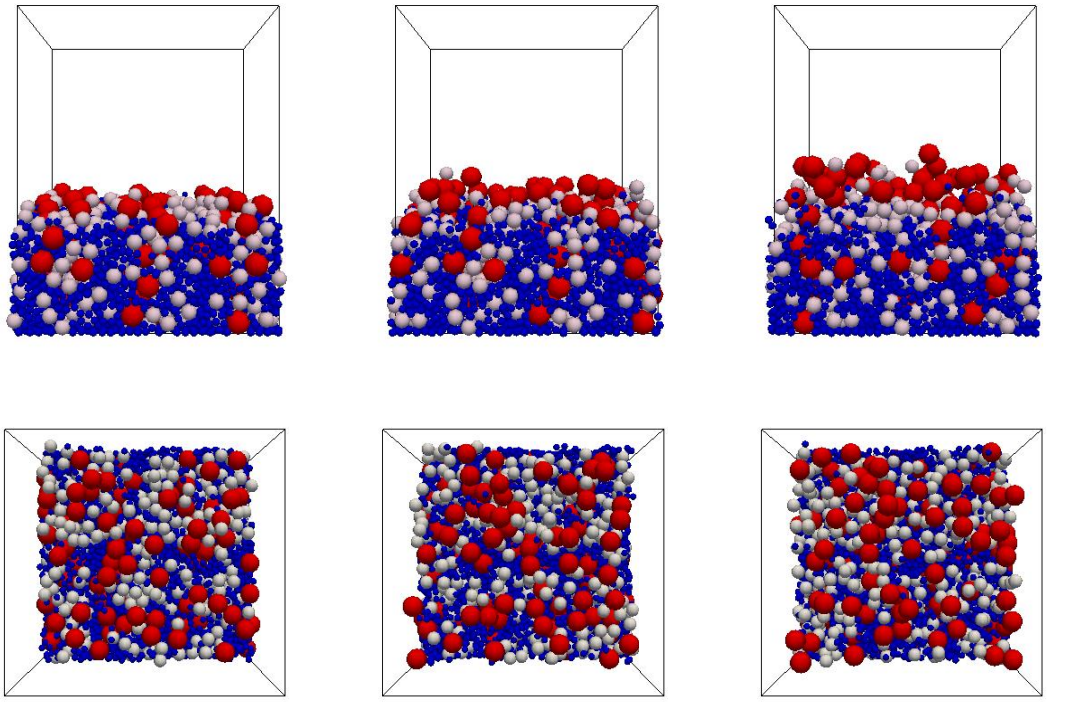

(a) Φ=(1/4)π (b) Φ=(1/2)π (c) Φ=(3/4)π

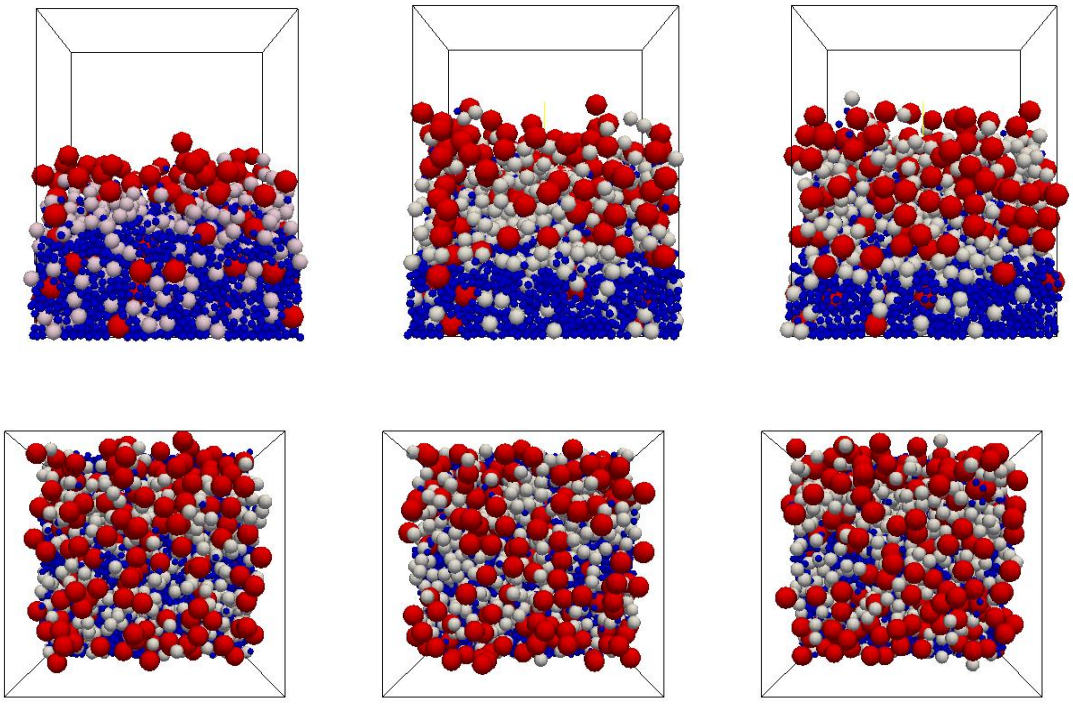

(d) Φ=(1/4)π (e) Φ=(1/2)π (f) Φ=(3/4)π

Figure 4.6 Snapshots of side/top view of Case 5 in the developing stage of grading (a, b, c) and developed stage of grading (d, e, f).

4.3.2 Concentration centroids of mixed sands

The centroid of concentration of particles is an important parameter to judge the vertical sorting process of mixed grain size sediments. It is defined as the deviation of the summary of centers of an individual group of one uniform grain size sediments to that of the initial condition. For instance, the vertical centroids of concentration of particles are determined by the following equation.

$$z^*_{gck} = z_i|t - z_i|t = 0 \tag{4.1}$$

The subscribe i=1, 2, 3 represents small, middle and large particles with diameter of di. $z_i|t=0$ is the initial vertical centroids of concentration of particles and zi|t is the vertical centroids of concentration of particles calculated by

$$z_i|t = \frac{\sum_n zc_i}{n_i} \tag{4.2}$$

where zc_i is the center of particles with the diameter of d_i, and n_i is the number of particles with the diameter of d_i.

The vertical centroids of concentration of particles of all cases (except Case 3 with double period) show that after 2 periods, become horizontal, which shows that the vertical sorting process is completed.

The vertical centroids of concentration of Case 1 and Case 4 (with slop bottom) are quite similar, which indicates that slop bottom is not a key influence factor to the vertical sorting of mixed sands. The centroids of concentrations of large and middle particles of Case 2 (smaller Shield parameter) and Case 5 (double bottom layer thickness) are lower than that of Case 1 while the centroids of concentrations of small particles are higher than that of Case 1. The centroids of concentration of case 3 (double period) arises after 1.5T, when armoring starts to break.

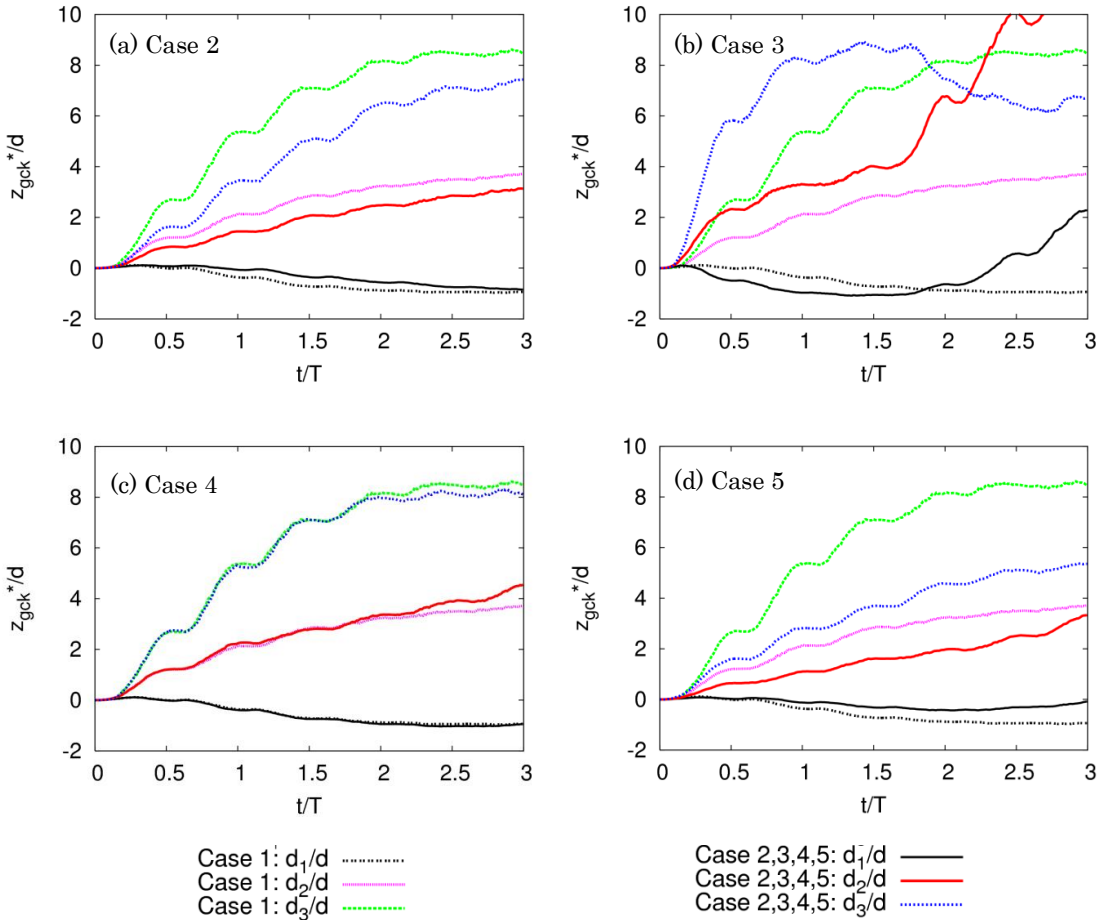

Figure 4.7 Comparisons of vertical centroids of concentration of particles between Case 1 and other 4 cases. The symbol "z_{gck}*" shows the deviation of the vertical centroid of concentrations of particle-diameter class from its initial value.

The horizontal centroids of concentration of particles of all cases (except Case 3 with double period) show that after 2 periods, shows no significant difference in the first two periods and a slight deviation of particles in different grain diameter in the third period, when the vertical sorting is fully developed.

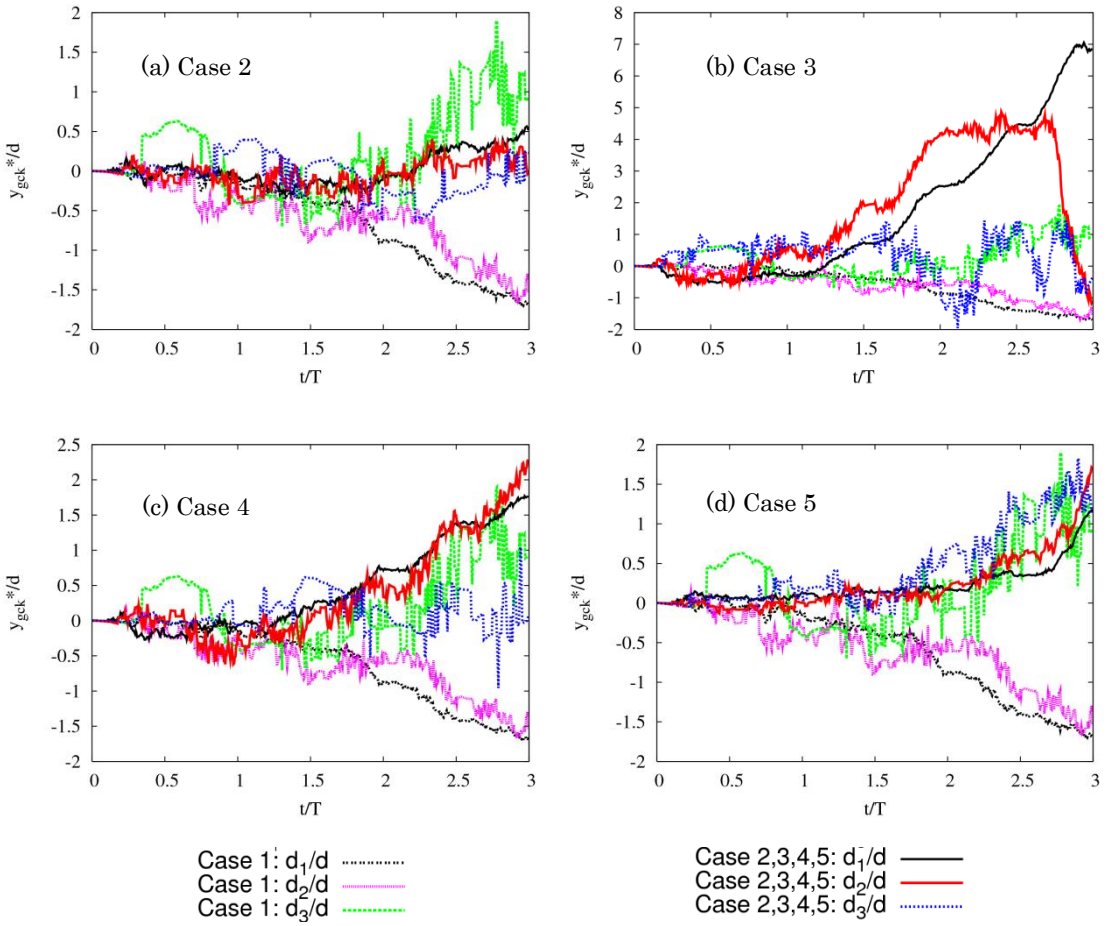

Figure 4.8 Comparisons of horizontal centroids of concentration of particles between Case 1 and other 4 cases. The symbol "y_{gck}*" shows the deviation of the horizontal centroid of concentrations of particle-diameter class from its initial value.

4.3.3 Mean velocity of sediment particles

Figure 4.9 – **Figure 4.13** show the dimensionless mean velocity of sediment particles, namely the average particle velocity with the same diameter (upi) over the maximum particle velocity in one period (upmax).

In **Fig. 4.9** for Case 1, in the accelerating phase ($\Phi=1/4\pi$), at the maximum velocity phase ($\Phi=1/2\pi$) and in the decelerating phase ($\Phi=1/4\pi$) in the developing stage of grading, velocity of all particle show almost the same distribution of downward convex velocity profile. At the maximum velocity phase and decelerating phase in the fully developed stage of grading, the velocity profile of small particle does not reach the upper layer, as armoring effects. And the distribution of all particles in the fully developed stage of grading show a linear profile in the accelerating phase, and an tendency of upward convex profile at the maximum velocity phase and in the decelerating phase.

The mean velocity profiles of sediment particles in the other four cases in the developing stage of grading are quite similar to Case 1. However, it is quite different in the fully developed stage of grading, except Case 2 and Case 4. The velocity distributions in Case 5 show significant upward convex profile at all three phases (**Fig. 4.13d, e, f**). The velocity profile of Case 3 show parabola distributions and the mean velocity of middle particle reach to high position, which indicates the suspension of middle particle after armoring break.

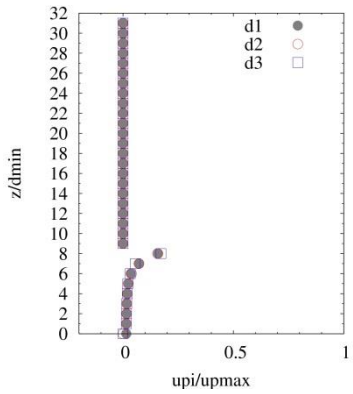

(a) Φ=(1/4)π

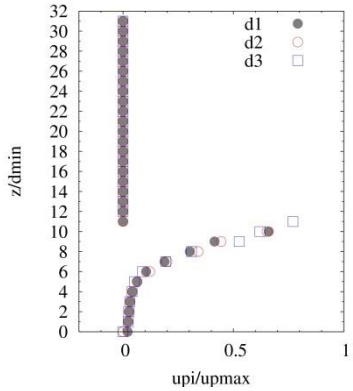

(b) Φ=(1/2)π

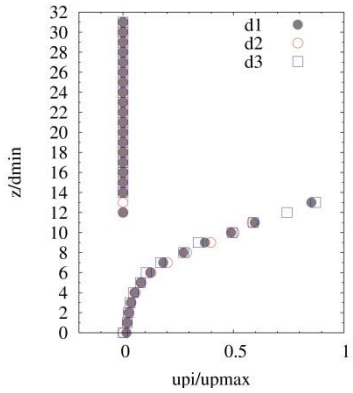

(c) Φ=(3/4)π

Developing stage of grading

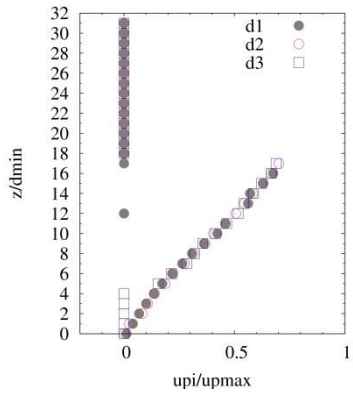

(d) Φ=(1/4)π

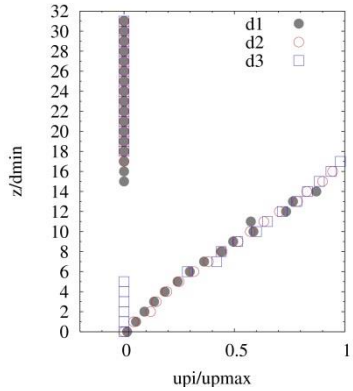

(e) Φ=(1/2)π

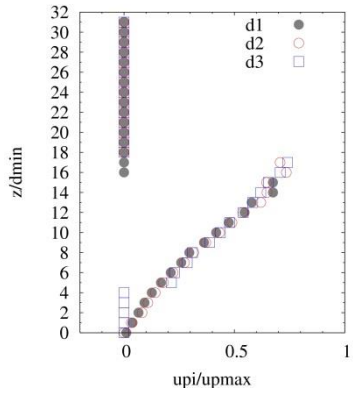

(f) Φ=(3/4)π

Developed stage of grading

Figure 4.9 Mean velocity profiles of sediment particles in Case 1 in the developing stage of grading (a, b, c) and developed stage of grading (d, e, f).

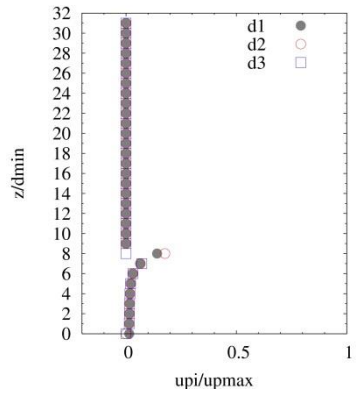

(a) Φ=(1/4)π

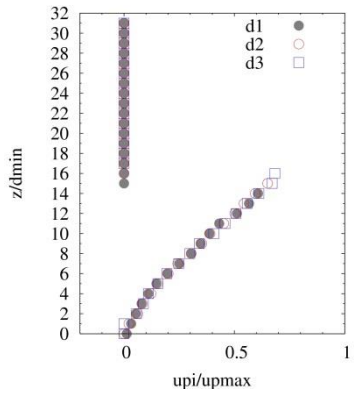

(d) Φ=(1/4)π

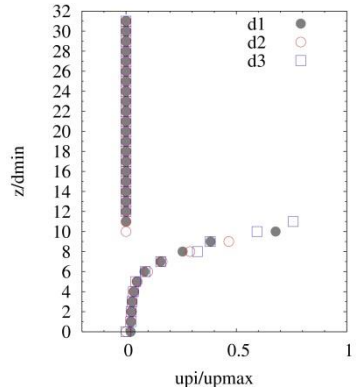

(b) Φ=(1/2)π

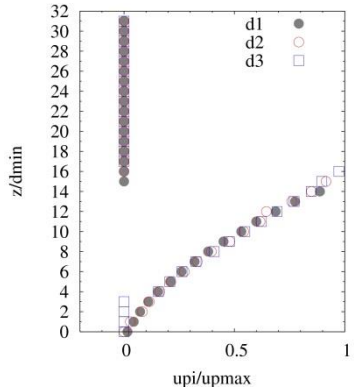

(e) Φ=(1/2)π

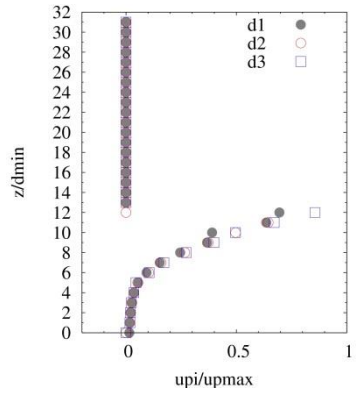

(c) Φ=(3/4)π

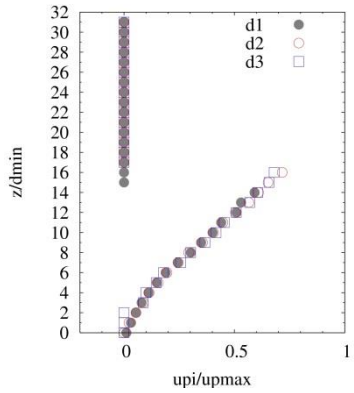

(f) Φ=(3/4)π

Developing stage of grading Developed stage of grading

Figure 4.10 Mean velocity profiles of sediment particles in Case 2 in the developing stage of grading (a, b, c) and developed stage of grading (d, e, f).

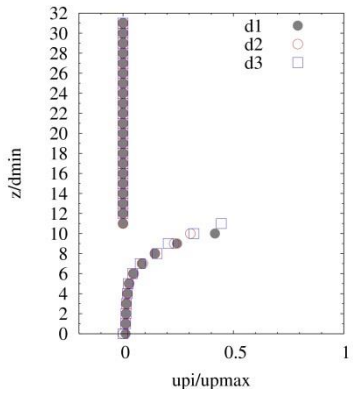

(a) Φ=(1/4)π

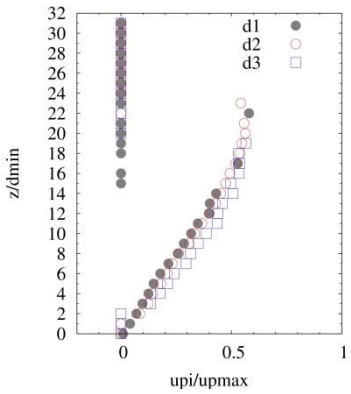

(d) Φ=(1/4)π

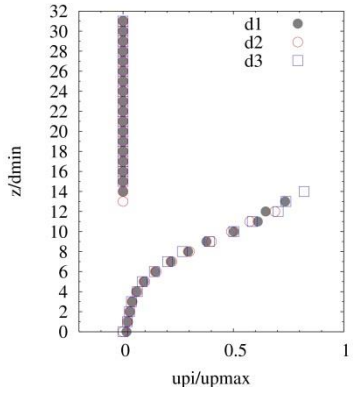

(b) Φ=(1/2)π

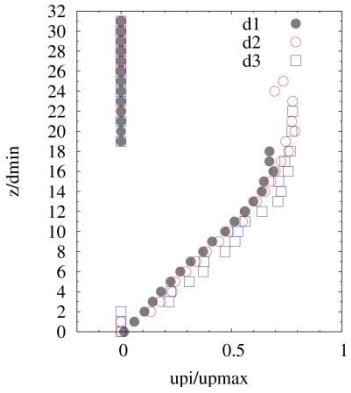

(e) Φ=(1/2)π

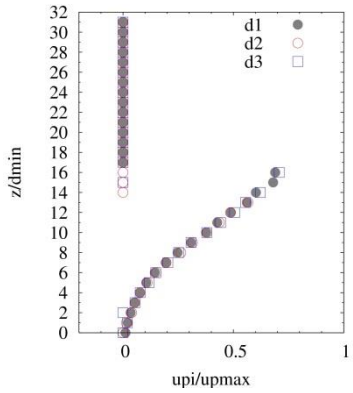

(c) Φ=(3/4)π

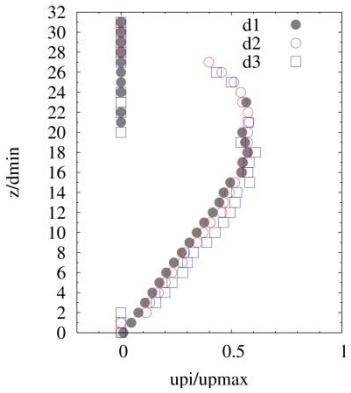

(f) Φ=(3/4)π

Developing stage of grading Developed stage of grading

Figure 4.11 Mean velocity profiles of sediment particles in Case 3 in the developing stage of grading (a, b, c) and developed stage of grading (d, e, f)

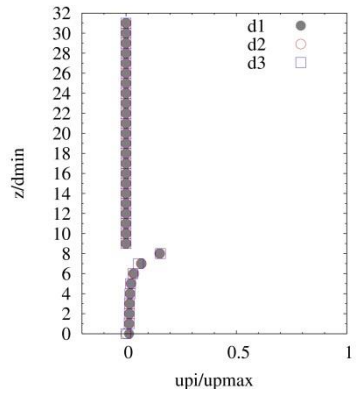

(a) Φ=(1/4)π

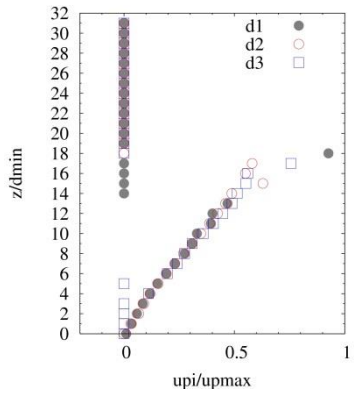

(d) Φ=(1/4)π

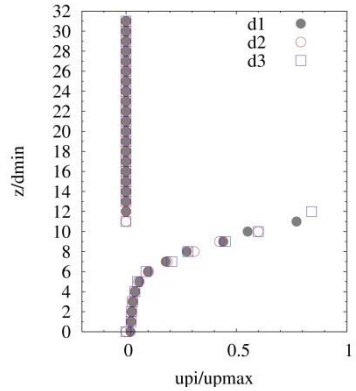

(b) Φ=(1/2)π

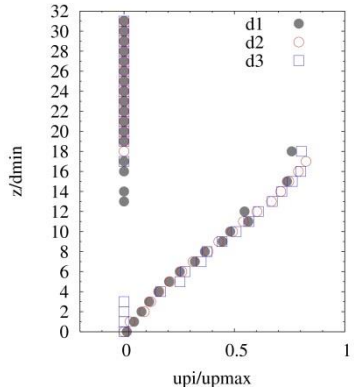

(e) Φ=(1/2)π

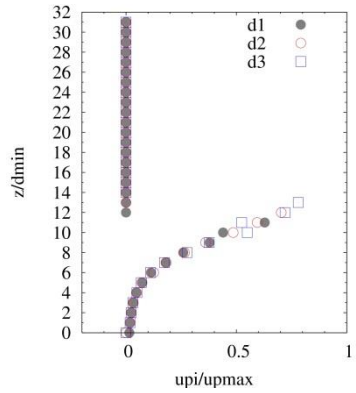

(c) Φ=(3/4)π

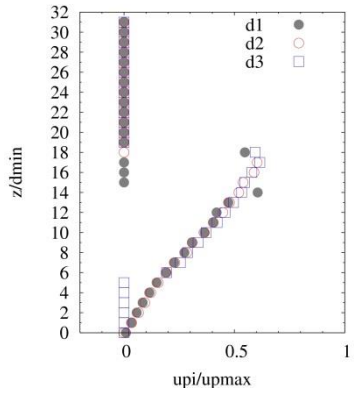

(f) Φ=(3/4)π

Developing stage of grading Developed stage of grading

Figure 4.12 Mean velocity profiles of sediment particles in Case 4 in the developing stage of grading (a, b, c) and developed stage of grading (d, e, f).

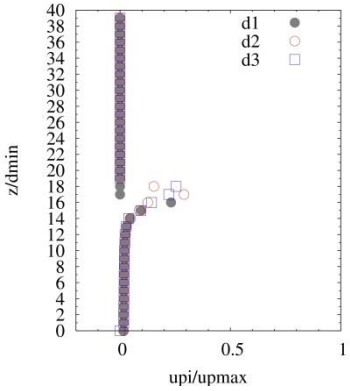

(a) Φ=(1/4)π

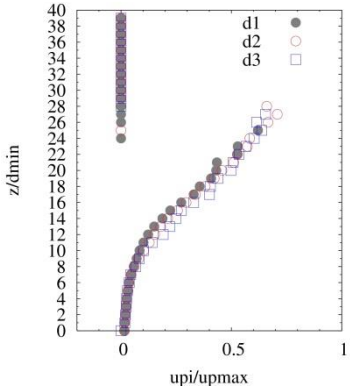

(d) Φ=(1/4)π

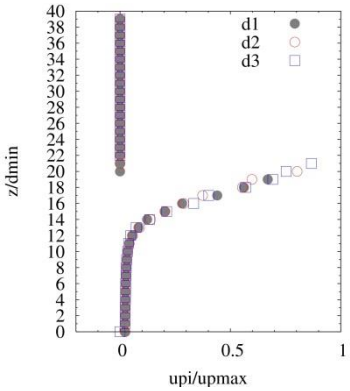

(b) Φ=(1/2)π

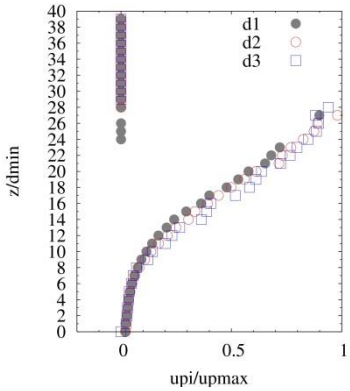

© Φ=(1/2)π

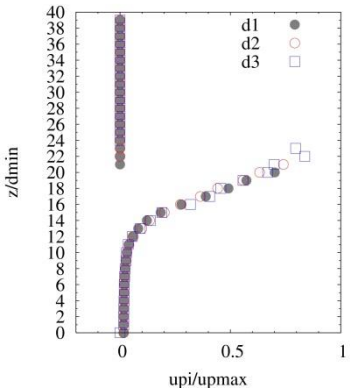

(c) Φ=(3/4)π

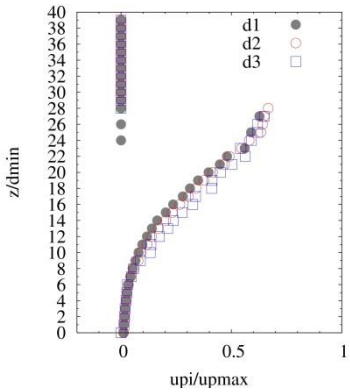

(f) Φ=(3/4)π

Developing stage of grading

Developed stage of grading

Figure 4.13 Mean velocity profiles of sediment particles in Case5 in the developing stage of grading (a, b, c) and developed stage of grading (d, e, f).

4.3.4 Dimensionless particle number density distribution

The dimensionless particle number density is an important factor to calculate the sediment transport rate. The method of calculating particle number density is quite different from Gotoh and Sakai (1997). It is simplified by counting the number of particles with particle center in the range of selected particle layers, multiplying the volume of each group of particle with the counted number and then dividing with the whole volume of the selected particle layers.

In **Fig. 4.14** of Case 1, the dimensionless particle number density distribution of small particles show a decrease along z-axis in the developing stage of grading. While the dimensionless particle number distribution of large particles increase in the vertical direction, especially in the decelerating phase of developing stage of grading. In the fully developed stage, the dimensionless number density profile of small particles show downward convex of distribution from the accelerating phase on. The vertical sorting of mixed sands can be found by a significant stratified distribution of dimensionless number density distribution with large particles on the top and small particles at the bottom in the fully developed stage of grading (**Fig. 4.14 d, e, f**).

Similar distributions can be found in the other cases expect Case 3 with double period. In the accelerating phase and at the maximum velocity phase, the distribution of particle number with all particles and the particle number with small and middle particles are quite similar, which means the vertical sorting failed due to the breaking of armoring effect.

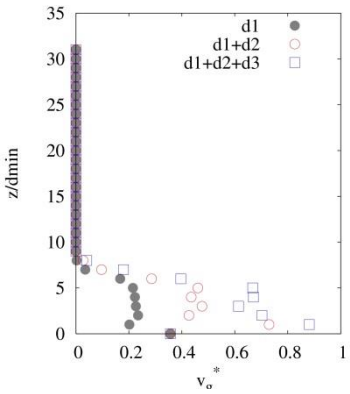

(a) Φ=(1/4)π

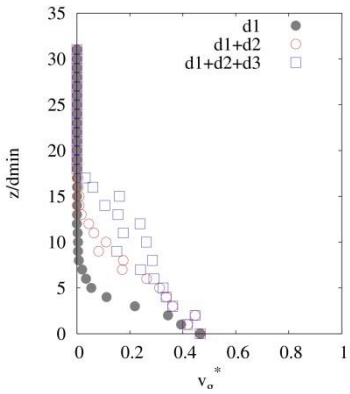

(d) Φ=(1/4)π

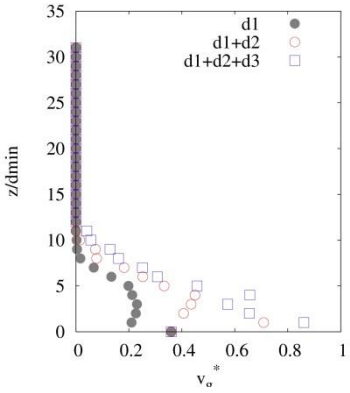

(b) Φ=(1/2)π

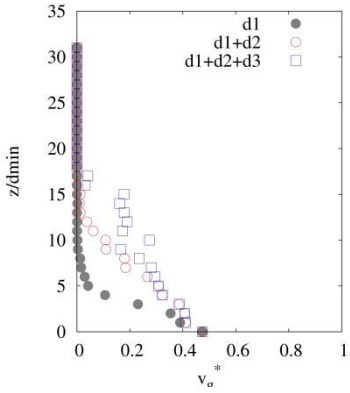

(e) Φ=(1/2)π

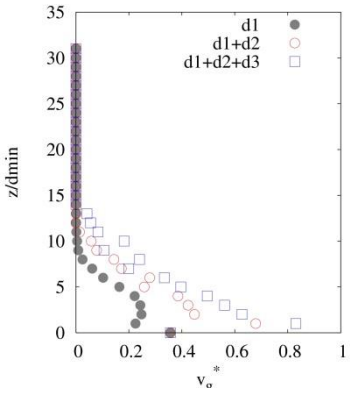

(c) Φ=(3/4)π

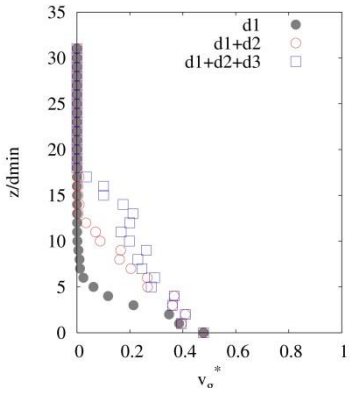

(f) Φ=(3/4)π

Developing stage of grading Developed stage of grading

Figure 4.14 Dimensionless particle number density distribution of Case 1 in the developing stage of grading (a, b, c) and developed stage of grading (d, e, f).

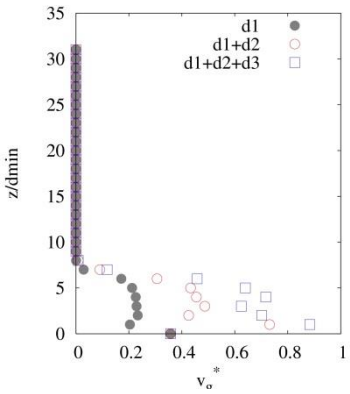

(a) Φ=(1/4)π

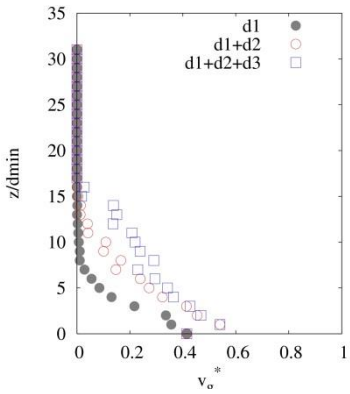

(d) Φ=(1/4)π

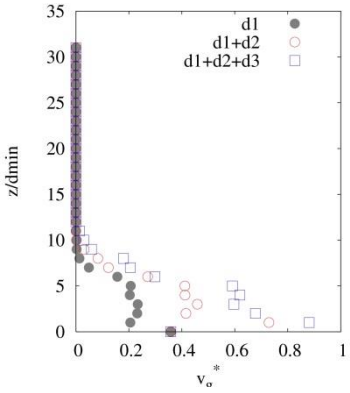

(b) Φ=(1/2)π

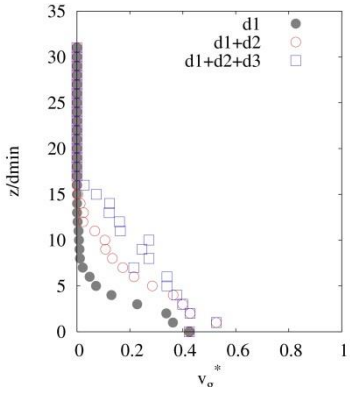

(e) Φ=(1/2)π

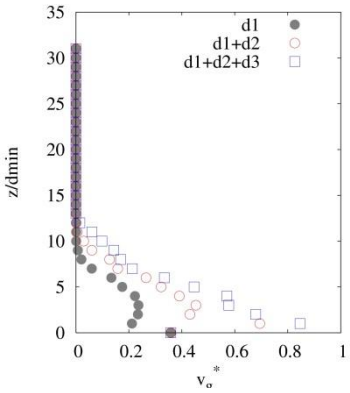

(c) Φ=(3/4)π

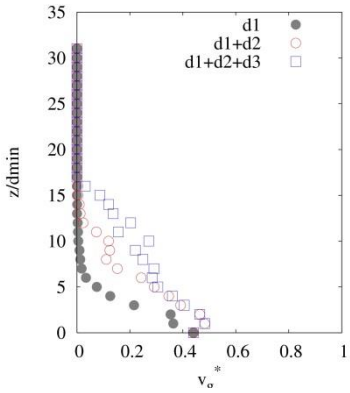

(f) Φ=(3/4)π

Developing stage of grading Developed stage of grading

Figure 4.15 Dimensionless particle number density distribution of Case 2 in the developing stage of grading (a, b, c) and developed stage of grading (d, e, f).

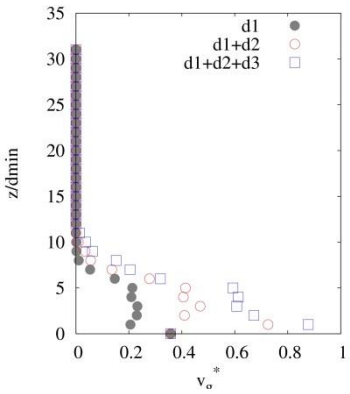

(a) Φ=(1/4)π

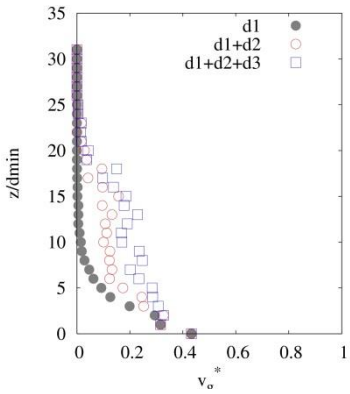

(d) Φ=(1/4)π

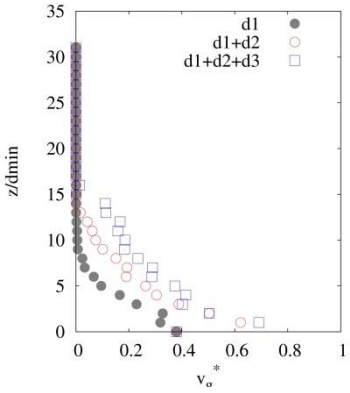

(b) Φ=(1/2)π

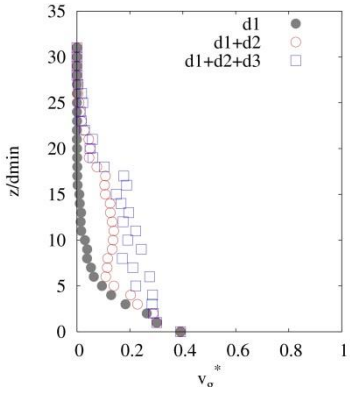

(e) Φ=(1/2)π

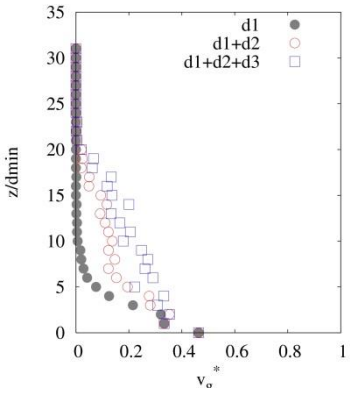

(c) Φ=(3/4)π

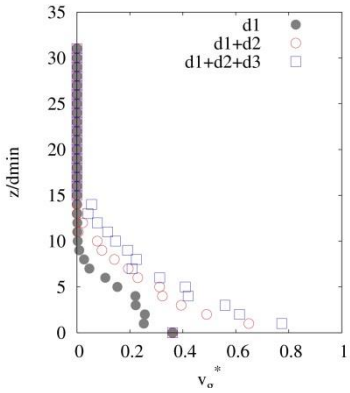

(f) Φ=(3/4)π

Developing stage of grading Developed stage of grading

Figure 4.16 Dimensionless particle number density distribution of Case 3 in the developing stage of grading (a, b, c) and developed stage of grading (d, e, f).

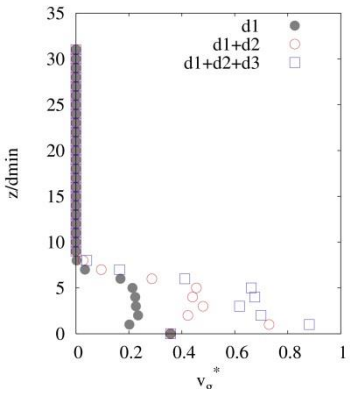

(a) Φ=(1/4)π

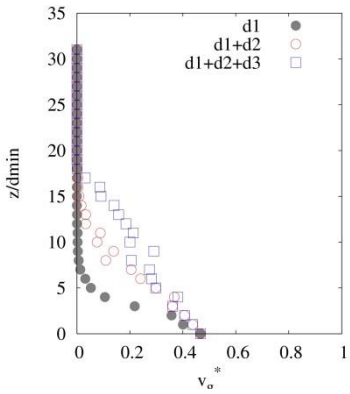

(d) Φ=(1/4)π

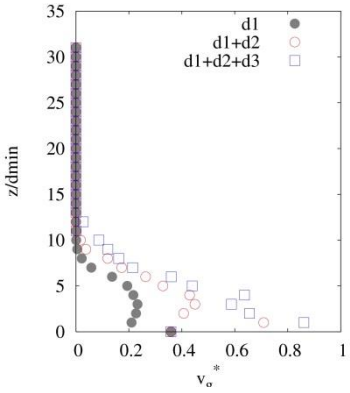

(b) Φ=(1/2)π

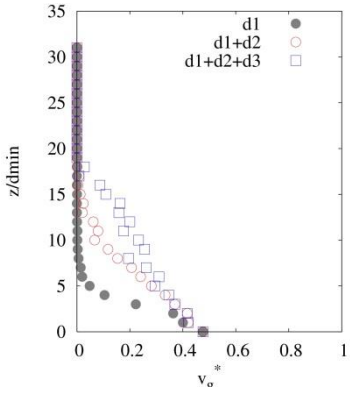

(e) Φ=(1/2)π

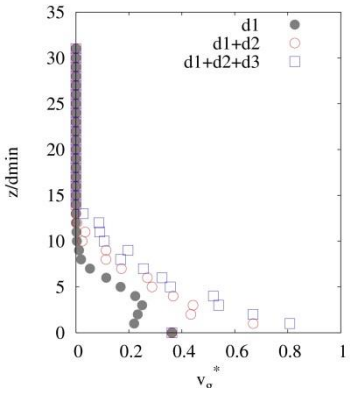

(c) Φ=(3/4)π

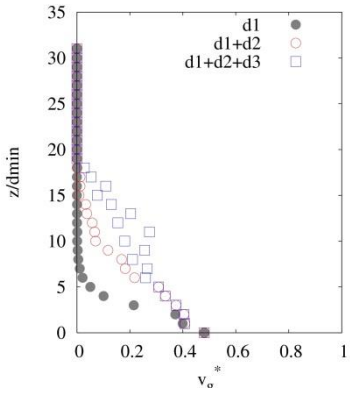

(f) Φ=(3/4)π

Developing stage of grading Developed stage of grading

Figure 4.17 Dimensionless particle number density distribution of Case 4 in the developing stage of grading (a, b, c) and developed stage of grading (d, e, f).

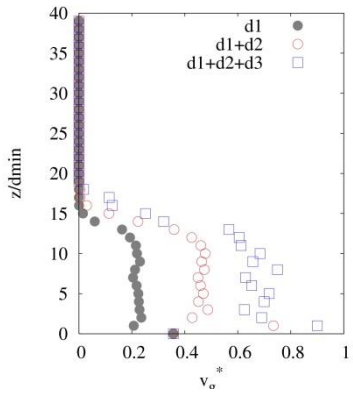

(a) Φ=(1/4)π

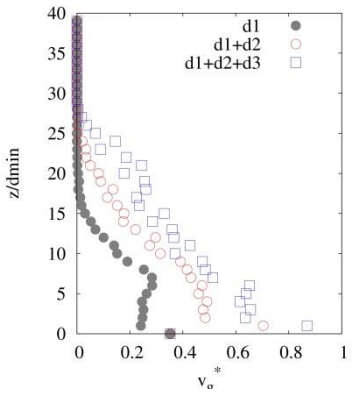

(d) Φ=(1/4)π

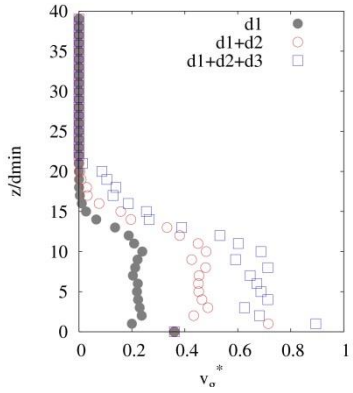

(b) Φ=(1/2)π

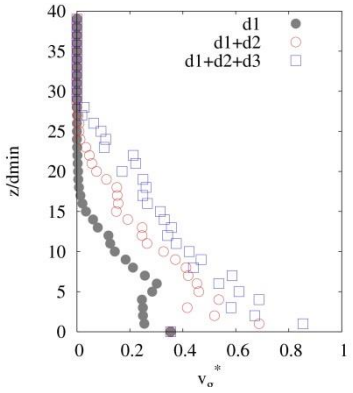

(e) Φ=(1/2)π

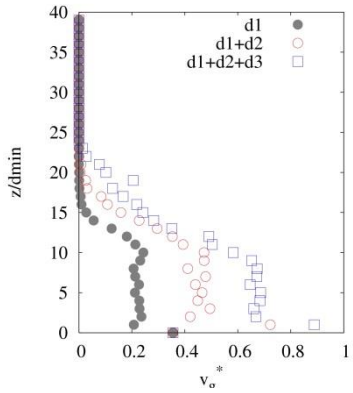

(c) Φ=(3/4)π

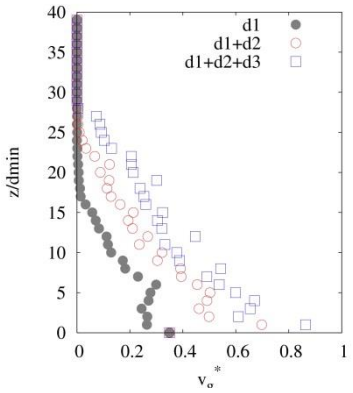

(f) Φ=(3/4)π

Developing stage of grading Developed stage of grading

Figure 4.18 Dimensionless particle number density distribution of Case 5 in the developing stage of grading (a, b, c) and developed stage of grading (d, e, f).

4.4 Simulation Results of Mixed Sands under Progressive Cnoidal Wave

4.4.1 Cnoidal wave

The second approximation of cnoidal wave theory is applied to generate a cnoidal wave with a still water depth of 20cm, wave height of 14cm and period of 1.4s. **Figure 4.19** shows the some phase of the free surface of water level elevation of the simulated progressive cnoidal wave. Still water depth of 20cm is given as the initial set of the cnoidal wave. Water level elevation together the horizontal and vertical velocities of water particles in the cnoidal wave are given as boundary conditions at the left and right boundary. **Figure 4.19b** – **Figure 4.19i** show phases in a complete cycle with an interval of 1/4π.

(a) initial

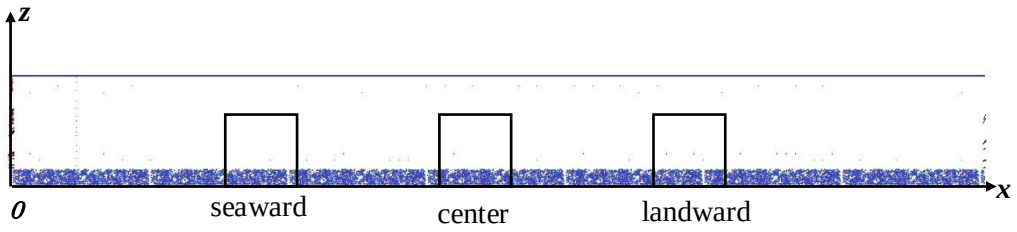

(b) Φ=(1/4)π

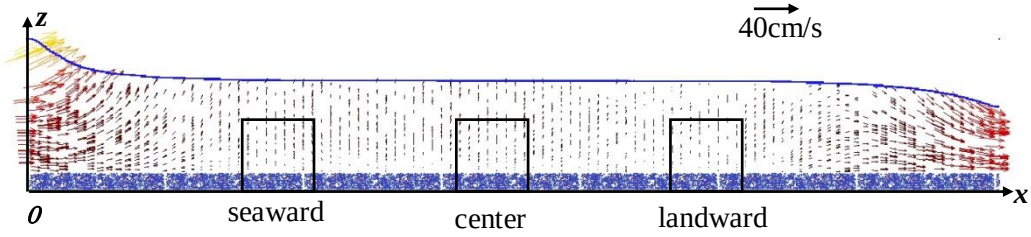

(c) Φ=(2/4)π

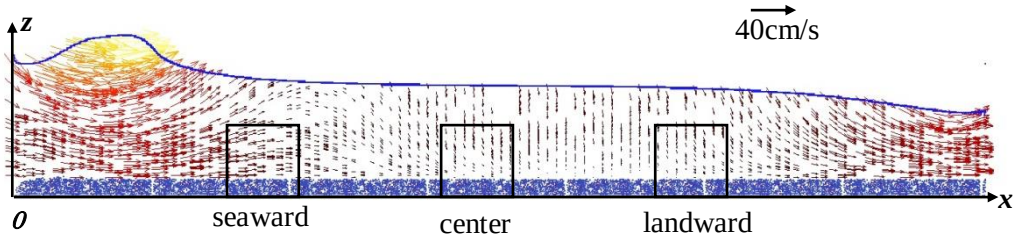

(d) Φ=(3/4)π

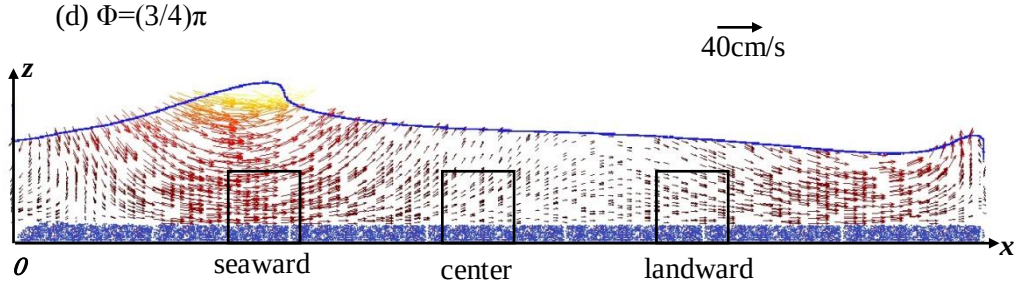

(e) Φ=(4/4)π

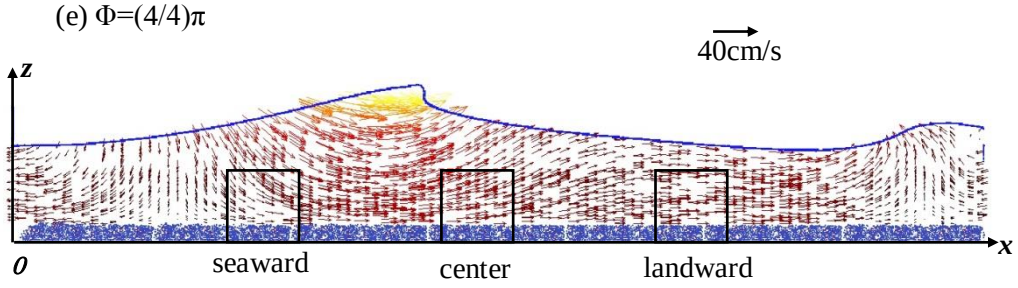

(f) Φ=(5/4)π

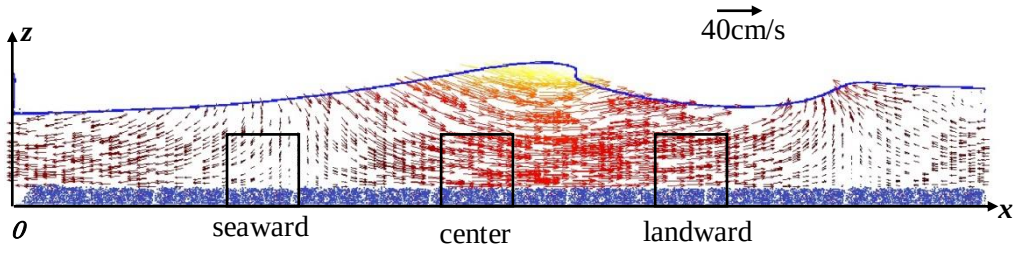

(g) Φ=(6/4)π

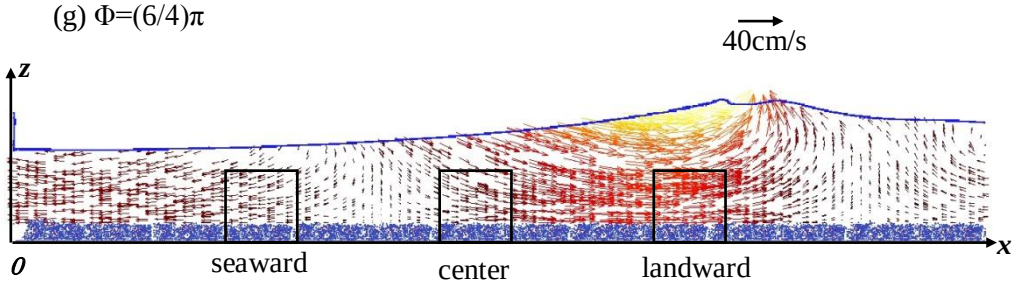

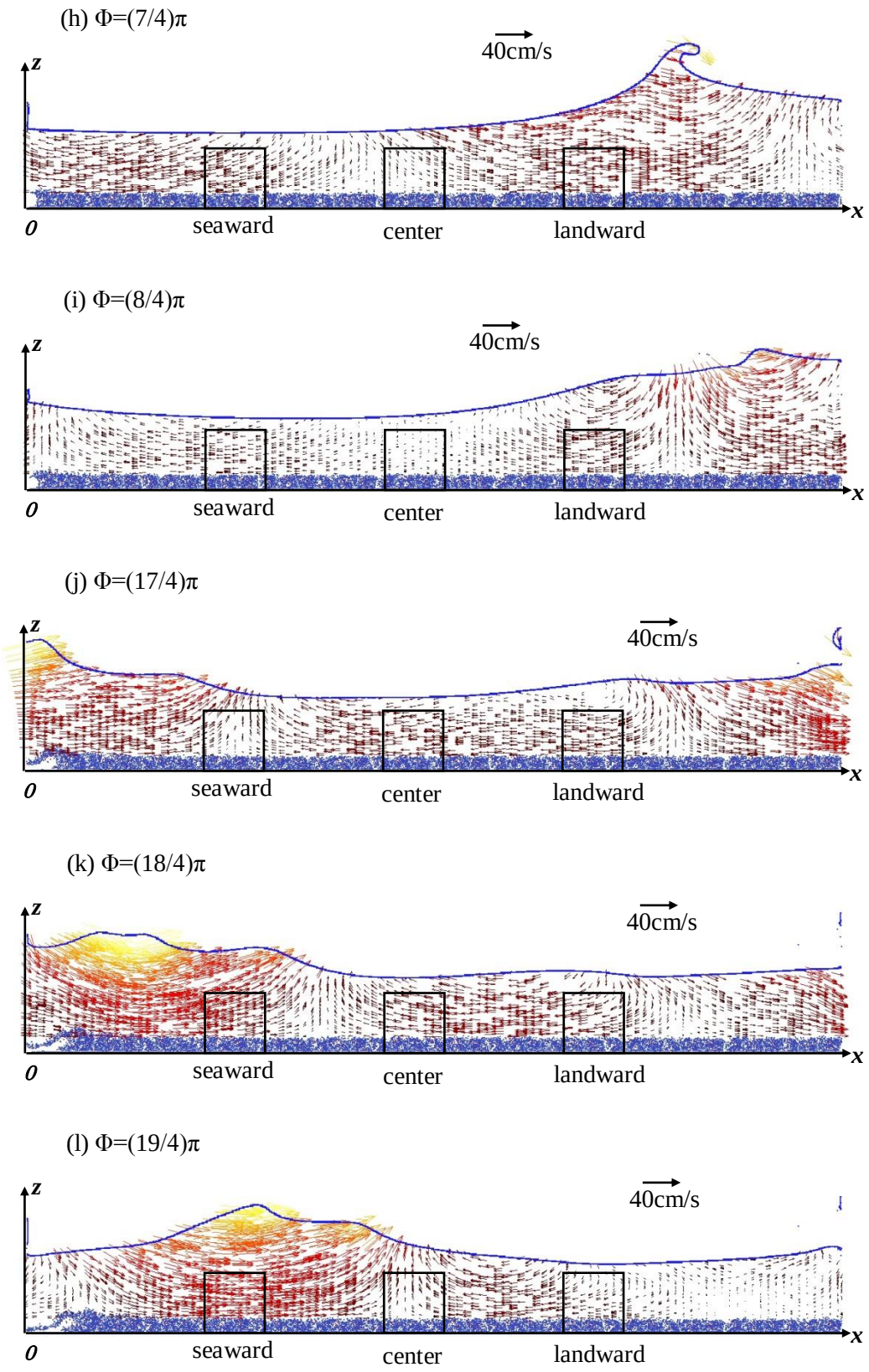

Figure 4. 19 Water elevation and velocity field of wave generated from initial cnoidal wave.

4.4.2 Vertical sorting of mixed sands under cnoidal wave

For clarity, the vertical sorting process of mixed sands in three areas of the whole computation domain, remarked as seaward, center and landward areas (**Fig. 4.19**), with sub-computation domains of 16×16×16cm, are investigated. **Figure 4.20 - Figure 4.22** show some snapshots of sorting process of mixed grain size sediment under the progressive cnoidal wave in the seaward area, center area and landward area of the computational domain, respectively. Obviously, particles do not start to move (**Fig. 4.20a**, **Fig. 4.21b**, **Fig. 4.22c**) until the bottom velocity is large enough when the wave crest pass by (corresponding to **Fig. 4.19d**, **e**, **f**, respectively). The vertical sorting happens after the wave crest pass by (**Fig. 4.20b**, **Fig. 4.21c**, **Fig. 4.22d**), and promoted in a complete period (**Fig. 4.20f**, **Fig. 4.21f**, **Fig. 4.22f**).

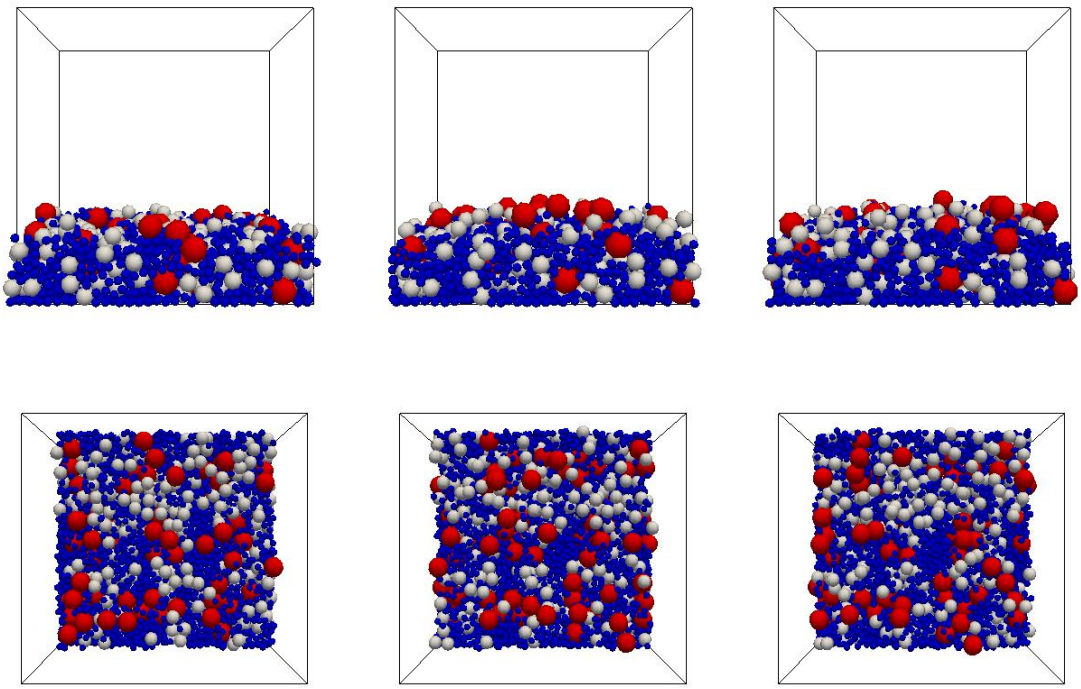

(a) Φ=(3/4)π (b) Φ=(4/4)π (c) Φ=(5/4)π

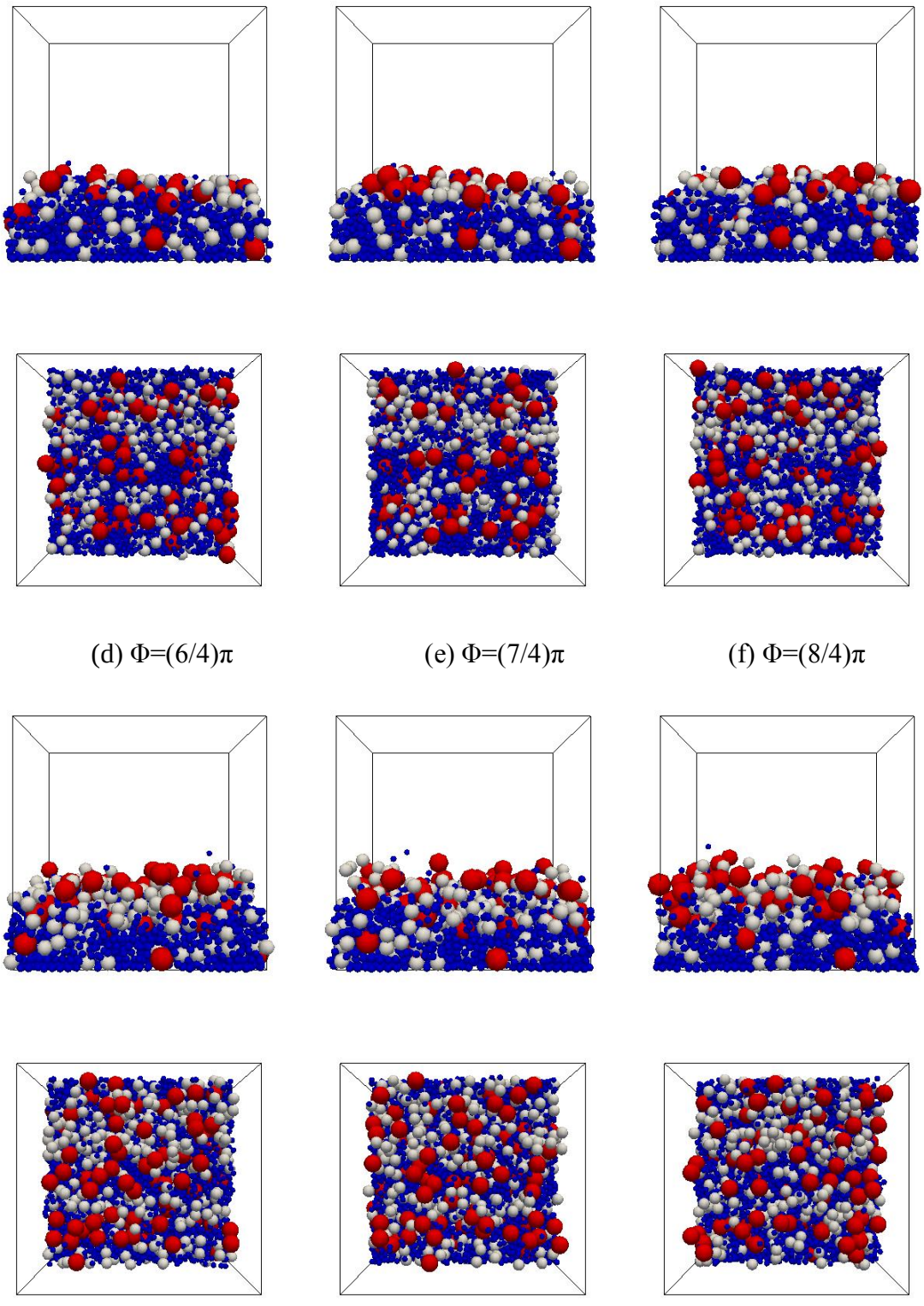

(d) Φ=(6/4)π (e) Φ=(7/4)π (f) Φ=(8/4)π

(g) Φ=(17/4)π (h) Φ=(18/4)π (i) Φ=(19/4)π

Figure 4.20 Snapshots of side/top view in the seaward part of Case 6 in the developing stage of grading (a-f) and developed stage of grading (g-i).

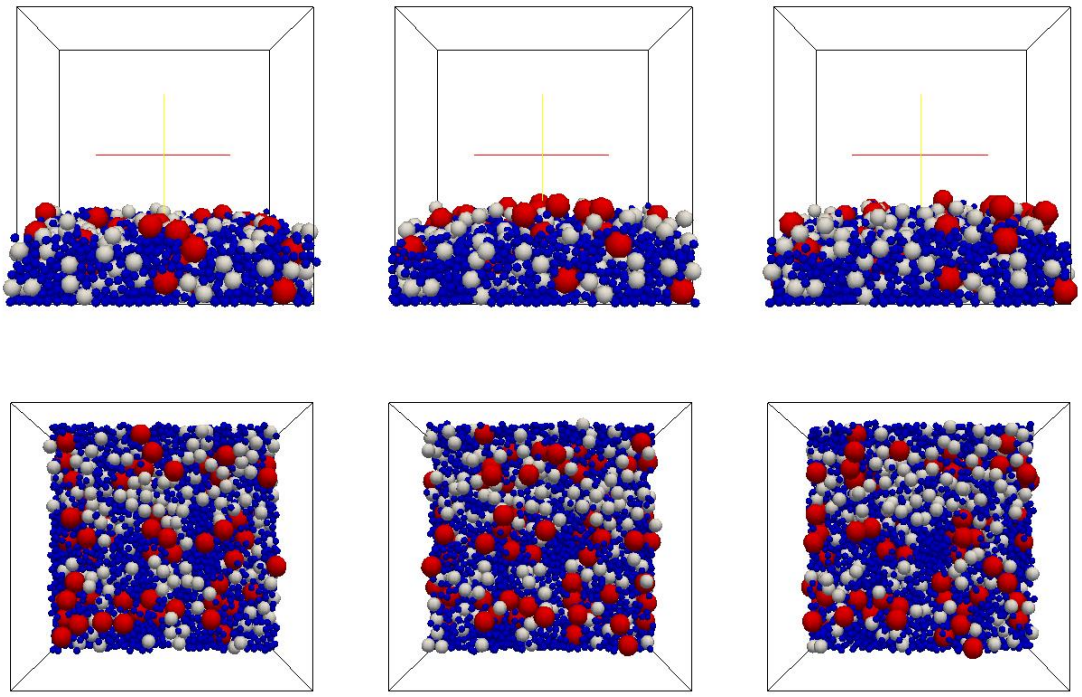

(a) Φ=(3/4)π (b) Φ=(4/4)π (c) Φ=(5/4)π

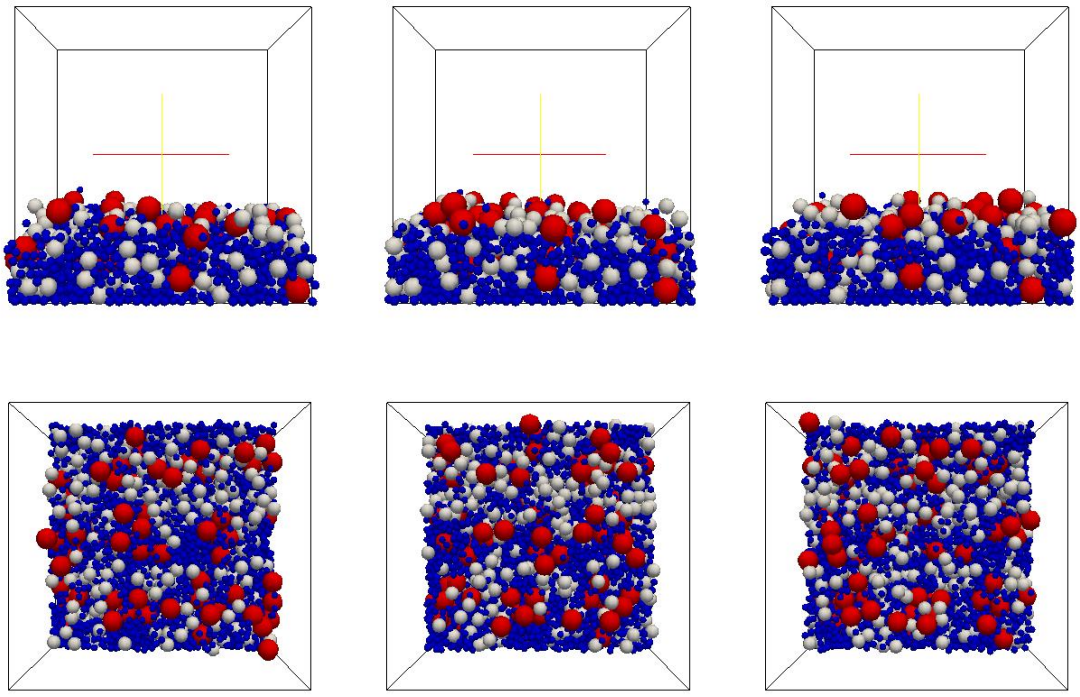

(d) Φ=(6/4)π (e) Φ=(7/4)π (f) Φ=(8/4)π

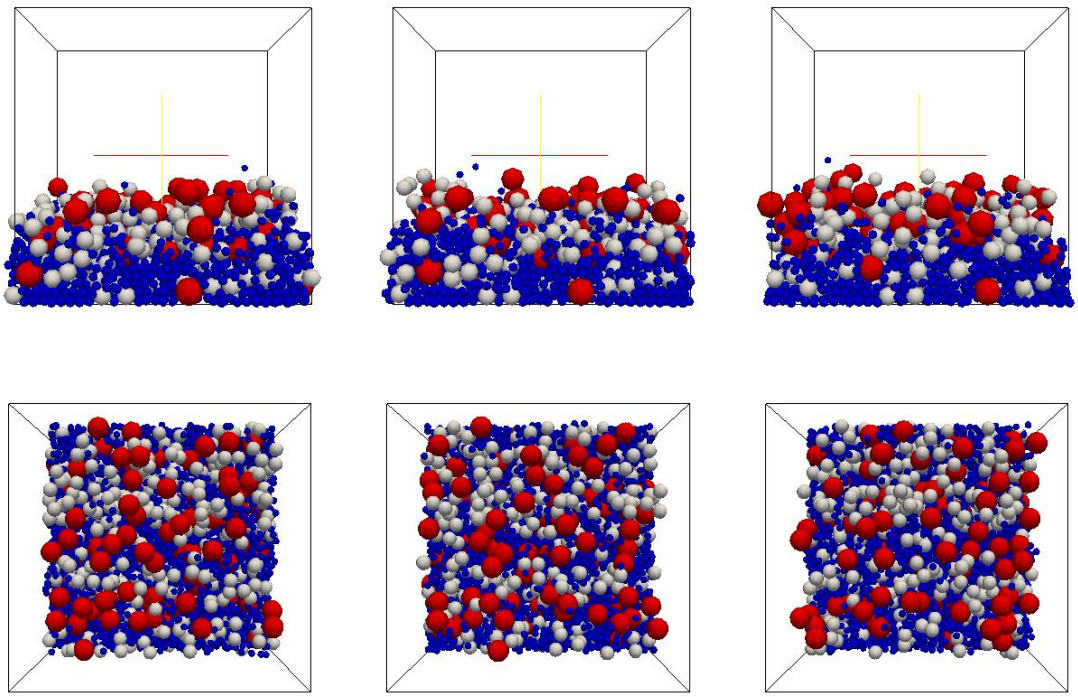

(g) Φ=(17/4)π (h) Φ=(18/4)π (i) Φ=(19/4)π

Figure 4.21 Snapshots of side/top view in the center part of Case 6 in the developing stage of grading (a-f) and developed stage of grading (g-i).

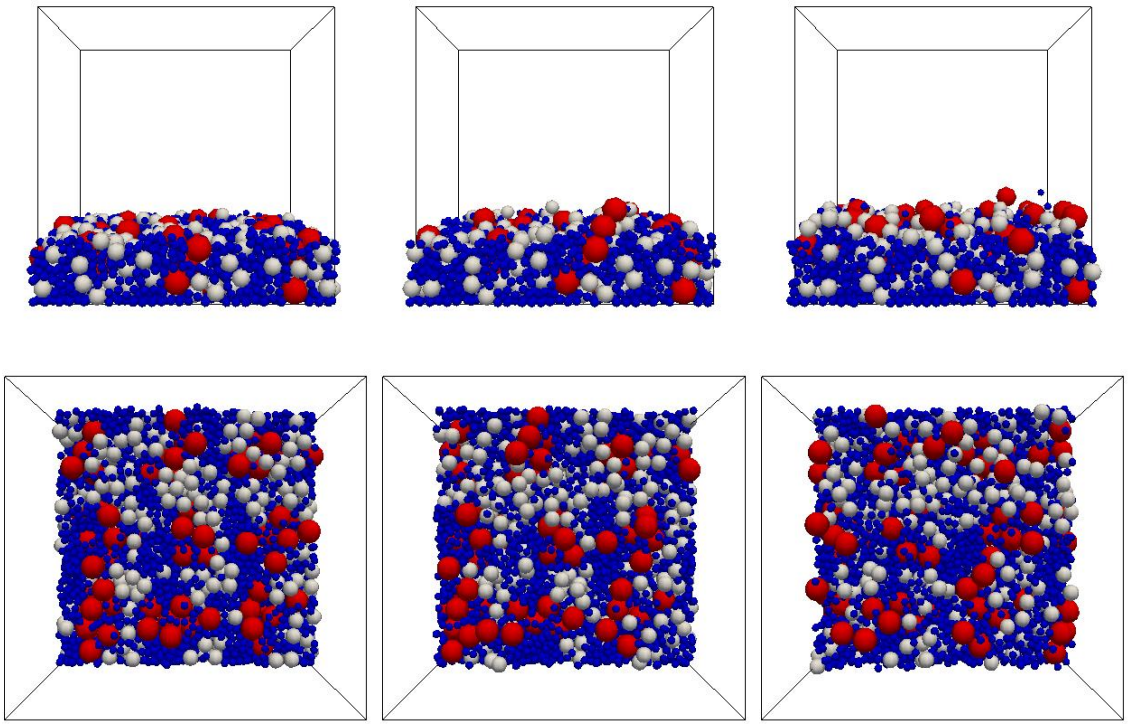

(a) Φ=(3/4)π (b) Φ=(4/4)π (c) Φ=(5/4)π

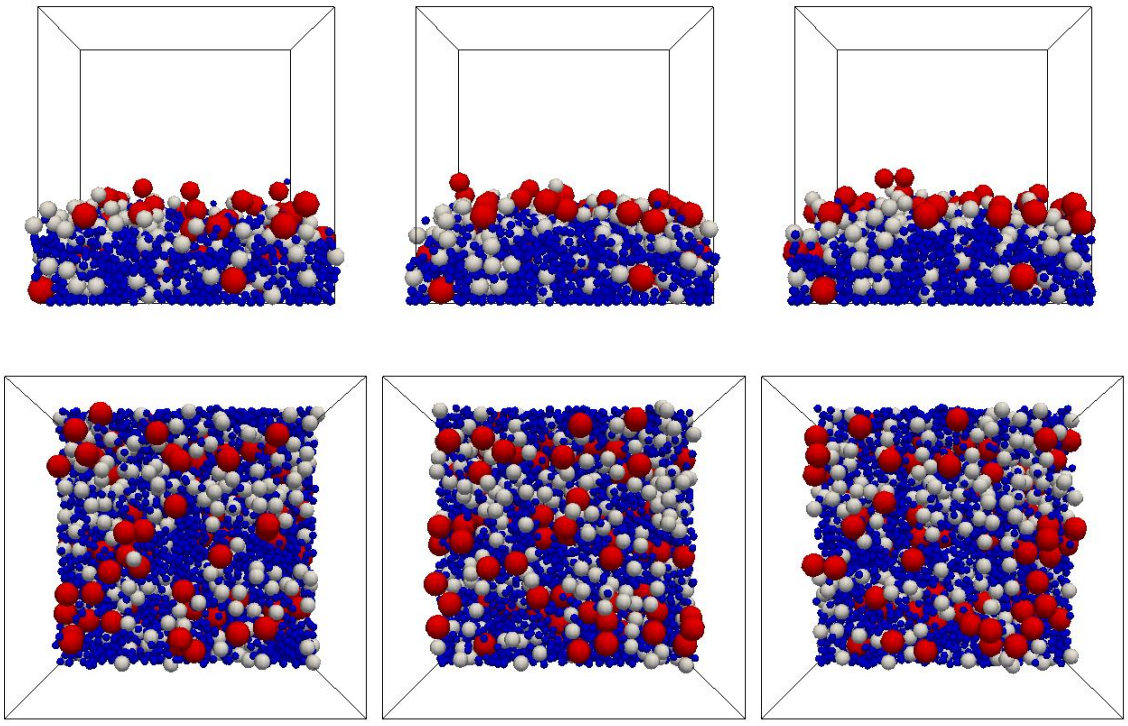

(d) Φ=(6/4)π (e) Φ=(7/4)π (f) Φ=(8/4)π

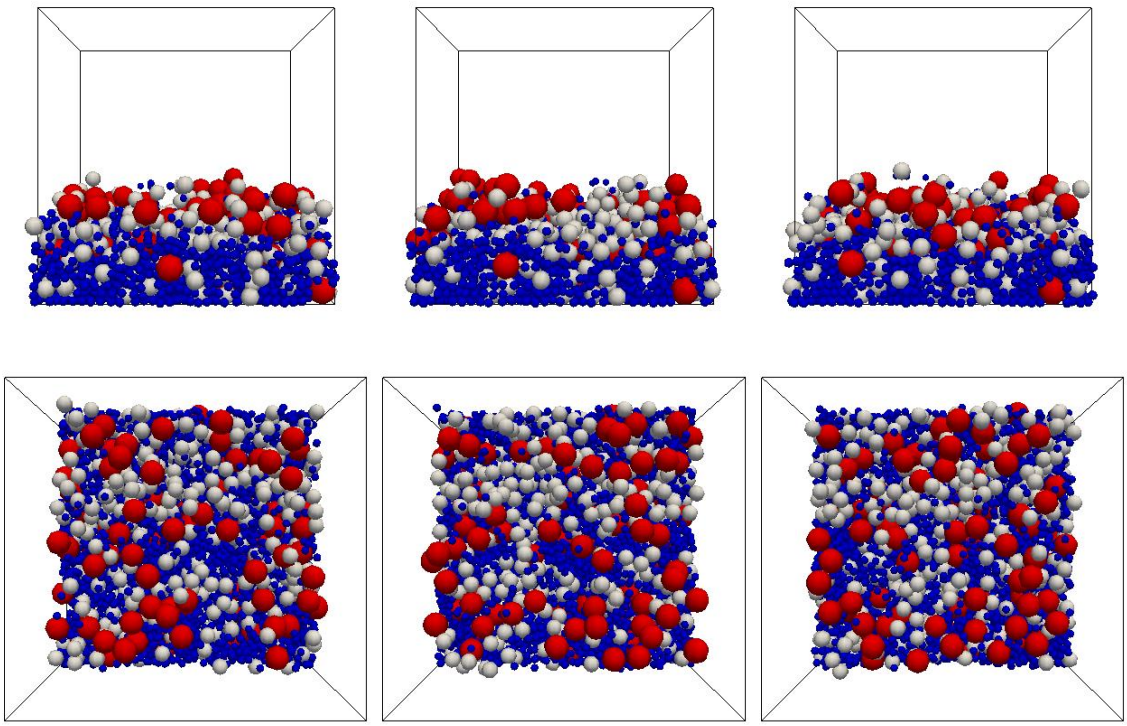

(g) Φ=(17/4)π (h) Φ=(18/4)π (i) Φ=(19/4)π

Figure 4.22 Snapshots of side/top view in the landward part of Case 6 in the developing stage of grading (a-f) and developed stage of grading (g-i).

Figure 4.23 shows the vertical centroids of concentration of particles for landward and seaward, respectively. It indicates that the concentration centroid of particles for overall width is, however, not uniform in wave progressing direction. The concentration centroid of large particles are higher landward from around 0.7T, however, becomes slightly higher seaward after 2.4T (**Fig. 4.23**), due to the effects of spatially periodic boundary conditions.

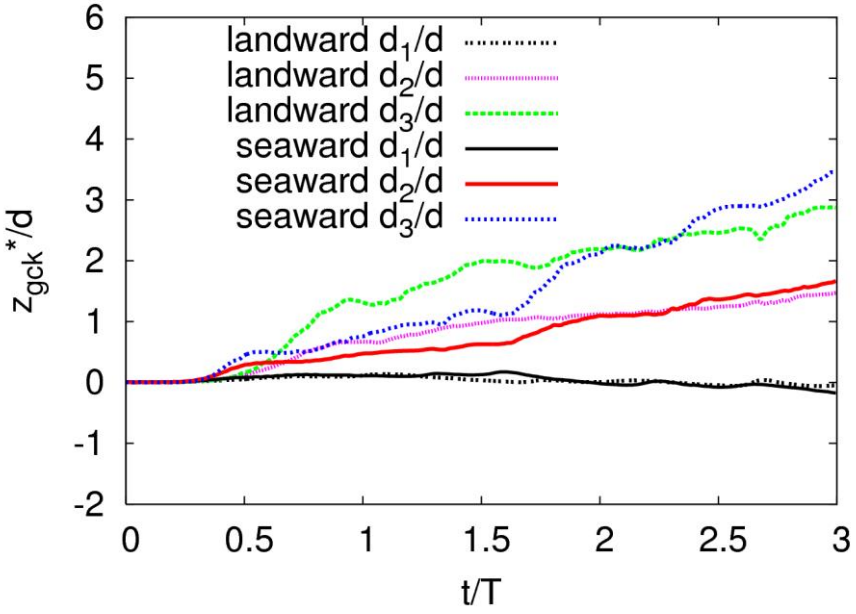

Figure 4.23 Comparisons of vertical centroids of concentration of particles between landward part and seaward area of Case 6.

4.5 Conclusions

3D numerical model of movable bed applied for mixed grain size sediments under sinusoidal oscillatory flow and progressive cnoidal wave. In order to understand the vertical sorting process of graded sands, which is essential for the sediment transport of mixed sands, five cases (with smaller Shield parameter, double period, double bottom layer thickness, slop bottom and a basic case for comparison) under symmetric oscillatory flow are performed. And another case under cnoidal wave is also conducted for the real condition.

The simulation results of Case 2 (smaller Shield parameter) and Case 1 indicate that the phenomenon of vertical sorting is more significant with larger Shield parameter. In Case 1 and Case 2 are quite similar. However, the snapshots show that the vertical sorting process comes early and the sorting process is more significant when Shield parameter is larger.

The concentration centroids of large and middle particles are lower while that of small particle is higher in Case 2, which confirms the above conclusion.

From the computational snapshots, in Case 3, where the period of oscillatory flow increases to double of Case 1, vertical sorting starts earlier. However, the concentration centroids of middle particles are higher than that of large particle after 1.5T, which shows that armor effect is not sufficiently working and middle particles become near suspension. The flow velocity U_m and Shields parameter for Case 3 and Case 1 are the same, while T increases to double of Case 1, the angular velocity becomes half. Hence the water particle semi-excursion increases and the drag force increase with the increase of Keulegan-Carpenter number. More momentum can be transferred from the fluid, sediment particles become more motive and as a result, the armoring effect breaks. The mean velocity profiles of particles show parabola mean velocity of middle particle reach to high position, which indicates the suspension of middle particle after armoring break. In the accelerating phase and at the maximum velocity phase of fully developed stage of grading, the distribution of particle number with all particles and the particle number with small and middle particles are quite similar, which means the vertical sorting failed due to the breaking of armoring effect.

When a sloping bottom is used for the simulation, the resultant centroids of concentration of particles, the mean velocity profiles of particles and the dimensionless particle number density distribution of Case 4 are quite similar to Case 1. However, the computational snapshot shows that large particles move much faster in the down-hill flow.

Armoring takes effect earlier in Case 5, where the thickness δ of sediments increases to double of Case 1. The bottom layer particles moves more slowly than the top layer particles in Case 5, hence the centroids of concentrations of large and middle particles are lower than that of Case 1 while the centroids of concentrations of small particles are higher than that of Case 1. The velocity distributions in Case 5 show significant upward convex

profile at all three phases.

For cnoidal wave, the vertical sorting proceeds until the wave crest passing by and fully develops in a complete period T. The concentration centroid of particles for overall width is, however, not uniform in wave progressing direction. The concentration centroid of large particles is higher landward within 2 periods.

CHAPTER 5

THE DRIFT BEHAVIOR OF DEBRIS WITH IRREGULAR SHAPE IN TSUNAMI

5.1 Introductions

The importance of tsunami evacuation tower, a facility used to protect the safety of life and property, is recognized especially after the Great East Japan Earthquake in 2011. A tsunami evacuation tower is usually constructed in plazas or parks with large parking place in the coastal land area, where involve dense population and automobiles but no upland nearby for people to evacuate in case of a tsunami inundation. However, large tsunami drifting debris, such as automobiles, always collides to the pillars of a tsunami evacuation tower and may cause damage to the tower in a tsunami flooding. Worse more, automobiles accumulate in front of the tsunami evacuation tower if the intervals between pillars are not long enough, and repeatedly collide, which may lead to blocking the tower. Hence, study on the movements of large drifts and their collisions to the tsunami evacuation tower becomes one of the key subjects in the design of tsunami evacuation tower.

Numbers of both physical experiments and numerical simulations have been done to study the drift behavior in tsunami run-up (Kumagai et al.; Tomita and Honda; Kawasaki et al and Nakamura et al.). However, most of these numerical models disregard the 3D interaction between fluid and large drift, only include the collisions between drift bodies or between drift and other structures.

In this chapter, laboratory experiments with 80 automobiles (made of Expanded polystyrene) colliding with both Bridge type of tsunami tower (with a large distance between pillars, short for B-type in the following paragraphs) and Conventional tsunami

tower (with beams between pillars, short for C-type) fixed in a hydraulic flume are carried out. Collision number and collision speed of automobiles together with the snapshots taken by high-speed camera are investigated in the experiments. For the numerical study, a 3D numerical model based on Lattice Boltzmann Method (LBM) is applied, and the interactions between fluid and drift, drift and drift can be solved by this method using a link-bounce-back scheme. The present numerical model is verified through the experimental data.

5.2 Hydrodynamic Experiments

5.2.1 Model set-up and experimental method

Using a length scale of 1:60, the hydraulic model experiment is carried out in 11,350×1,490mm concrete hydraulic flume. A distance of 7,488mm is set before the wave propagates to the automobiles. Totally 4 lines of automobiles (80×28×26mm), each line with 20 automobiles and each two lines with an interval of 90mm, are arranged 70mm in front of the tsunami evacuation tower. Other details of the experiment layout are shown in **Fig. 5.1**.

Figure 5.2 shows the dimensions of both B-type (488×88×150mm) and C-type (250×190×150mm) tsunami evacuation tower. B-type tsunami evacuation tower is constructed by 6 cylinder pillars, each of which has a circle section with diameter of 12mm; while C-type tsunami evacuation tower includes 12 cuboid pillars, each of which has a 10×10mm square section. The intervals between two adjacent pillars of B-type tower along the line perpendicular to the wave propagation direction are long enough for two abreast automobiles passing, while those of C-type tower is suitable for one automobile. Since the dimensions of these two tsunami evacuation towers are not identical, we will only focus on the behaviors of drift automobiles colliding against, blocking in front of or passing through the tsunami evacuation towers.

The specific gravity of model automobile is adjusted to 0.235 by installing a weight for the engine part in the front part (see **Fig. 5.3b**). This attachment gives a weight distribution of 60: 40 for front: rear. Tsunami flooding is generated by pumping water through an open gate in a hydraulic flume, and sponge is used to reduce turbulence. The experimental data are obtained from electromagnetic flow meter, capacity-type wave height meter and high-speed camera used for PIV. A discharge of 45*l/s* is applied and the corresponding maximum measured wave height is 3.3cm and average flow velocity is 30cm/s after noise reduction.

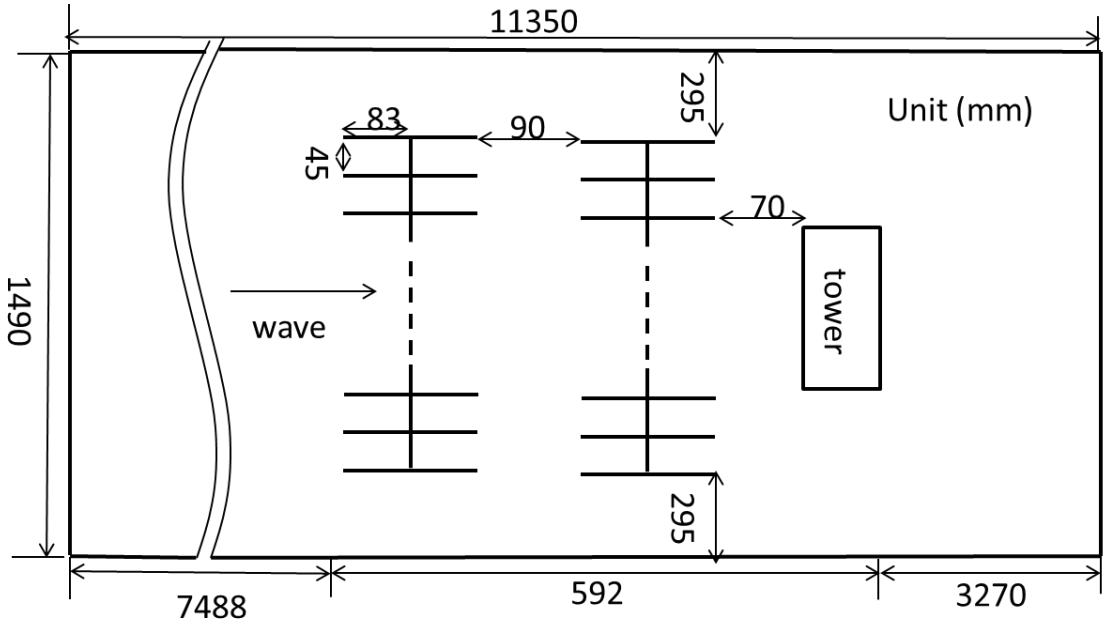

Figure 5.1 Layout of experimental set-up. (unit: mm)

(a) Photos of actual tsunami evacuation tower

(b) Photos of model tsunami evacuation tower

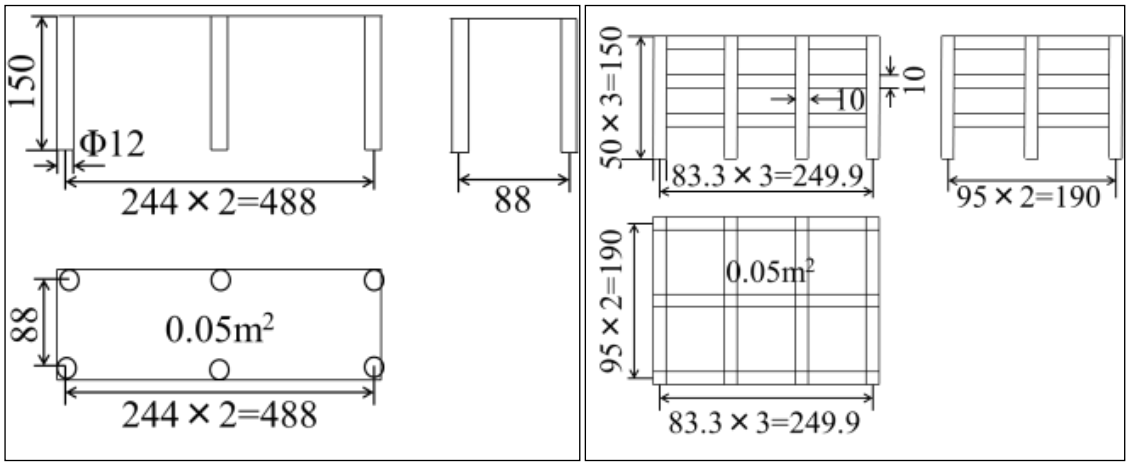

(c) Three orthographic views of tsunami evacuation tower (unit: mm)

Figure 5.2 B-type (left) and C-type (right) tsunami evacuation tower.

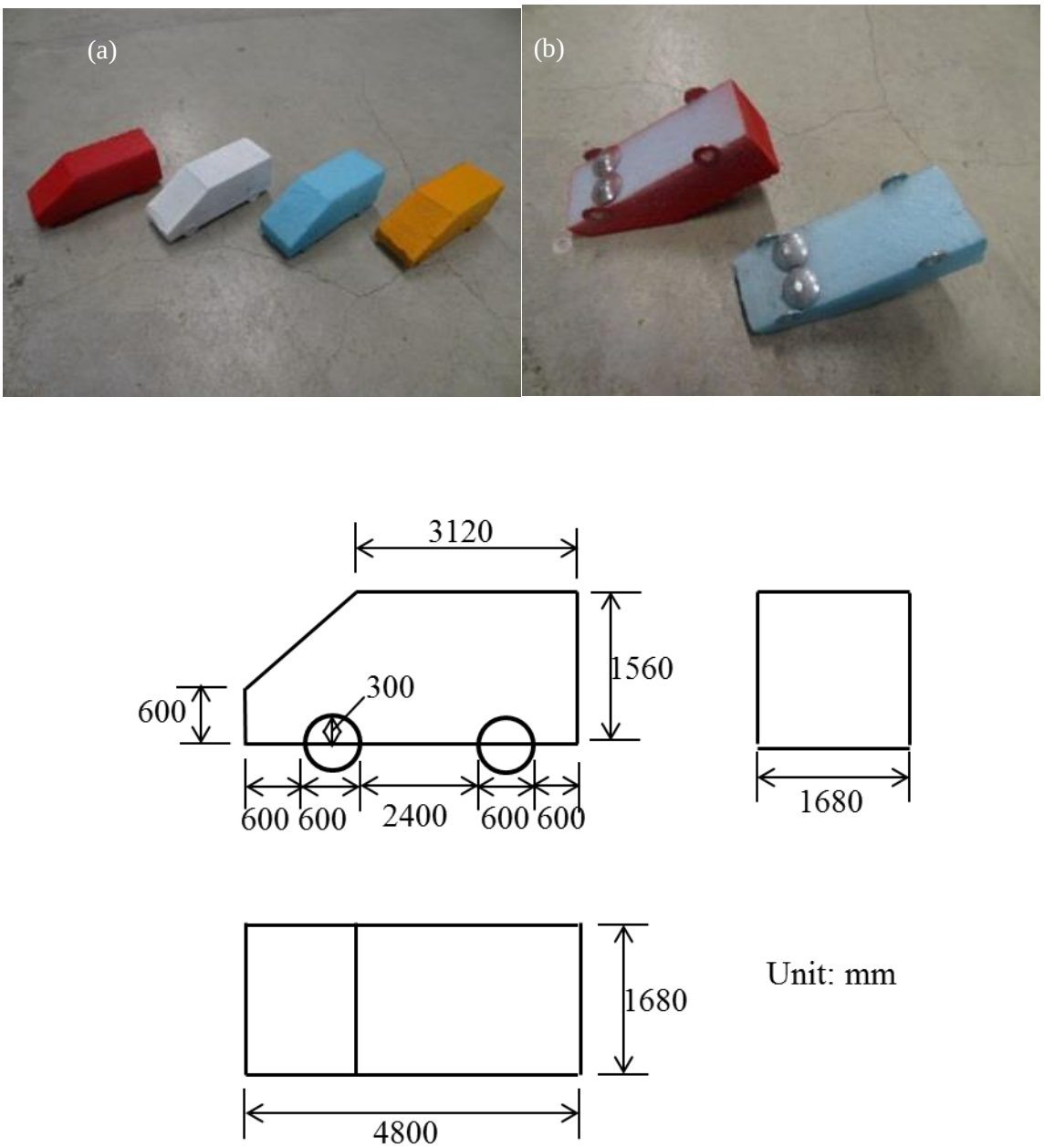

Figure 5.3 (a) top view, (b) bottom view and (c) three orthographic views of model automobiles.

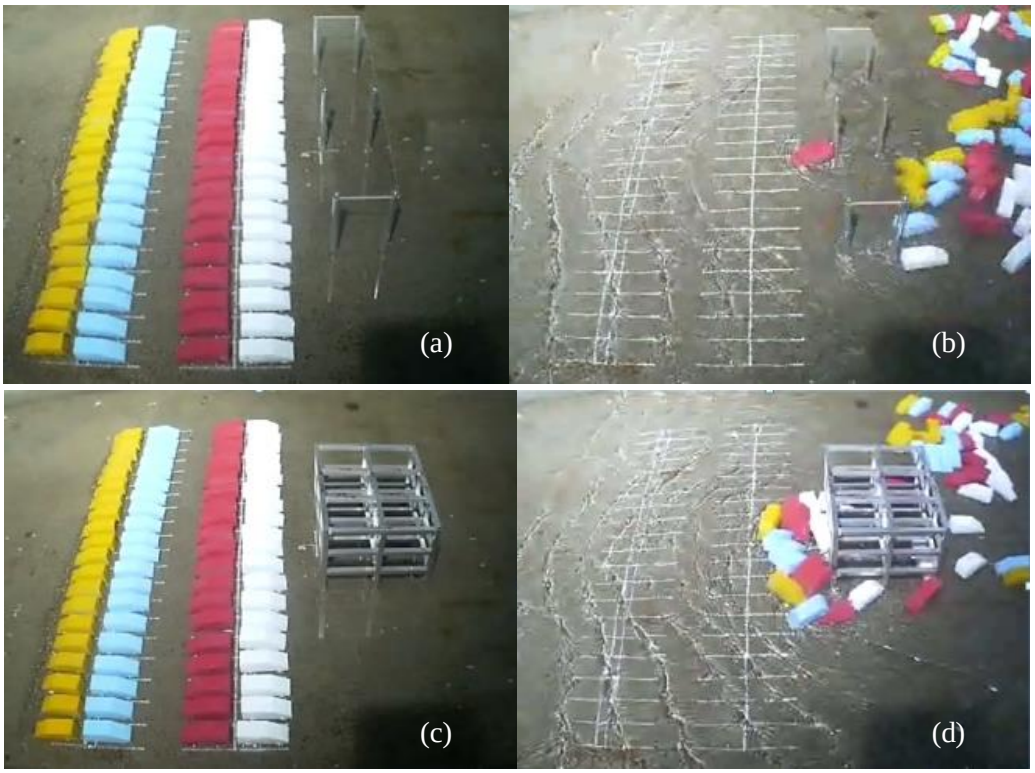

Figure 5.4 Snapshots of automobiles through B-type (b) and C-type (d) tsunami evacuation tower at the same time.

5.2.1 Collision number and collision speed

Figure 5.4 shows the snapshots of automobiles with 4 lines colored by yellow, blue, red and white and numbered Line 4 to Line 1, respectively. Namely, automobiles of Line 4 are located facing tsunami incoming current, while Line 1 is next to the tower. Set the time when the forefront wave propagates in front of automobiles of Line 1 (**Fig. 5.4a,c**) as 0s, then **Fig. 5.4b,d** show the snapshots of automobiles after 5.0s. More than 10 automobiles accumulated in front of C-type tsunami evacuation tower (**Fig. 5.4d**) due to the narrow distances between pillars. This implies when B-type is applied, collision frequency of automobiles to pillars is less as more automobiles can pass through, and when C-type is used, the drag force caused by tsunami increases as the active area (proportional to drag force) is larger. Hence less damage will be expected for B-type tower.

In order to know the characteristics of these two types of tsunami evacuation tower against automobile drifts, details of collision number and collision speed are listed from **Table 5.1** through **Table 5.4**. The collision number is calculated by the sum of the number of automobiles colliding with pillars, and the number of automobiles accumulated in front of the tsunami evacuation tower after collision. As a result, the collision number for B-type is less than C-type, especially for Line 2, where the number is reduced from 6 to 1. In the case of B-type tsunami evacuation tower, automobiles do not stay near the pillars after collision and are swept away by the ambient current, while in the case of C-type, automobiles of Line 1 remain in the vicinity of pillars after collision and accumulate automobiles of the other lines near the front tower.

Table 5.1 The collision number of automobiles for B-type tsunami evacuation tower.

	Left pillar	Mid pillar	Right pillar	Total
Line 1	2	2	1	5
Line 2	1	0	0	1
Line 3	1	0	1	2
Line 4	0	0	3	3
Total	4	2	5	11

Table 5.2 The collision number of automobiles for C-type tsunami evacuation tower.

	Pillars	Total
Line 1	No differences between pillars	7
Line 2		6
Line 3		2
Line 4		4
Total		19

Table 5.3 The magnitude of collision speed of automobiles for B-type tsunami evacuation tower (unit: cm/s).

	End pillar	Mid pillar	Average
Line 1	11.5	9.2	10.4
Line 2	10.6	16.0	13.3
Line 3	18.4	28.9	23.7
Line 4	26.3	26.7	26.5

Table 5.4 The magnitude of collision speed of automobiles for C-type tsunami evacuation tower (unit: cm/s).

	End pillar	Mid pillar	Average
Line 1	11.0	12.0	11.5
Line 2	16.2	16.3	16.3
Line 3	21.3	22.9	22.1
Line 4	25.0	20.7	22.9

Table 5.3 and **Table 5.4** list the collision speeds of automobiles (one random example for each Line), which are calculated from the snapshots taken by high speed camera, and defined as the moving distances of automobiles just before collision over the corresponding short time interval. Collision speed of one automobile in Line 4 is twice larger than that in Line 1, because the moving distance of automobile in Line 4 is considerably longer than that in Line 1. Based on the collision speed v given in **Table 5.3** and **Table 5.4**, the maximum collision force is calculated by $F=mv/\Delta t$=590kN, with a reference collision time of 0.01s[5].

5.2.3 Trajectories of the center of automobiles

Because of the symmetry, we only focus on the trajectories of automobiles laid in front of the right-hand side of tsunami evacuation tower. And for simplicity, only automobiles with odd numbers, namely the 1st, 3rd, 5th, 7th and 9th automobiles from the center of tsunami evacuation tower, are analyzed. The results are shown in **Fig. 5.5**. In the figure, the black solid circles and squares represent pillars of B-type and C-type respectively, and colors of green, red, blue and yellow are used to sign automobiles of Line 1 to Line 4 respectively. The wave propagates in the y-direction.

It can be seen in **Fig. 5.5a** and **Fig. 5.5b**, trajectories of automobiles far away from the center of tsunami evacuation tower (No.4 and No.5 of all lines) are similar in both B-type and C-type cases, while trajectories of automobiles for No.1 to No.3 of all lines are quite different in those two cases. Automobiles of Y1 (abbreviate for No.1 of Line4 colored by yellow), Y2, B1, B2 curve slightly to the right and then drift straightly through B-type tsunami evacuation tower, while automobiles of R1, R2, B1, B2, Y1, Y2, Y3 bend significantly to the right and bypass C-type tsunami evacuation tower. For the case of B-type, automobiles drift through the tsunami evacuation tower immediately after colliding with its pillars. However, for the case of C-type, automobiles of Line 1 accumulate in front of tsunami tower after colliding with its pillars and cause the following automobiles dammed one after another. As a result, the flow field changes, and the automobiles appear to significantly drift.

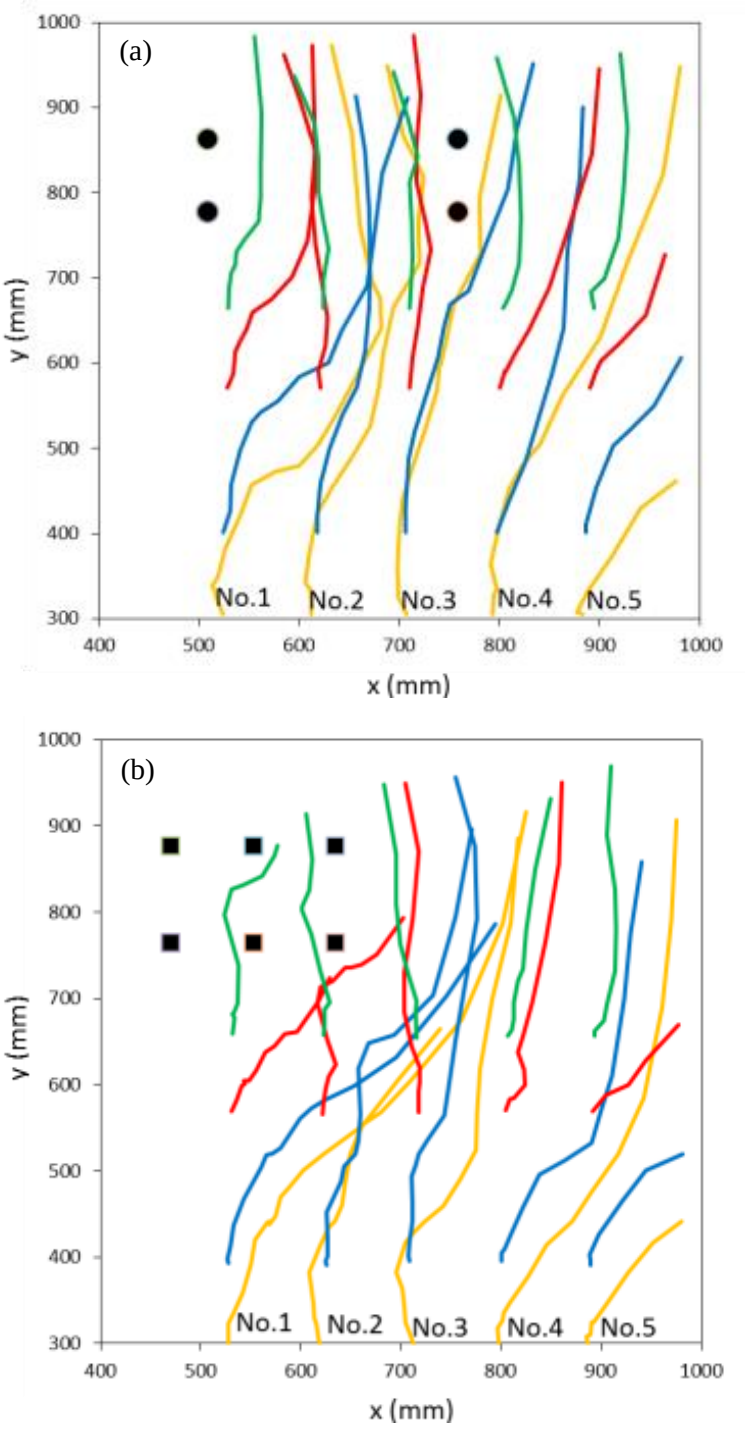

Figure 5.5 Trajectories of the center of automobiles through B-type (a) and C-type (b) of tsunami evacuation tower. (Yamauchi, 2014)

5.3 Simulation Results

A typical initialized automobile is constructed with 6,550 solid nodes, 2,160 surface solid nodes which are adjacent to fluid nodes. The inertia momentums of the automobiles are approximated to an 80×28×26mm polyhedron as shown in **Fig. 5.6**. The submerged volume for the calculation of buoyance force is simplified to a pyramid when only a corner of the automobile is submerged (**Fig. 5.7a**), but once one whole edge of the automobile is submerged, the volume is calculated with the length of the edge by its perpendicular submerged surface area of the automobile (**Fig. 5.7b**).

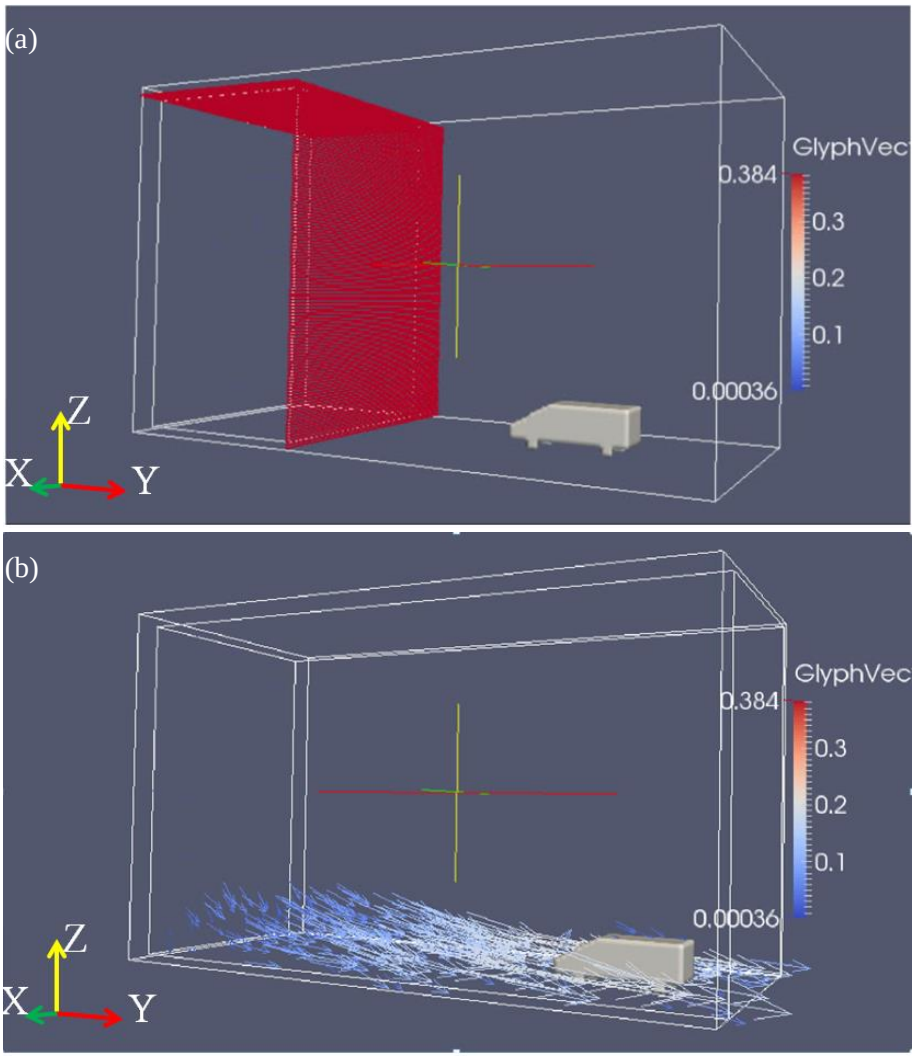

Figure 5.6 (a) Initial setup of automobile and dam-break flow; (b) snapshot of movable automobile.

A series of numerical simulations has been performed to investigate the collision speed of automobiles to tsunami evacuation tower by the change of submerged water depths and flow velocities.

In order to save computation time, a small computation domain of 400×120×60mm is applied. With this limited computation domain, tsunami flooding current is generated by a dam-break in front of the automobiles (**Fig. 5.6**). No-slip boundary condition, periodic boundary condition, transmission boundary condition and free surface boundary condition are used for the bottom, front and back, right and top sides respectively.

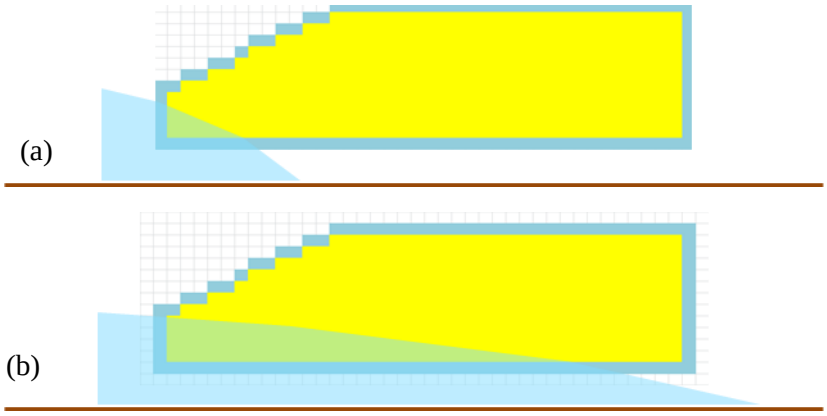

Figure 5.7 Schematic graph of the calculation method for buoyance force when only (a) a corner of the automobiles is submerged and (b) one whole edge of automobile is submerged.

Figure 5.8 shows the behavior of partly submerged 3 drifting automobiles near the front pillar. **Figure 5.8a** shows the initial position of all the automobiles and the pillar. Distances between the center of automobiles and the pillar are the same to the hydraulic experiment. At early stage, the red and yellow automobiles drift with a slight declination to the y-direction while the green automobile remains straightly along the y-direction. After 0.2s, the front part of the red automobile is totally submerged in the tsunami flooding current (**Fig. 5.8b**). Momentums from current flows are transported to the red automobile and

make it drifting. As the simulation goes on, all three automobiles are submerged in the flooding current. The red automobile drifts to the front part of the yellow automobile, collides against it. After several collisions between the red automobile and the yellow automobile, at the time period of 2.3s, the red automobile sinks while the yellow and green ones float (**Fig. 5.8c**).

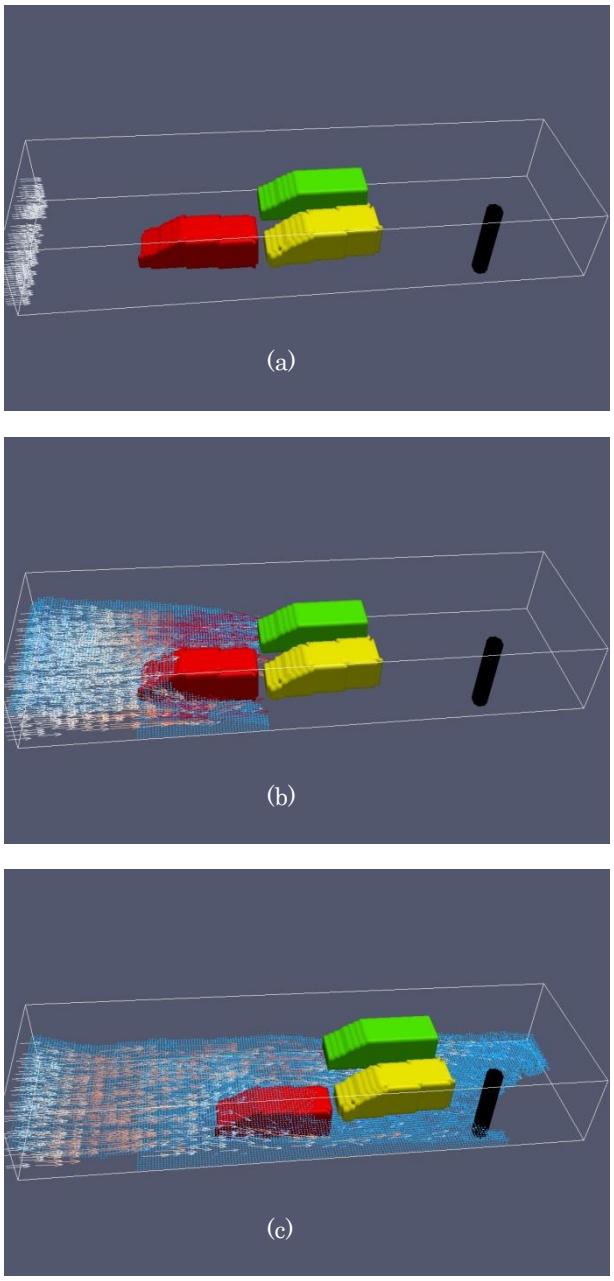

Figure 5.8 Behaviors of drift automobiles in tsunami at (a) initial, and after (b) 0.2s and (c) 2.3s.

With the same simulation condition but a relatively larger computation domain of 140×1700×60mm, the behavior of 8 drifting automobiles are simulated. **Figure 5.9** shows the behavior of partly submerged 8 drifting automobiles in front of two pillars located in the center of C-type tsunami evacuation tower. **Figure 5.9a** shows the initial position of the automobiles and pillars. Distances between the center of automobiles and the pillar are the same with the hydraulic experiment. The blue and white automobiles are set oppositely to the yellow and red ones, as in the experiment.

After 0.17s, tsunami flooding current flows to the front of the yellow automobiles (**Fig. 5.9b**), which are then drifted by it and collide to the blue automobiles. Momentum from current flow is transferred to the blue automobiles and makes them drifting together (**Fig. 5.9c**). As the simulation goes on, all 8 automobiles are submerged in and drifted by the flooding current. These drifted automobiles collide with each other, and at the time period of 1.3s, the white and red automobiles bypassed the two pillars (**Fig. 5.9d**). All these automobiles drift to the pillars in y-direction but against the pillar in x-direction (perpendicular to the wave propagating direction), and have a tendency of bypassing the pillar (**Fig. 5.10**), which is very similar to the experimental results.

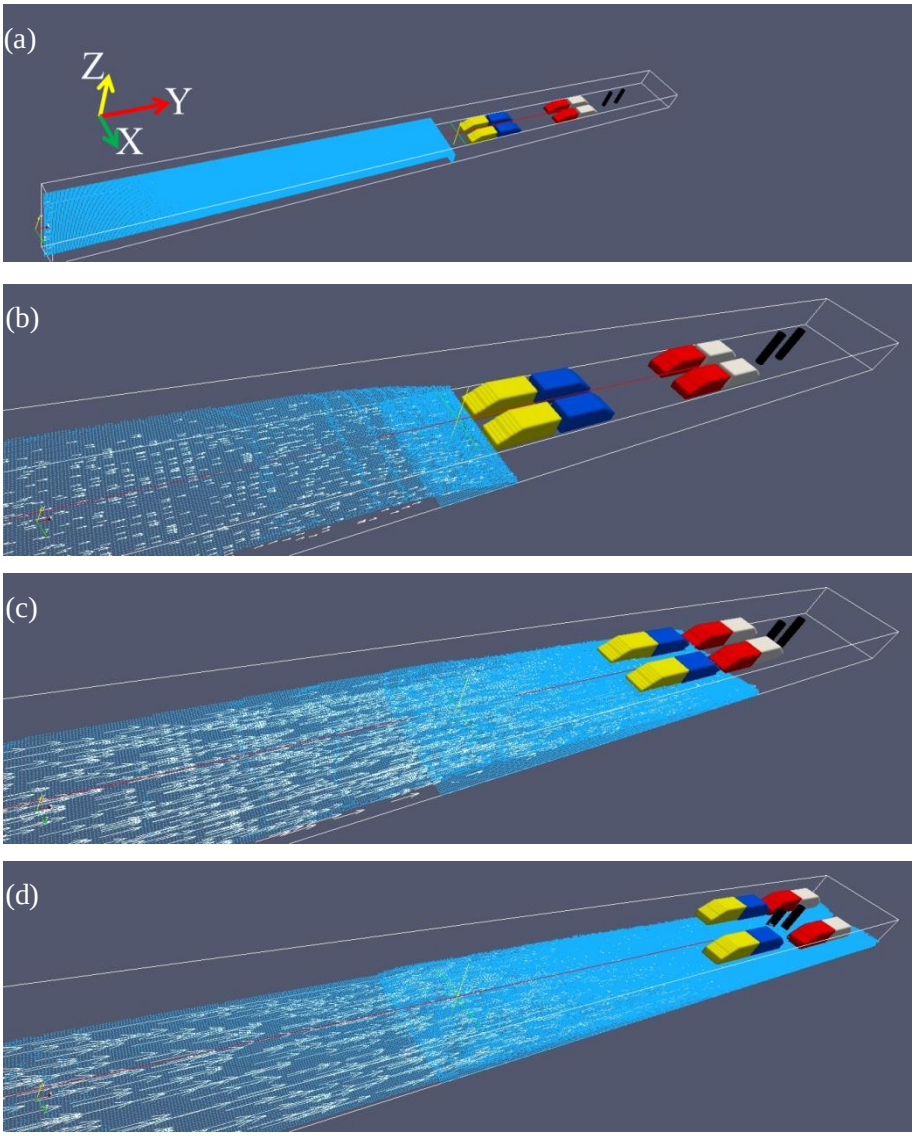

Figure 5.9 Behaviors of drift automobiles in tsunami at (a) initial, and after (b) 0.17s, (c) 0.82s and (d) 1.30s.

Trajectories of the center of the simulated automobiles indicate that most of these automobiles do not move straightly along y-direction, but zigzag slightly at the beginning and bend with a relative significant angle near the pillars. The collision speed increases with the increase of submerged water depths and flow velocities, which cause the increment of the collision force due to automobiles.

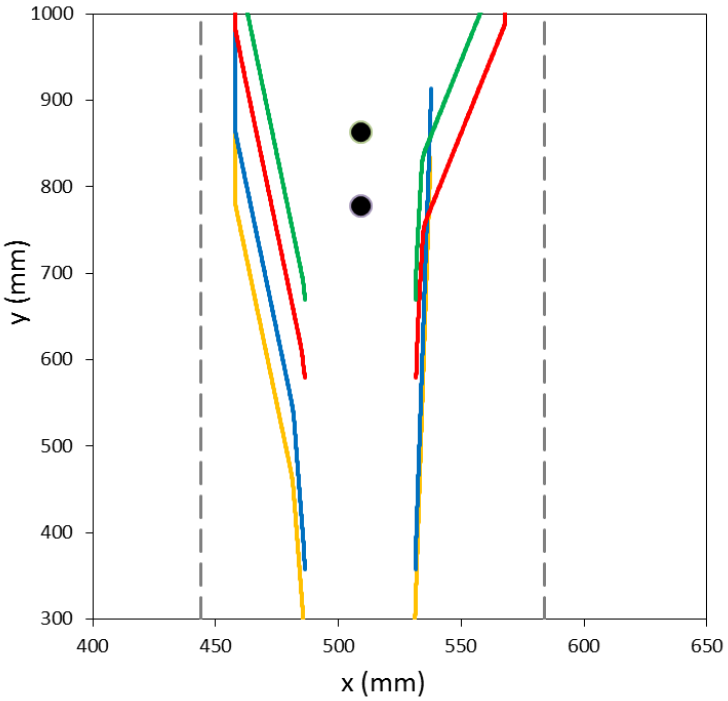

Figure 5.10 Simulated trajectories of the center of each automobile.

5.4 Conclusions

3D movable bed model is modified to study the behavior of tsunami drifted automobiles with irregular shapes. In order to verify the model, experiments of 80 automobiles collide to the pillars of B-type and C-type tsunami evacuation towers are conducted.

Study on the behaviors of tsunami drifted automobile debris is necessary in the design of tsunami evacuation tower, because automobile debris drifting in the tsunami current can block towers and cause damage to it. Based on this conception, hydraulic experiments of 80 automobiles collide against both B-type and C-type tsunami evacuation towers are carried out. The results show B-type tsunami evacuation tower is more effective. Larger distances between pillars make more automobiles passing through and as a result, less collision between automobiles and automobiles against towers occur, also the drag force caused by the tsunami flooding current decreases due to the less active area when few automobiles block tsunami evacuation towers.

Besides physical experiments, numerical experiments are conducted by using a 3D LBM model for particle suspension, modified for irregular particle shape and extended with free surface part and SGS turbulence term. Tsunami flooding currents in the simulation are generated by the dam break flows. The submerged volume for the calculation of buoyance force is simplified to a pyramid when only a corner of the automobile is submerged, but once one whole edge of the automobile is submerged, the volume is calculated with the length of the edge by its perpendicular submerged surface area of the automobile.

A series of numerical simulations has been performed. The behavior of partly submerged 3 drifting automobiles, two of which have slight declinations to the y-direction, collide with one pillar are simulated. Momentums from current flows are transported to the automobiles and make it drifting. As the simulation goes on, all three automobiles are submerged in the

flooding current. And after several collisions between automobiles, the one automobile sinks while the others float.

Then a relatively complicated case of 8 drifting automobiles with two pillars located in the center of C-type tsunami evacuation tower are performed. Similar phenomenon can be observed in this case. After 0.17s, tsunami flooding current flows to the front of the yellow automobiles, which are then drifted by it and collide to the blue automobiles. Momentum from current flow is transferred to the blue automobiles and makes them drifting together. As the simulation goes on, all 8 automobiles are submerged in and drifted by the flooding current. These drifted automobiles collide with each other, and at the time period of 1.3s, the white and red automobiles bypassed the two pillars.

And the trajectories of the center of drift automobiles show that all these automobiles drift to the pillars in y-direction but against the pillar in x-direction (perpendicular to the wave propagating direction), and have a tendency of bypassing the pillar, which is very similar to the experimental results.

CHAPTER 6

CONCLUSIONS

A 3D movable bed model based on LBM is established with expansion to free surface condition and SGS turbulence model. This gas-fluid-solid model identifies fluid-gas interaction by applying a fluid fraction ε, and deals the fluid-solid interaction and solid-solid interaction by using a link-bounce-back scheme. This model was first used to simulate sediment transport of uniform-grain-size sediments and mixed-grain-size sediments with sphere shapes, and then to study the behavior of drifting automobiles with irregular shapes. Based on this, sediments with irregular shape can be simulated with the present model.

The 3D movable bed model based on LBM is developed to study the particle movements of uniform grain size sediments of bed-load layer under open channel flow in sheetflow regime. In the present LBM model, any semi-empirical coefficient is not needed as an input data, but only the cut-off of lubrication approximation, the additional offset in computing fluid fraction, together with the Smagorinsky Constant in turbulent model are required. This model can be extended relatively easily to 3D movable bed in large scale, because the LBM process involves an algorithm suitable for parallel computation.

This model has been successfully applied to study the uniform grain size sediments under open channel flows, mixed grain size sediments under oscillatory flows and progressive waves, and submerged tsunami drifts in tsunami flooding currents.

6.1 Uniform Sands under Open Channel Flows

In order to know more about the behavior of uniform bed-load sediments, a series of cases are carried out with different Shield parameter ranged between 0.01 and 0.42, with a constant water depth of 8.3 cm. For the model's validation, the horizontal movement velocity of sediment particles and the vertical existing probability density distribution of sediment particles are compared with the experimental data of Gotoh et al. (1993, 1994). The results show that the simulation results of the present model agrees fairly well with their experimental data.

The time series of flow velocity field in the longitudinal section show that at the beginning, the flow velocity is unstable with a tangential flow velocity due to pressure gradient and after around $t' = 2.0$, the flow velocity field becomes stable.

2D longitudinal profiles of the movements of sediment particles with $\tau^*=0.025$, $\tau^*=0.10$ and $\tau^*=0.18$ show that: (1) when Shields parameter is small, particles move very slowly with sliding and rolling, and small saltation occurs in the surface layer. (2) With the increase of Shields parameter, sediment particles move faster and jump higher, and saltation becomes significant. (3) Sheetflow occurs when Shields parameter increases to 0.1, and becomes more significantly pronounced when $\tau^*=0.18$.

The trajectories of 5 individual particles show that: (1) when the Shields parameter is small ($\tau^*=0.025$), sediment particles at the top of bed-load layer move with a small saltation besides sliding and rolling, while sediment particles in the middle layer move with sliding and rolling. The collisions among particles induce 3D spiral trajectories. (2) With the increase of τ^*, particles in the intermediate layer becomes more motive in the vertical direction. (3) When $\tau^*=0.18$, sheetflow occurs in the bed-load layer. (4) With the increase of τ^*, the movement of particles in the bed-load layer becomes 2D sheetflow, and the particle trajectories can be drawn in the 2D plane as the saltation distance becomes longer.

The horizontal velocity distributions of sediment particles show that the horizontal velocity of the top bed-load layer does not increase monotonously, but increases in a complicated distribution with several inflection points in all cases except the case of τ*=0.06. This phenomenon is quite similar to the results of Gotoh (1993), where larger arc-shaped saltation occurs due to the repeated collisions between particles in the intermediate layer.
The results of vertical existing P.D.F. of sediment particles show that the distribution of vertical existing P.D.F is asymmetry and the width of the peak of P.D.F increases with the increase of Shields parameter. The position of the peak of P.D.F becomes lower with the increase of Shields parameter but it is almost fixed when τ*>0.2.

6.2 Mixed Sands under Oscillatory Flows and Progressive Wave

3D numerical model of movable bed applied for mixed grain size sediments under sinusoidal oscillatory flow and progressive cnoidal wave. In order to understand the vertical sorting process of graded sands, which is essential for the sediment transport of mixed sands, five cases (with smaller Shield parameter, double period, double bottom layer thickness, slop bottom and a basic case for comparison) under symmetric oscillatory flow are performed. And another case under cnoidal wave is also conducted for the real condition.

The phenomenon of vertical sorting is more significant with larger Shield parameter. When a sloping bottom is used for the simulation, the resultant centroids of concentration of particles are quite similar to the case with flat bottom. However, large particles move much faster in the down-hill flow. When the period of oscillatory flow increases to double, vertical sorting starts earlier. However, after 1.5T, armor effect is not sufficiently working and middle particles become near suspension. The flow velocity U_m and Shields parameter for case with double period T=2s and case with T=1s are the same, while T increases to double, the angular velocity ω becomes half. Hence the water particle semi-excursion A (in

the function $U_m=A\omega$) increases, and the drag force increase with the increase of Keulegan-Carpenter number. More momentum can be transferred from the fluid, sediment particles become more motive and as a result, the armoring effect breaks.

Armoring takes effect earlier in the case, where the thickness δ of sediments increases to double. The bottom layer particles moves more slowly than the top layer particles in the case with double layer thickness, hence the centroids of concentrations of large and middle particles are lower than that of the case with smaller layer thickness while the centroids of concentrations of small particles are higher than that of the case with smaller layer thickness.

For cnoidal wave, the vertical sorting proceeds until the wave crest passing by and fully develops in a complete period *T*. The concentration centroid of particles for overall width is, however, not uniform in wave progressing direction. The concentration centroid of large particles is higher landward within 2 periods.

6.3 Submerged Drift Automobiles under Tsunami Flooding Currents

3D movable bed model is modified to study the behavior of tsunami drifted automobiles with irregular shapes. In order to verify the model, experiments of 80 automobiles collide to the pillars of B-type and C-type tsunami evacuation towers are conducted.

Study on the behaviors of tsunami drifted automobile debris is necessary in the design of tsunami evacuation tower, because automobile debris drifting in the tsunami current can block towers and cause damage to it. Based on this conception, hydraulic experiments of 80 automobiles collide against both B-type and C-type tsunami evacuation towers are carried out. The results show B-type tsunami evacuation tower is more effective.

Larger distances between pillars make more automobiles passing through and as a result, less collision between automobiles and automobiles against towers occur, also the drag force caused by the tsunami flooding current decreases due to the less active area when few automobiles block tsunami evacuation towers.

Besides physical experiments, numerical experiments are conducted by using a 3D LBM model for particle suspension, modified for irregular particle shape and extended with free surface part and SGS turbulence term. Tsunami flooding currents in the simulation are generated by the dam break flows. The submerged volume for the calculation of buoyance force is simplified to a pyramid when only a corner of the automobile is submerged, but once one whole edge of the automobile is submerged, the volume is calculated with the length of the edge by its perpendicular submerged surface area of the automobile.

A series of numerical simulations has been performed. Momentums from current flows are transferred to the automobiles and make it drifting. As the simulation goes on, all automobiles are submerged in the flooding current. These drifted automobiles collide with each other, and finally, the front automobiles bypassed the pillars.

And the trajectories of the center of drift automobiles show that all these automobiles drift to the pillars in y-direction but against the pillar in x-direction (perpendicular to the wave propagating direction), and have a tendency of bypassing the pillar, which is very similar to the experimental results.

References

Ahmed, A. S. M. and Sato, S., 2003a. A sheetflow transport model for asymmetric oscillatory flows. Part I: Uniform grain size sediments. *Coastal Engineering Journal*, Vol. 45, No.3, pp. 321-337.

Ahmed, A. S. M. and Sato, S., 2003b. A sheetflow transport model for asymmetric oscillatory flows. Part II: Mixed grain size sediments. *Coastal Engineering Journal*, Vol. 45, No.3, pp. 339-361.

Aidun, C. K., Lu, Y. and Ding, E.-J., 1998. Direct analysis of particulate suspensions with inertia using the discrete Boltzmann equation, J. Fluid Mech., 373, pp.287-311.

Al-Salem, A. A., 1993. Sediment transport in oscillatory boundary layers under sheet-flow conditions. Doctoral dissertation, Delft University of Technology.

Bhatnagar, P.L., Gross, E.P. and Krook, M., 1954. A model for collision processes in gases. I. Small amplitude processes in charged and neutral one-component systems. *Physical Review*, Vol. 94, No. 3, pp. 511-525.

Campbell, L., McEwan, I., Nikora, V.,, Pokrajac, D., Gallagher, M. and Manes, C., 2005. Bed-load effects on hydrodynamics of rough-bed open-channel flows. *Journal of Hydraulic Engineering*, Vol. 131, pp. 576-585.

Chen, H., Chen, S. and Matthaeus, W.H., 1992. Recovery of the Navier-Stokes equations using a lattice-gas Boltzmann method. *Physical Review A*, Vol. 45, No. 8, pp. 5339-5342.

Dibajnia, M. and Watanabe, A., 2000. Moving layer thickness and transport rate of graded sand. *Coastal Eng. Proc.*, pp. 2752-2765.

Dong, P. and Zhang, K., 1999. Two-phase flow modelling of sediment motions in oscillatory sheet flow. *Coastal Engi.*, Vol. 36, pp. 87-109.

Einstein, H. A., 1950. The bed-load function for sediment transportation in open channel flows, *Technical Bulletin*, No. 1026, pp.32.

Feng Y.T., Han K. and Owen D.R.J., 2010. Combined three-dimensional lattice Boltzmann method

and discrete element method for modelling fluid-particle interactions with experimental assessment. *Int. J. Numer. Meth. Eng.*, Vol. 81, pp. 229-245.

Feng Z.-G. and Michaelides, E. E., 2003. Fluid-particle interactions and resuspension in simple shear flow. *J. Hydraul. Eng.*, Vol. 129, pp. 985-994.

Frisch, U., d'Humieres, D., Hasslacher, B., Lallemand, P., Pomeau, Y. And Rivet, J.-P., 1987. Lattice gas hydrodynamics in two and three dimensions. *Complex systems*, Vol. 1, No. 4, pp. 649-707.

Fukuda T., Fukuoka S. and Uchida T., 2013. Three-dimensional gravel motions in numerical movable bed channel with particles of various shapes and sizes. *Advances in River Sediment Research*, pp. 323-332.

Gotoh H., Harada E. and Sakai T., 2001a. Vertical sorting of graded sediment transport under oscillatory flow. *J. JSCE*, No. 691/ II-57, pp. 133-142. (in Japanese)

Gotoh H., Harada E. and Sakai T., 2001b. Optimization of parameters in DEM-based numerical movable bed simulator. *J. JSCE*, No. 691/ II-57, pp. 159-164. (in Japanese)

Gotoh H., Harada E. and Sakai T., 2002. Numerical Simulation of vertical sorting process in sheetflow regime by using 3D granular simulator. *Journal of JSCE*, Vol. 49, pp. 471-475. (in Japanese)

Gotoh, H. and Sakai, T., 1997. Numerical simulation of sheetflow as granular material, *J. Waterway, Port, Coastal and Ocean Eng.*, Vol. 123, pp. 329-336.

Gotoh, H., Sakai, T., Toyota, Y. and Tada, T., 1996. Vertical grading mechanisms of mixed grain size sediments under oscillatory flows. *Journal of JSCE*, Vol. 43, pp.456-460. (in Japanese)

Gotoh H., Tsujimoto T. and Nakagawa H., 1993. The moving characteristics of sediment particles: the transition process from saltation to sheetflow. *Journal of JSCE*, Vol. 40, pp. 326-330. (in Japanese)

Gotoh H., Tsujimoto T. and Nakagawa H., 1994. Numerical analysis of bed-load layer as solid/liquid two-phase flow. *Journal of JSCE*, Vol. 485 No. II-26, pp. 11-19. (in Japanese)

Gotoh, H., Yeganeh-Bakhtiary A. and Sakai T, 2000. Coupling of multiphase-flow model and distinct element method for simulation of sediment transport under high bottom shear, *Journal of JSCE*, No. 649/ II-51, pp. 17-26.(in Japanese)

Hanson, H., Brampton, A., Capobianco, M., Dette, H.H., Hamm, C.L., Lechuga, A., Spanhoff, R., 2002. Beach nourishment projects, practices, and objectives—a European overview. *Coastal Engineering*, Vol. 47, No. 2, pp. 81-111.

Harada E. And Gotoh H., 2006. Numerical simulation of sediment sorting in sheetflow regime by 3D granular material model. *Journal of JSCE, B*, Vol. 62, No. 1, pp. 128-138. (in Japanese)

Harada E. And Gotoh H., 2007. Numerical simulation of vertical sorting in sheetflow sediment transport by two-phase turbulent flow model, *Journal of JSCE, B2*, Vol. 54, pp. 476-480. (in Japanese)

Harada E. And Gotoh H., 2008. Computational mechanics of vertical sorting of sediment in sheetflow regime by 3D granular material model. *Coastal Engineering Journal*, Vol. 50, No. 1 pp. 19-45.

Harada, E., Gotoh, H. and Tsuruta, N., 2010. Numerical simulation of vertical sorting in sheetflow regime by 3D solid-liquid two-phase turbulent flow model. *Journal of JSCE, B2*, Vol. 66, No.1, pp. 411-415. (in Japanese)

Harada, E., Tsuruta, N. and Gotoh, H., 2011. Large eddy simulation for vertical sorting processes in sheet-flow regime. *Journal of JSCE, B2*, Vol. 67, No.2, pp. I_471-I_475. (in Japanese)

Harada, E., Yeganeh-Bakhtiary A., Gotoh, H. and Sakai, T., 2000. Numerical simulation on sediment sorting in sheetflow regime by granular model. *Journal of JSCE*, Vol. 47, pp. 491-495. (in Japanese)

Hassan, W. N. and Ribberink, J. S., 2005. Transport processes of uniform and mixed sands in oscillatory sheet flow. *Coastal Engineering*, Vol. 52, pp. 745-770.

He, L., Okajima, M., Kioka W. and Kitano T., 2013. Modelling 3D numerical movable bed based on LBM and its application to the analysis of bed-load layer. *Journal of JSCE*, B2, Vol. 69, No.2, pp. I_546-I_550. (in Japanese)

Hus, T.-J., Jenkins, J. T. and Liu, P. L.-F., 2004. On two-phase sediment transport: sheet flow of massive particles. *Proc. R. Soc. Lond. A*, Vol. 460, pp. 2223-2250.

Inamuro, T., Ogata, T., Tajima, S., Konishi, N., 2004. A lattice Boltzmann method for incompressible two-phase flows with large density differences. *Journal of Computational Physics*, Vol. 198, pp. 628-644.

Kawasaki, K., Takusu, Y. and Ut, H. D., 2010. 2-D numerical wave flume with solid-gas-liquid interaction and its application. *Coastal Engineering Proceeding*, Vol. 32, No. 1.

Körner, C., Pohl, T., Rüde, U., Thürey, N. and Zeiser, T., 2005. Parallel lattice Boltzmann methods for CFD applications. In: A. Bruaset, A. Tveito (eds.) *Numerical Solution of Partial Differential Equations on Parallel Computers*, 51 of LNCSE, pp.439-465.

Kuang, C.P., Pan, Y., He, L.L., Yang, Y.X., Cai, F., 2011. Beach nourishment projects in China. *Proceedings of the Sixth International Conference on Asian and Pacific Coasts* (Hong Kong, China), pp. 147-161.

Kumagai, K., Oda, K. and Fujii, N., 2006. Applicability of simulation model for drift behavior of containers due to tsunami. *Proc. of Techno-Ocean 2006/ 19th JASNAOE Ocean Engineering Symposium*, No. 72.

Ladd, A.J.C., 1994a. Numerical simulations of particulate suspensions via a discretized Boltzmann equation. Part 1. Theoretical foundation. *J. Fluid Mech.*, Vol. 271, pp. 285-310.

Ladd, A.J.C., 1994b. Numerical simulations of particulate suspensions via a discretized Boltzmann equation. Part 2. Numerical results. *J. Fluid Mech.*, Vol. 271, pp. 311-339.

Ladd, A.J.C. and Verberg, R., 2001. Lattice-Boltzmann simulations of particle-fluid suspensions. *Journal of statistical physics*, Vol. 104, pp. 1191-1251.

Lockard, D.P., Luo, L.S., Singer, B.A., 2000. Evaluation of the Lattice-Boltzmann equation solver PowerFLOW for aerodynamic application. *Technical Report*, NASA/CR-2000-210550, ICASE Report No. 2000-40.

McNamara, G.R. and Zanetti, G., 1988. Use of the Boltzmann Equation to simulate Lattice-Gas Automata. *Physical Review Letters*, Vol. 61, No. 20, pp. 2332-2335.

Meyer-Peter, E. and Müller, R., 1948. Formulas for bed-load transport. *Proc. 2nd Meeting*, Intern. Assoc. Hyd. Res., Vol.6, pp. 39-64.

Nakamura, T., Mizutani, N. and Wakamatsu, Y., 2012. Study on drift behavior of container on apron due to tsunami-induced incoming and return flow. *Coastal Engineering Proceeding*, Vol.33, No. 1.

National Police Agency of Japan Emergency Disaster Countermeasures Headquarters, 2014. Damage situation and police countermeasures associated with 2011 Tohoku district – off the Pacific Ocean Earthquake.

Nguyen N.-Q. and Ladd A.J.C., 2002. Lubrication corrections for lattice-Boltzmann simulations of particle suspensions. *Physical review E*. Vol. 66, 046708.

Nielsen, P., 2009. *Coastal and Estuarine Processes*. World Scientific Publishing Co. Pte. Ltd., Advanced series on ocean engineering, vol. 29, pp. 207.

Okajima, M., 2013. Modeling Noncohesive Sediment Suspension and Transport. Master's Thesis, Nagoya Institute of Technology. (in Japanese)

Qian, Y.H., d'Humieres D. and Lallemand P., 1992. Lattice BGK models for Navier-Stokes equations. *Europhysics Letters*, Vol. 17, No. 6, pp. 479-484.

Ribberink J.S., 1998. Bed-load transport for steady flows and unsteady oscillatory flows. *Coastal Engineering*, Vol. 34, pp. 59-82.

Sakai T., Gotoh H. Oki K. and Takahashi T., 2000. Vertical grading of mixed-size grains in sheetflow regime under oscillatory flow. *Proceeding of Coastal Engineering*, Vol. 32, No. 1, pp. 2766-2779.

Shan, X., and Chen, H., 1996. Lattice Boltzmann model for simulating flows with multiple phases and components. *Physical Review E*, Vol. 47, No. 3, pp.1815-1819.

Smagorinsky J., 1958. On the numerical integration of the primitive equations of motion for baroclinic flow in a closed region. *Monthly Weather Review*, Vol. 86 No. 12, pp. 457-466.

Smagorinsky J., 1963. General circulation experiments with the primitive equations. I. The basic experiments. *Monthly Weather Review*, Vol. 91 No. 3, pp. 99-164.

Small, C. and Cohen, J. E., 2004. Continental physiography, climate, and the global distribution of human population. *Current Anthropology*, Vol. 45, No. 2, report.

Sumori, 2014. Numerical simulation on the mechanism of suspended sediment transports. Master's Thesis, Nagoya Institute of Technology. (in Japanese)

Swift, M.R., Orlandini, E., Osborn, W.R. and Yeomans, J.M., 1996. Lattice Boltzmann simulations of liquid-gas and binary fluid systems. *Physical Review E*, Vol. 54, No. 5, pp. 5041-5052.

Thaxton C. S. and Calantoni J., 2006. Vertical sorting and preferential transport in sheet flow with bimodal size distributions of sediment. *Coastal Engineering Proceeding*, Vol. 30, No.1.

Thürey, N., 2007. Physically based animation of free surface flows with the lattice Boltzmann

method. Master's thesis, technical faculty of University of Erlangen-Nuremberg, Germany, pp. 11.

Thürey, N. and Rüde, U., 2009. Stable free surface flows with the lattice Boltzmann method on adaptively coarsened grids. *Computing and Visualization in Science*, Vol.12, No.5, pp. 247-263.

Tomita, T. and Honda, K., 2010 Practical model to estimate drift motion of vessels by tsunami with consideration of colliding with structures and stranding. *Coastal Engineering Proceeding*, Vol.32, No.1.

Uda, T., 2010. *Japan's Beach Erosion: Reality and Future Measures*. Singapore: World Scientific Publishing Co. Pte. Ltd., pp. 3.

U.S. Army Corps of Engineers (USACE), 1984. *Shore Protection Manual*. Vicksburg, Mississippi: U.S. Army Corps of Engineers, Coastal Engineering Research Center, pp. 1-3.

Van der Salm, J. and Unal, O., 2003. Towards, a common Mediterranean framework for beach nourishment projects. *Journal of Coastal Conservation*, Vol. 9, pp. 35-42.

Van Rijn, L.C., 1984. Sediment transport, Part 1: bed load transport. *J. Hydraul. Eng.*, Vol. 110, pp. 1431-1456.

Van Rijn, L.C., 1987. Mathematical modeling of morphological processes in the case of suspended sediment transport. Delft Hydr. Communication, No. 382.

Wieberg, P. L. and Smith, J. D., 1989. Model for calculating bed load transport of sediment. *Journal of Hydraulic Engineering*, Vol. 115, No. 1, pp. 101-123.

Wu, W., Rodi, W. and Wenka, T., 2000. 3D numerical modeling of flow and sediment transport in open channels. *Journal of Hydraulic Engineering*, Vol. 126, pp. 4-15.

Xu B.H. and Yu A.B., 1997. Numerical simulation of the gas-solid flow in a fluidized bed by combining discrete particle method with computational fluid dynamics. *Chemical Engineering Science*, Vol. 52, No. 16, pp. 2785-2809.

Yamauchi, 2014. Study on the stability of tsunami evacuation tower due to drift debris. Undergraduate's Thesis Nagoya Institute of Technology. (in Japanese)

Yeom, G.-S., Nakamura, T. And Mizutani, N., 2009. Collision analysis of container drifted by runup tsunami using drift collision coupled model. *Journal of Disaster Research*, Vol. 4, No.6,

pp. 441-442.

Yu, H. Girimaji, S. S., Luo, L.S., 2005. DNS and LES of decaying isotropic turbulence with and without frame rotation using lattice Boltzmann method. *Journal of Computational Physics*, Vol. 209, pp. 599-616.

Zheng, H.W., Shu, C. and Chew, Y.T., 2006. A lattice Boltzmann model for multiphase flows with large density ratio. *Journal of Computational Physics*, Vol. 218, pp. 353-371.

Zheng, Y. and Struchtrup H., 2004. Burnett equations for the ellipsoidal statistical BGK model, *Continuum Mech. Thermodyn.* Vol. 16, pp. 97-108.

List of Tables

Table 1.1 Examples of experimental conditions from some references.

Table 1.2 Numerical conditions applied by the group of Sakai, Gotoh, Harada, et al. in the years from 1996 to 2011.

Table 2.1 Lubrication ranges for various kinematic viscosities, determined for a sphere of radius a = 8.2Δx, the ranges are determined separately for the normal Δ_{cN}, tangential Δ_{cT} and rotational Δ_{cR} motions.

Table 2.2 Different value of *Se* in Eq. (2.32).

Table 3.1 Simulation conditions in cases with different Shields parameter.

Table 4.1 Characteristics of cases under oscillatory flow (Case 1 – Case 5) and progressive conidal wave (Case 6).

Table 4.2 Composition of mixed grain size sediment.

Table 5.1 The collision number of automobiles for B-type tsunami evacuation tower.

Table 5.2 The collision number of automobiles for C-type tsunami evacuation tower.

Table 5.3 The magnitude of collision speed of automobiles for B-type tsunami evacuation tower (unit: cm/s).

Table 5.4 The magnitude of collision speed of automobiles for C-type tsunami evacuation tower (unit: cm/s).

List of Figures

Figure 1.1 Sediment transport modes on a beach, a simplified 2D view.

Figure 1.2 An aerial view of damage in the Sendai region with black smoke coming from the Nippon Oil Sendai oil refinery.

Figure 1.3 Flow Chart of the present dissertation.

Figure 2.1 Discretized distribution functions fi for the DnQm models.

Figure 2.2 Streaming and collision steps for a fluid lattice.

Figure 2.3 Schematic diagram of D3Q19 LBM model.

Figure 2.4 The surface boundary nodes of curved particles.

Figure 2.5 DFs before and after collision with stationary (a) and moving (b, c) boundary nodes.

Figure 2.6 Schematic graph of three lattice types.

Figure 2.7 Streaming and collision of an interface lattice.

Figure 2.8 Three typical lattice types of interface lattice.

Figure 3.1 Initial set up of uniform size particles in an open channel flow.

Figure 3.2 Snapshot of uniform grain size sediment in open channel flow (τ^*=0.16).

Figure 3.3 Flow velocity fields in longitudinal section (τ*=0.16).

Figure 3.4 2D longitudinal profile of the movements of sediment particles (τ^*=0.025).

Figure 3.5 2D longitudinal profile of the movements of sediment particles (τ^*=0.10).

Figure 3.6 2D longitudinal profile of the movements of sediment particles (τ^*=0.18).

Figure 3.7 Trajectories of individual sediment particles (τ*=0.025).

Figure 3.8 Trajectories of individual sediment particles (τ*=0.10).

Figure 3.9 Trajectories of individual sediment particles (τ*=0.18).

Figure 3.10 The horizontal movement velocity of sediment particles.

Figure 3.11 The vertical existing probability density distribution of sediment particles.

Figure 4.1 Initial snapshots of (a) Case1, Case 2, Case 3, Case 4 and (b) Case 5.

Figure 4.2 Snapshots of side/top view of Case 1 in the developing stage of grading (a, b, c) and developed stage of grading (d, e, f).

Figure 4.3 Snapshots of side/top view of Case 2 in the developing stage of grading (a, b, c) and developed stage of grading (d, e, f).

Figure 4.4 Snapshots of side/top view of Case 3 in the developing stage of grading (a, b, c) and developed stage of grading (d, e, f).

Figure 4.5 Snapshots of side/top view of Case 4 in the developing stage of grading (a, b, c) and developed stage of grading (d, e, f).

Figure 4.6 Snapshots of side/top view of Case 5 in the developing stage of grading (a, b, c) and developed stage of grading (d, e, f).

Figure 4.7 Comparisons of vertical centroids of concentration of particles between Case 1 and other 4 cases. The symbol "z_{gck}*" shows the deviation of the vertical centroid of concentrations of particle-diameter class from its initial value.

Figure 4.8 Comparisons of horizontal centroids of concentration of particles between Case 1 and other 4 cases. The symbol "y_{gck}*" shows the deviation of the horizontal centroid of concentrations of particle-diameter class from its initial value.

Figure 4.9 Mean velocity profiles of sediment particles in Case 1 in the developing stage of grading (a, b, c) and developed stage of grading (d, e, f).

Figure 4.10 Mean velocity profiles of sediment particles in Case 2 in the developing stage of grading (a, b, c) and developed stage of grading (d, e, f).

Figure 4.11 Mean velocity profiles of sediment particles in Case 3 in the developing stage of grading (a, b, c) and developed stage of grading (d, e, f).

Figure 4.12 Mean velocity profiles of sediment particles in Case 4 in the developing stage of grading (a, b, c) and developed stage of grading (d, e, f).

Figure 4.13 Mean velocity profiles of sediment particles in Case 5 in the developing stage of grading (a, b, c) and developed stage of grading (d, e, f).

Figure 4.14 Dimensionless particle number density distribution of Case 1 in the developing stage of grading (a, b, c) and developed stage of grading (d, e, f).

Figure 4.15 Dimensionless particle number density distribution of Case 2 in the developing stage of grading (a, b, c) and developed stage of grading (d, e, f).

Figure 4.16 Dimensionless particle number density distribution of Case 3 in the developing stage of grading (a, b, c) and developed stage of grading (d, e, f).

Figure 4.17 Dimensionless particle number density distribution of Case 4 in the developing stage of grading (a, b, c) and developed stage of grading (d, e, f).

Figure 4.18 Dimensionless particle number density distribution of Case 5 in the developing stage of grading (a, b, c) and developed stage of grading (d, e, f).

Figure 4.19 Water elevation and velocity field of wave generated from initial cnoidal wave.

Figure 4.20 Snapshots of side/top view in the seaward part of Case 6 in the developing stage of grading (a-f) and developed stage of grading (g-i).

Figure 4.21 Snapshots of side/top view in the center part of Case 6 in the developing stage of grading (a-f) and developed stage of grading (g-i).

Figure 4.22 Snapshots of side/top view in the landward part of Case 6 in the developing stage of grading (a-f) and developed stage of grading (g-i).

Figure 4.23 Comparisons of vertical centroids of concentration of particles between landward part and seaward area of Case 6.

Figure 5.1 Layout of experimental set-up. (unit: mm)

Figure 5.2 B-type (left) and C-type (right) tsunami evacuation tower.

Figure 5.3 (a) top view, (b) bottom view and (c) three orthographic views of model automobiles.

Figure 5.4 Snapshots of automobiles through B-type (b) and C-type (d) tsunami evacuation tower at the same time.

Figure 5.5 Trajectories of the center of automobiles through B-type (a) and C-type (b) of tsunami evacuation tower.

Figure 5.6 (a) Initial setup of automobile and dam-break flow; (b) snapshot of movable automobile.

Figure 5.7 Schematic graph of the calculation method for buoyance force when only (a) a corner of the automobiles is submerged and (b)one whole edge of automobile is submerged.

Figure 5.8 Behaviors of drift automobiles in tsunami at (a) initial, and after (b) 0.17s, (c) 0.82s and (d) 1.30s.

Figure 5.9 Simulated trajectories of the center of each automobile.

Acknowledgement

The author would like to express sincere gratitude to her supervisor Prof. Wataru KIOKA, Nagoya Institute of Technology (NIT), without whose helpful guidance, moderate encouragement and effective support, the author couldn't have such a meaningful experience in the academic work in NIT. The author also wants to express deep gratitude to Prof. Akihiro TOMINAGA and Associate Prof. Toshikazu KITANO for their advices and guidance during the doctoral study.

The author would like to express the deep gratitude to Prof. Cuiping KUANG, the author's supervisor at Tongji University, China, who leads the author to the study of coastal engineering and the numerical simulation. The author would also like to thank Prof. Feng ZHANG, who provides the opportunity for the doctoral study in NIT, and his family, for their enthusiasm and hospitality.

The author would like to express thankfulness to Dr. Ni Nyoman PUJIANIKI, for her help in daily life and advices on the study; to Rikuya TAKAHASHI and Masashi OKAJIMA, for their help as Japanese tutors; to Shintaro YAMAUCHI for his help in the hydrodynamic experiment of tsunami drifting automobiles; and to all the other members of Kaikan's Laboratory who show welcome and kindness to the author.

The dissertation has been financially supported by the Japanese Government Scholarship Program, Ministry of Education, Culture, Sports, Science and Technology (MEXT). The dissertation has also been technically supported by Prof. Anthony J. C. LADD for his previous studies on particle-fluid suspension.

Last but not least, the author would like to express her deep gratitude to her family and her friends. Their accompanies and encouragements paint the life of the author in Nagoya with more colors and make it full of cheerfulness. Especially thankfulness goes to the author's parents, from whom the author always gets courage and strength.